SACLANTCEN MEMORANDUM
serial no.: SM-269

SACLANT UNDERSEA
RESEARCH CENTRE

MEMORANDUM

Interpretation and representation of the synoptic features in the Iceland–Faeroe–Shetland region

G. Peggion

July 1993

Page count for SM-269 (excluding Covers and Data Sheet)

Pages	Total
i–vi	6
1–70	70
	76

SACLANT Undersea Research Centre
Viale San Bartolomeo 400
19138 San Bartolomeo (SP), Italy

tel: 0187 540 111
fax: 0187 524 600
telex: 271148 SACENT I

NORTH ATLANTIC TREATY ORGANIZATION

SACLANTCEN SM-269

Interpretation and representation of the synoptic features in the Iceland–Faeroe–Shetland region

G. Peggion

The content of this document pertains to work performed under Project 04 of the SACLANTCEN Programme of Work. The document has been approved for release by The Director, SACLANTCEN.

Issued by:
Underwater Research Division

H. Urban
Division Chief

intentionally blank page

SACLANTCEN SM-269

Interpretation and representation of the synoptic features in the Iceland–Faeroe–Shetland region

G. Peggion

Executive Summary: Reliable assessment and prediction of sonar capabilities requires a knowledge of the dominant features of the ocean dynamics and the associated spatial and temporal variability. Ocean dynamics, through the resultant current structures, determine the temperature, salinity, and sound-speed distributions. As a result in regions of high mesoscale variability frequent (real-time) data collection is required in order to update the sound-velocity information.

Ocean models complement data collection by predicting the currents that change the thermal structure between times of data collection. In this way numerical ocean models supply acoustic velocity information between times of observation and in regions not accessible to data-gathering. Under adverse conditions (e.g. bad weather, times of crisis) one must rely primarily on such models to accurately estimate acoustic propagation conditions for ASW operations.

This paper studies the ability of an inverse model (model that calculates ocean currents from hydrography data) to reproduce the ocean currents measured in the Iceland–Faeroe Front (IFF) region. The data from 6 currentmeter moorings deployed during the June 1989 Icelandic Current Experiment (ICE) cruise are analyzed and interpreted. A high degree of mesoscale and internal tide activity is found.

It is found that this particular inverse model reproduces the mean trends of the ocean currents that are evident in mooring and satellite data. The representation and resolution of the currents can be improved by increasing the horizontal temperature and salinity gradient resolution during the hydrographic survey.

The calculated ocean currents can be used as initial conditions in a regional eddy-resolving dynamic model and as a guide for MCM operations. The use of the inversely calculated currents as initial conditions in dynamic ocean models will lead to better propagation forecasting and improved interpretation of transmission loss in terms of oceanic features.

intentionally blank page

SACLANTCEN SM-269

Interpretation and representation of the synoptic features in the Iceland–Faeroe–Shetland region

G. Peggion

Abstract: The kinematic structure of the sub-inertial fluctuations of measured current and temperature fields from 6 moorings deployed during the June 1989 Icelandic Current Experiment (ICE) cruise is analyzed and interpreted. The field of operations encompassed the Iceland–Faeroe Front (IFF) where high temperature and salinity gradients exist together with mesoscale activity. The currentmeter records were found to be highly contaminated by tidal signals and contain evidence of 2–5 day oscillations (the mesoscale events) embedded in a long period signal of about 10–15 days (synoptic events). The currentmeter data is analyzed for vertical and horizontal coherence. The variability of the IFF is highly energetic and mainly due to baroclinic instability of the frontal flow. Satellite images of the region show that in the vicinity of the front mesoscale features are present with horizontal scales of 15 to 50 km. Ocean currents were calculated from hydrography data with a diagnostic model. The model assumes geostrophic and hydrostatic balances and uses CTD measurements taken in the region during the interval of currentmeter measurements. It is found that the model reproduces the large scale current structures of the region but underestimates the velocity magnitude of the upper ocean. This is attributed to the simplified physics that is incorporated into the formalism.

Keywords: Bryan–Cox model ○ currents ○ salinity ○ sound velocity ○ temperature

Contents

1
Introduction

This memorandum addresses the problem of representing the synoptic features and predicting the mesoscale variability of the Iceland–Faeroe Front (IFF). In this study, the term synoptic refers to oceanic features with spatial scales ranging from tens to low hundreds of kilometers and lifetimes of the order of weeks or months. Synoptic motions in the ocean can be classified according to their generation mechanisms into frontal motion or meanders in jet current systems, free motion of eddies generated by baroclinic and barotropic instabilities, topographic effects, and atmospheric factors. Excursions and oscillations of these features on a spatial scale of hundreds of meters or several kilometers, and timescales of a few days, are highly energetic and henceforth are referred to as mesocale variability (Monin, 1986).

The IFF, separating the warmer and saltier water of Atlantic origin (NAW) from the colder and less saline water of Arctic origin (AW), presents an extensive formation of meanders and eddies that may affect the whole water column. Satellite images show that the front is disturbed by mesoscale meanders and eddies with 10–50 km wavelength.

Fluctuations of these features are mainly concentrated on a period of 2–10 days, with velocity oscillations up to 30 cm/s (Koshlyakov, 1986). The front is located on the sea surface at about 100 km north of the Iceland–Faeroe Ridge (IFR), but the frontal interface is inclined and touches the ocean bottom along the crest of the ridge. North of the Faeroe Bank, part of the IFF moves northwards, closing the cyclonic gyre that characterizes the circulation in the Greenland–Iceland–Norwegian (GIN) Sea, part recirculates feeding the Norwegian Atlantic Current (NwAtC) that enters the basin from the Faeroe–Shetland Channel.

Due to the high strategic relevance of the IFF, operational interests require an accurate and extensive description of the environmental conditions of the IFR. Only recently, has increased computer power and measurement capability provided the tools necessary for a new generation of numerical models able to describe synoptic oceanographic features and predict their effects on acoustic environmental conditions.

This study is an investigation to test and verify the procedure developed at SACLANTCEN (Peggion, 1991, hereafter referred to as Part 1) for the initialization of time-dependent numerical models of ocean circulation. The model is applied and evaluated using the oceanographic measurements of the GIN 89A cruise. This field experiment was conducted by SACLANTCEN in the Iceland–Faeroe–Shetland re-

gion from May 24 to July 1, 1989. From CTD measurements of temperature and salinity, numerical experiments are carried out to simulate the 3D circulation in the Iceland–Faeroe–Shetland region. The model formulation relies heavily on the quality of the observational program; i.e., it is implicitly assumed that the data set furnishes an adequate representation of the large-scale (spatial and time scales greater than, or equal to, those of the synoptic motion) features. The objective analysis procedure used for the interpolation of the data is chosen to preserve the dominant spatial scales contained in the observed field. The circulation pattern is derived by diagnostic computation, in that density field is not computed but known from observations; the predicted quantities are pressure and velocity fields. A detailed description of the model formulation is given in Sect. 4.

The validity of the circulation pattern as described in Part 1 is tested by comparison with currentmeter data and remote sensing images taken in the IFR region during the GIN 89A hydrographic survey. The data and methods used to analyze the currentmeter record are illustrated in Sect. 2. The circulation pattern as derived from the currentmeter time series is described in Sect. 3, and compared with the numerical results in Sect. 4. Evaluation of the model results with respect to the data reported in this study is a difficult task. The problems arise from two different sources being concerned with the limitations of both the observational program and the mathematical formulation of the numerical model. These problems are discussed in Sect. 4. Finally Sect. 5 summarizes this study.

2
Data and Observations

Currentmeter data are taken from 6 of the 9 moorings deployed during the GIN 89A cruise. Information associated with the deployment and recovery of the instruments is summarized in Table 1. Instruments are referred to in the text and figures by numerical codes. The first three digits indicate the mooring site, the last the instrument depth (with the number sequence increasing towards the ocean bottom). The moorings are divided into 2 arrays: Array 1 consisted of moorings 2 and 3 and was located north of the Faeroe Continental Shelf, in the region where the IFF and the NwAtC come into contact. Array 2 consisted of the remaining moorings and was centered at roughly 64°N and 9°W, where the IFF axis is expected to be (Fig. 1). The two arrays were separated by about 180 km, and the moorings at a spatial resolution ranging from 20–60 km, to allow the study of a wide range of spatial scales in the front region.

The data and methods applied in the analysis of the currentmeter records are described in Appendix A. For the purposes of this research, the original time series (henceforth referred to as OTS) were low-pass filtered with a 48 h cutoff frequency to remove tidal and inertial energy. The new series are referred as to as LPF2. The LPF2 time series were low-passed again with a 10 day cutoff frequency (LPF10) to remove mesoscale signals and define the dominant events in the synoptic range.

Sea-surface temperature data from the NOAA polar orbiting satellites could also be used in interpreting the *in situ* measurements. Unfortunately, the IFR region is characterized by a high concentration of clouds that markedly reduce the applicability of remote sensing observations. For the time of the GIN 89 cruise, only one image taken on an uncommonly clear day (June 19, 1989, or Julian day 170) is available for the region of interest (Fig. 2).

Table 1 *Mooring locations, bottom depth, data return, and instrument depth (position and water depth correspond to the location of the anchor-drop)*

Instr.	Lat. (N)	Long. (W)	Bottom depth (m)	Day (1989)[1]		Instr. depth (m)
				Start	Stop	
S02_L00	62°56.06′	6°13.90′	1003	26 May (146)	2 Oct. (275)	91
S02_L01						260
S02_L02						524
S03_L00	63°15.20′	5°47.85′	2009	27 May (147)	2 Oct. (275)	187
S03_L01						355
S03_L02						619
S03_L03						1623
S05_L01	64°04.62′	8°43.93′	1002	29 May (149)	30 Sep. (273)	255
S05_L02						524
S06_L00	64°20.75′	8°14.01′	1997	30 May (150)	29 Sep. (272)	45
S06_L01						205
S06_L02						472
S06_L03						1485
S07_L00	64°18.40′	9°32.97′	714	31 May (151)	29 Sep. (272)	113
S07_L01						280
S07_L02[2]						547
S09_L00	64°10.44′	9°12.41′	999	31 May (151)	28 Sep. (271)	84
S09_L01						246
S09_L02						583

[1] The numbers in brackets are the corresponding Julian day.
[2] Quality of data set was not good.

2.1. THE OBSERVED CURRENTS

The basic statistical functions for the OTS, LPF2 and LPF10 time series are listed in Table A1, and shown graphically in Fig. A1 of Appendix A. It can be observed that the filters imposed on the OTS do not noticeably alter the mean values, but greatly reduce the oscillations in the records, suggesting that the region is affected by a high variability in the inertial-to-mesoscale range. However, for all three data sets, the confidence limits (usually about 80% of the standard deviation) often include zero, so that the flow direction is not resolved by these records.

A quick comparison between the OTS and LPF2 time series clearly indicates that the circulation is strongly contaminated by tidal energy. A hint of the tidal amplitude at the mooring sites may be obtained by computing the difference between the maximum and minimum excursions of the OTS and LPF2 records. As a function of the vertical structure of the tidal components, the OTS indicate two distinct behaviors. The mooring sites that are located far from the IFR (i.e. in regions of slowly-varying bathymetry) show tidal currents which are mainly barotropic with no more than 40% reduction in amplitude between the shallowest and the deepest instrument. On the other hand, close to the IFR (i.e. in a region characterized by

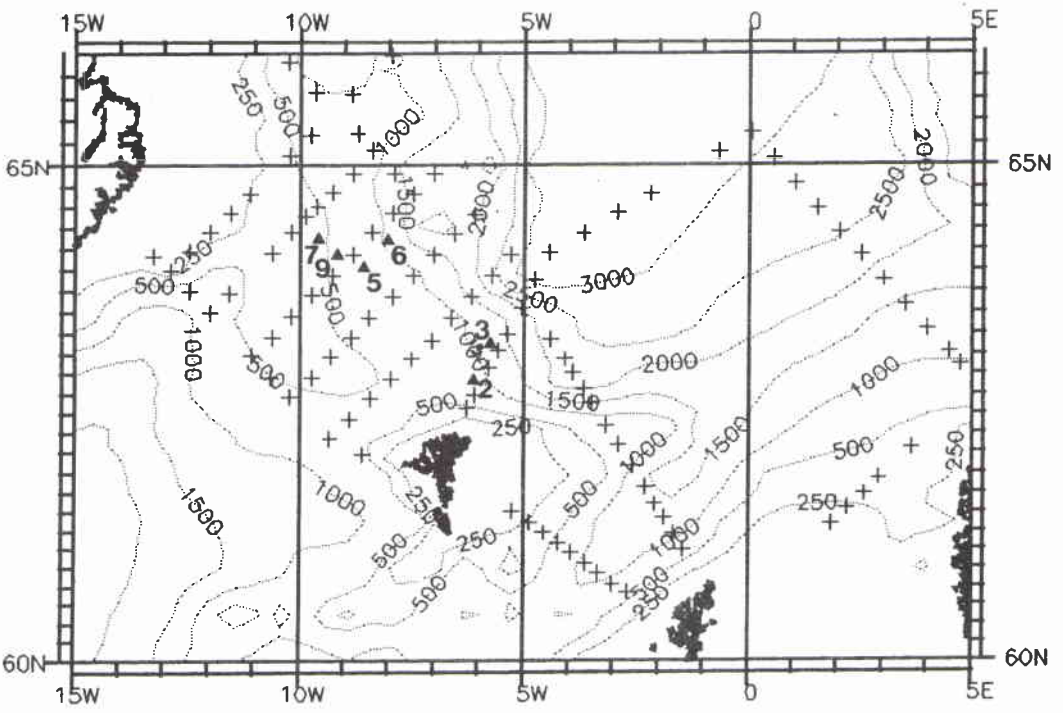

Figure 1 *GIN_89A cruise data distribution. Crosses indicate CTD cast stations, and triangles the currentmeter mooring locations.*

strong variations in the topographic features) tidal amplitude markedly increases with depth, so that the interaction of tides with the bathimetry is feeding energy at the inertial frequency.

3.1. THE LOW-PASS FILTERED TIME SERIES

The filtered velocity components contain clear evidence of 2–5 day fluctuations embedded in a long-period signal with a period of about 15–20 days. The autospectra for all the instrument records are similar as a function of frequency and for both velocity components. The lowest frequency band (20-day period) is highly energetic, and contains at least one order of magnitude of energy more than the other frequency bands. The autospectra of the poleward velocity components often present a peak at about 5-day period, which could correspond to atmospheric forcing fluctuations.

The coherence functions among the mooring records were also calculated. Table 2 indicates the stations with a coherence function above the 90% significant level (usually at about 0.40) at least in one of the velocity components, and for some

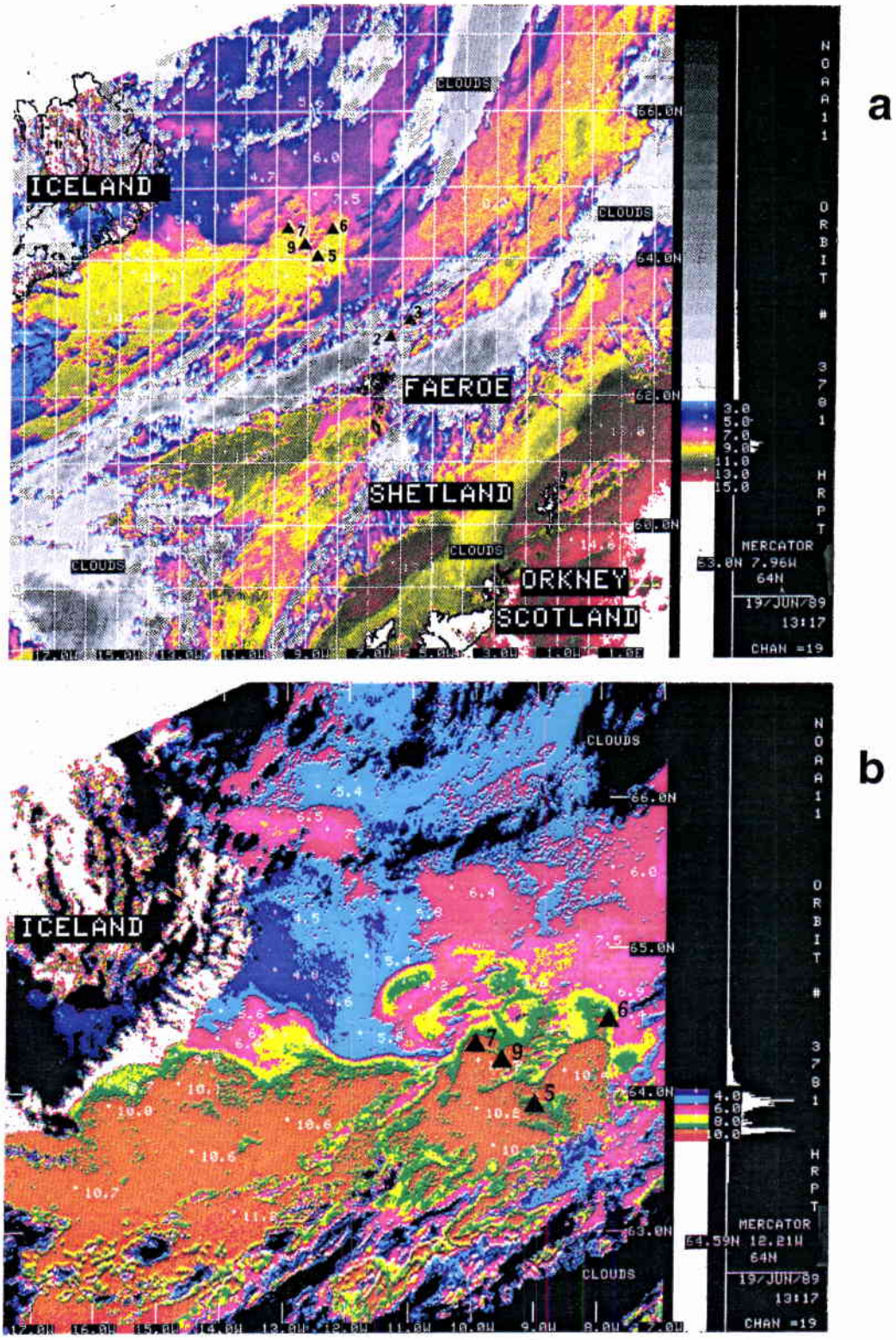

Figure 2 *Sea surface temperature data from the NOAA polar orbiting satellite. (a) The Iceland–Faeroe–Shetland region for 19 June 1989; (b) an enlarged portion of the Iceland–Faeroe ridge. Images processed at SACLANTCEN by E. Nacini.*

Table 2 *Correlation diagram between velocity components of each currentmeter mooring. Correlation functions above the confidence limit are indicated as follows: Circles for both u and v components, rhombi for u-velocity only, triangles for v-velocity only*

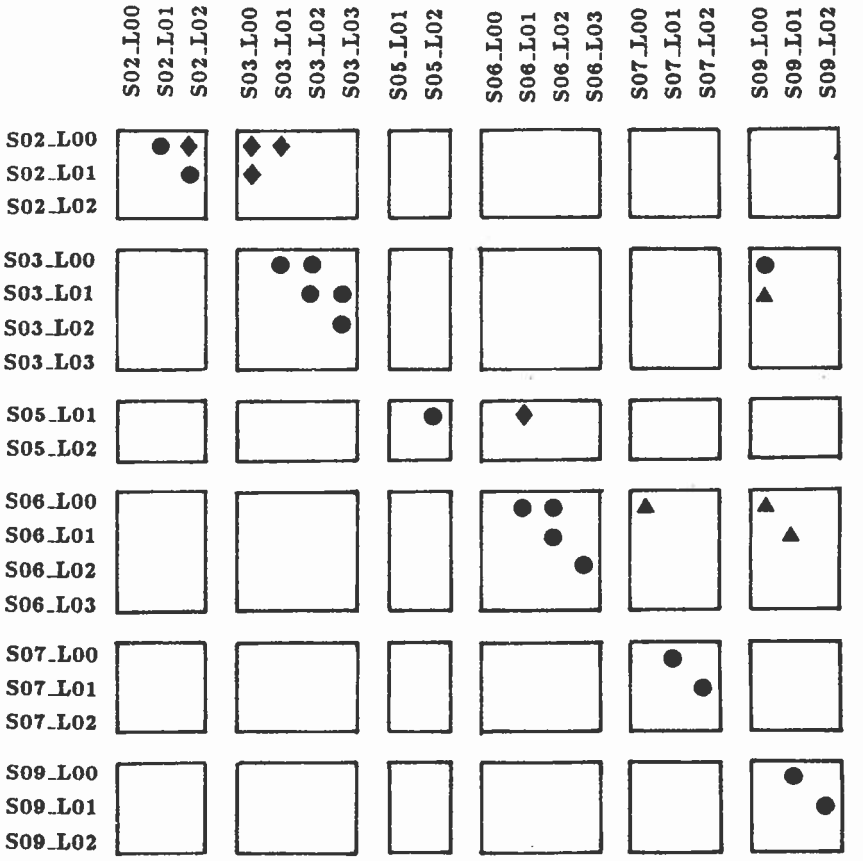

frequency band. All the moorings show a strong vertical coherence between the first two upper instruments (say, in the first 200 m depth), but the u- and v-components have dissimilar behaviors, and the correlation between records at the same site appears to be dependent upon the array location.

The coherence functions at site S02 are shown in Fig. 3 as representative examples of the vertical energy distribution at Array 1. The records of the upper instruments are well correlated over all the frequency band, and for both velocity fields, so that the kinetic energy is uniformly distributed in the upper ocean layer (Fig. 3a). The agreement is lost between the upper and lower levels: the long period motion maintains a barotropic component only in the eastward velocity component (Fig. 3b). The vertical spectral distribution along the IFR is illustrated in Fig. 4. It can be observed that the eastward velocities of the S09_L00 and S09_L01 instruments are coherent in the lowest frequency band, and the poleward velocity at about the 5 day period. The differences in the frequency range imply that a significant confidence

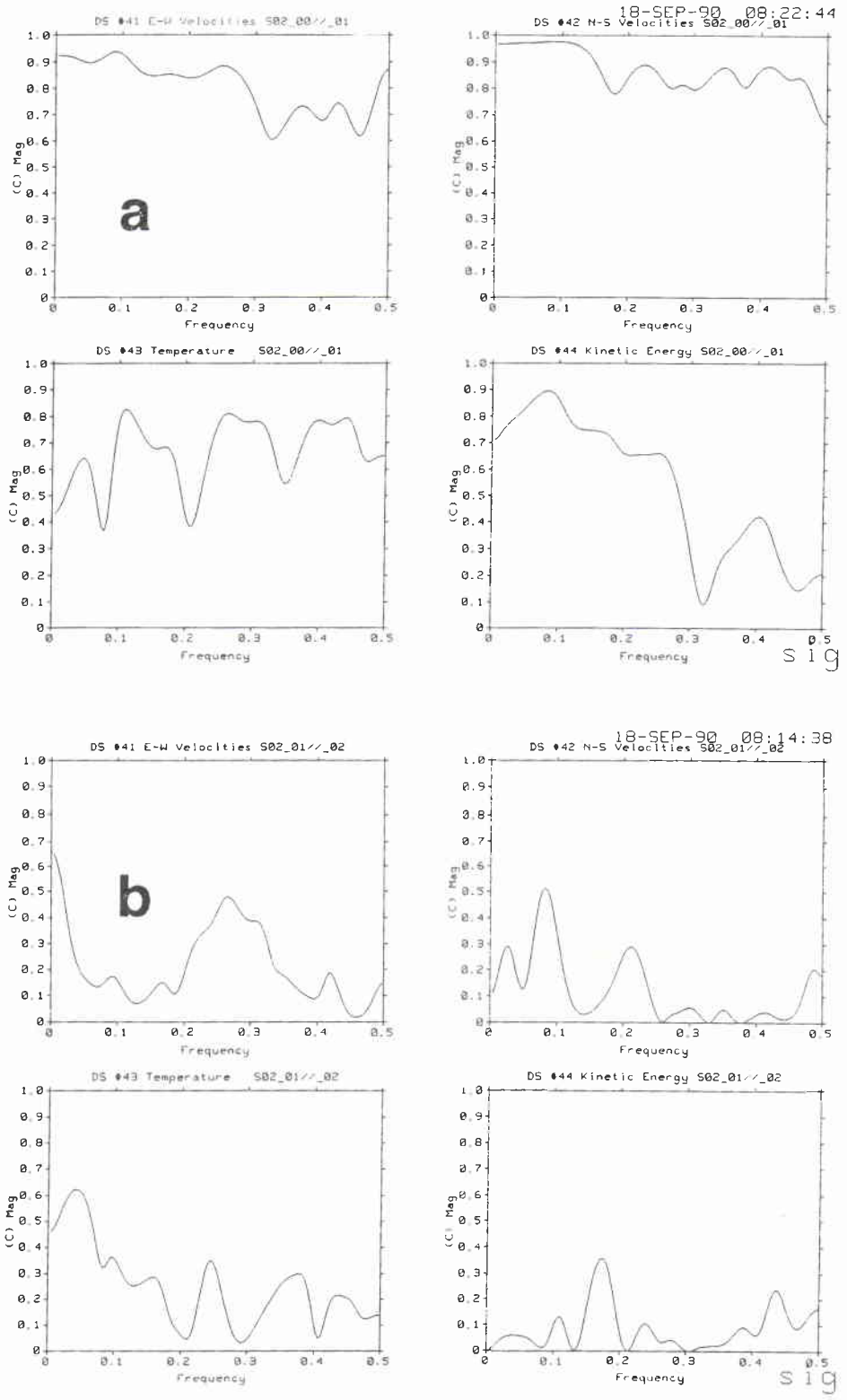

Figure 3 *The coherence functions between eastward velocity, poleward velocity, temperature and kinetic energy of currentmeter moorings a) S02_L00 and S02_L01; b)S02_L01 and S02_L02.*

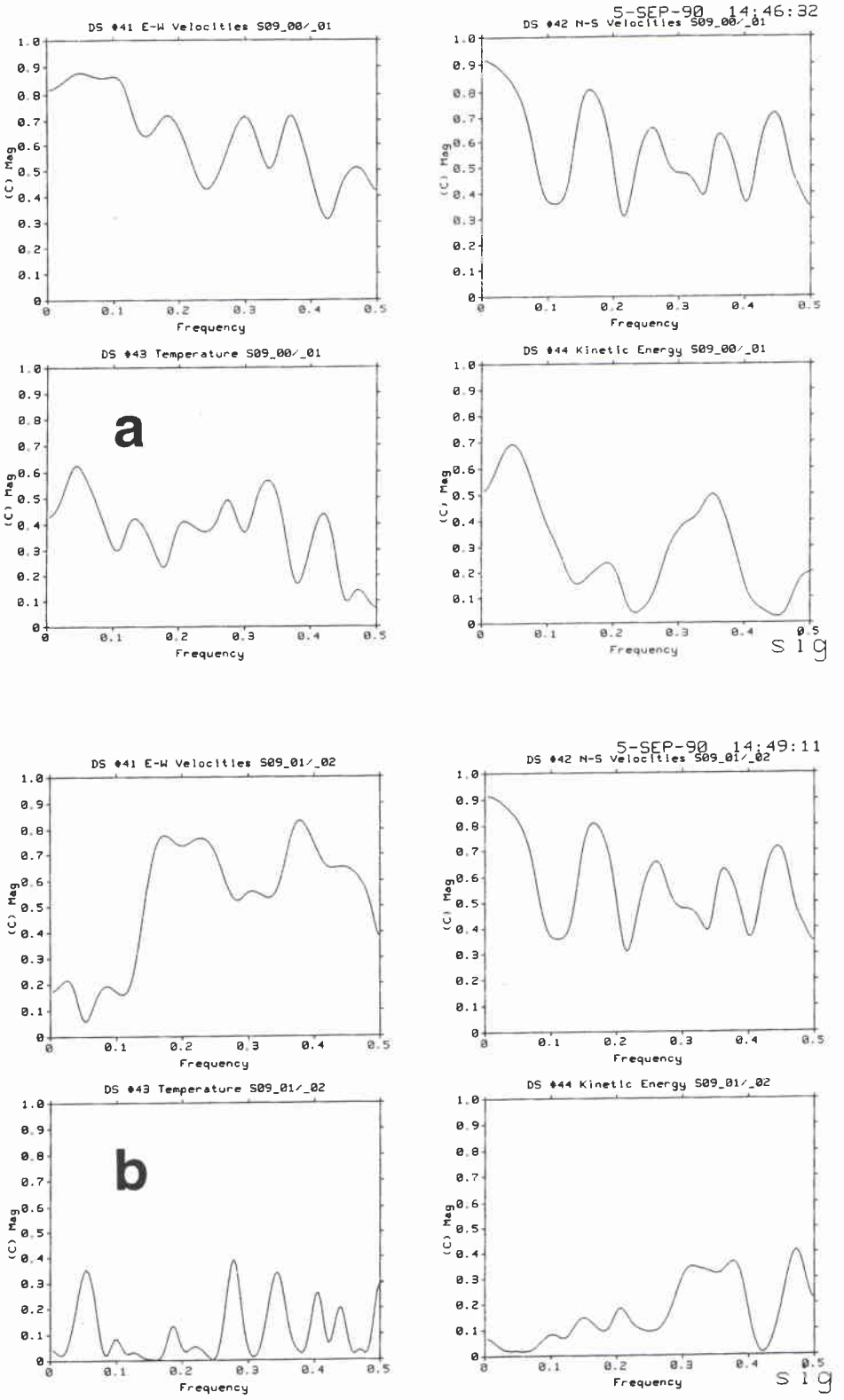

Figure 4 *The coherence functions between eastward velocity, poleward velocity, temperature and kinetic energy of currentmeter moorings a) S09_L00 and S09_L01 ; and b) S09_L01 and S09_L02.*

Table 3 *EOF vertical analysis at sites S02 and S09*

Modes	Eigen-values	Variance (%)	Eigenvectors[1]		
			L00	L01	L02
Site S02					
1	687.26	94.09	0.77	0.61	0.12
			97	*93*	*89*
2	186.76	4.76	0.14	0.02	0.99
			−84	*−57*	*90*
3	44.54	1.13	0.61	0.78	0.07
			−94	*83*	*−91*
Site S09					
1	887.01	92.07	0.93	0.36	0.03
			127	*123*	*67*
2	56.53	5.86	0.26	0.46	0.86
			−93	*77*	*67*
3	19.86	2.06	0.30	0.80	0.50
			−103	*76*	*−115*

[1] Normalized amplitudes are given in roman, and directions in italics.

level is lost in the kinetic energy cross spectra (Fig. 4a). While the fluctuations of the poleward velocity component are almost uniform at all water depths, the eastward velocities of the upper and lower levels are uncorrelated in the low frequency band (over the 3 day period). Temperature distribution at 200 and 500 m depth are also uncorrelated, suggesting that two different water masses are flowing through the mooring site. These findings are also confirmed by the empirical ortogonal function (EOF) analysis carried to investigate the vertical structure of the motion. Table 3 shows the percentage of the total variance and the modal decomposition at the S02 and S09 mooring sites accounted for the first 3 vertical modes. At both array locations, mode 1 provides more than 90% of the total variance, and the succesive modes are not significant. In view of the overwhelming contribution of mode 1, further consideration will be restricted to this mode. Along the IFR, mode 1 feeds 93% of the energy recorded in the nearsurface instrument, but only 36% of the energy at the intermediate level. This implies that the whole water column is affected by a strong baroclinic component of motion that is particularly significant between instruments S09_L01 and S09_L02. Moving to Array 1, the first mode is depth independent in the upper ocean layer, but the time series also indicate considerable fluctuations in the velocity field around this mode.

3

The circulation pattern

The spatial horizontal coherence between records is less obvious than the vertical. As Table 2 indicates, the horizontal spatial structure of the flow appears almost random and casual, with very little energy in the cross spectra. However, arrays 1 and 2 manifest different tendencies: Array 2 indicates a weak correlation in the poleward velocity usually in the low frequency band (greater than 10-day period); on the other hand, it is the eastward velocity of array 1 that shows some correlation in the same frequency band.

These results confirm that the LPF2 time-series are still contaminated by a high mesoscale variability, so that the synoptic motion is not resolved. The complexity of the IFF dynamics may be seen by analysis of the S07 and S09 mooring records. Although the sites are only about 20 km apart, the records are strongly uncorellated, confirming the difficulty of reliable synoptic surveys in the IFR region. As Figs. A14 and A19 illustrate, until the beginning of August the records are well correlated with a shift period of about 10 days (in the S07 to S09 direction) which is equivalent to a mean velocity of about 2.5 cms^{-1}. However, the relationship between the two locations is completely lost after day 220. While site S07 is characterized by the northward excursions of the IFF, and consequent warming of the water column, the instruments at site S09 recorded a marked drop in temperature. The phenomena is clearly seen at the S09_L01 location (Fig. A18) where temperature dropped off by about 0.5C° per day between July 28 and August 5. This sharp temperature change is not seen in the time-series of the upper instrument, in which the cooling is much less evident. Temperature steadily decreased by about 1.5C° between July 28 and August 30, and subsequently increased again because of the transit of a warm eddy-like feature. Thus, temperature variations at site S09 indicate a southward intrusion of Artic water at intermediate-deep depths while the upper front location is not noticeably affected, confirming that subsurface temperature changes are not always related to SST variations.

4

Numerical simulations

The model described in Part 1 is a procedure developed for fitting data into model initialization. Observational data have been processed to provide an ocean structure on a 3D regular grid, that preserves the dominant spatial features contained in the records. It is implicitly assumed that the measured fields contain all the information on their past history, so that the constituent distributions can be considered instantaneously time-independent. From the processed temperature and salinity data, absolute velocities have been computed.

The model mathematical formulation assumes the ocean to be non-diffusive and inviscid except close to the sea surface where there exists an adiabatic Ekman-type boundary layer sustained by wind and atmospheric forcing. The flow of the inner ocean is assumed to be geostrophic and hydrostatic. The assumption of geostrophic and hydrostatic balances is traditional and often confirmed by direct measurements in the inner open ocean. As is well known, those assumptions define the vertical shear of the velocity, which upon integration leave the velocity components undetermined by an integration constant. The indeterminacy of the problem is removed in a mathematical framework assuming that the barotropic component of the velocity field has a length scale large with respect to the observational grid, and the small-scale noise in the hydrographic data is uncorrelated between stations (Peggion, 1987). The velocity, solution of the inversion is finally chosen to be the most consistent with the data distributions (i.e. absolute velocities are required to minimize the misfit in the constituent conservation equations over the whole domain of interest). The omissions of vorticity conservation, non-linearity, and time-dependence are the major limitations in the theoretical and mathematical formulation of the problem. However, these conditions might be not restrictive when the method is applied to large domains using climatological/statistical data sets. Under such circumstances, the effects of the neglected physical processes can be thought of as a sub-scale noise of the dynamics under investigation.

4.1. PRELIMINARY REMARKS

Real measurements and observations seldom satisfy the assumptions of the numerical model, so that their use complicates the interpretation and validity of the simulations. In the following discussion, the solution of Part 1 is examined and taken as a representative sample of this question. The problems arise primarily from two different sources, being concerned with the limitations of both field program and the mathematical formulation of the model. They may be summarized as follows:

1. The data set, input for the numerical experiments of Part 1, is from 120 CTD stations taken during the GIN 89A hydrographic survey. The observational program considered a spatial resolution between stations of about 25 and 60 km across and along the front directions, respectively. The sampling covered a period of about 3 weeks, with the maximum concentration of stations in less than a 10 day period. Thus, the field program is adequate to describe the synoptic feature of the region, but stations are too coarse for a reliable representation of the mesoscale variability. Moreover, the original data are contaminated by sub-scale signals that contain a substantial amount of energy. The numerical regular grid used in the model has a spatial resolution of about 20×40 km on the longitude and latitude axis, respectively, so that, similarly to the field program, synoptic, but not mesoscale, features are correctly parametrized.
2. The appearence of synoptic disturbances in the IFR region is primarily caused by the baroclinic instability of a frontal current (Willebrand and Meincke, 1980). This implies that the dynamics described in the model formulation of Part 1 are not adequate to represent all the physical mechanisms acting on the IFF. Basically, the dynamics are characterized by the conversion of available potential energy (due to the temperature and salinity differences between the NAW and Artic Water water masses) to the kinetic energy carried by the zonal flow. The length scale of the associated disturbances is of the order of the Rossby radius of deformation $L_R = NHf^{-1}$ (where N is the Brunt–Väisälä frequency, H the depth of the ocean, and f the Coriolis parameter) which is about 15 km in the IFR region (Hansen and Meincke, 1979). Conservation of potential vorticity, advection, time dependence, all physical mechanisms neglected in the model formulation of Part 1, are necessary terms in the development of a suitable theory on the instability genesis.

Evaluation of the model results presented in Part 1 with respect to the data reported in this paper is a difficult task; however some low-level comparisons are discussed. Since the structure of the mean flow is not determined by the currentmeter records due to the nonlinear, non-zero time averaging oscillations, analysis is henceforth restricted to the currentmeter data recorded between June 5–28, 1989, the period during which the hydrographic survey described in Part 1 took place. From a standard statistical approach, the numerical experiments have been successfull because the computed values are within the confidence limits of the currentmeter time series. Unfortunately, in most of cases the LPF10 time series presented confidence limits which were too great, and standard deviations including zero (see Table A1), so that the comparison is inconclusive from the physical point of view, even though mathematically correct. The mean velocity vectors computed from the LPF10 time series are depicted in Fig. 5. It may be easily observed that at the Array 1 location the circulation pattern presents strong horizontal shear and does not properly define the long-term structure of the IFF. At the Array 2 location, the flow appears strongly convergent. The effect is apparent, because the moorings are not at the same depth, but at a level difference of about 100 m.

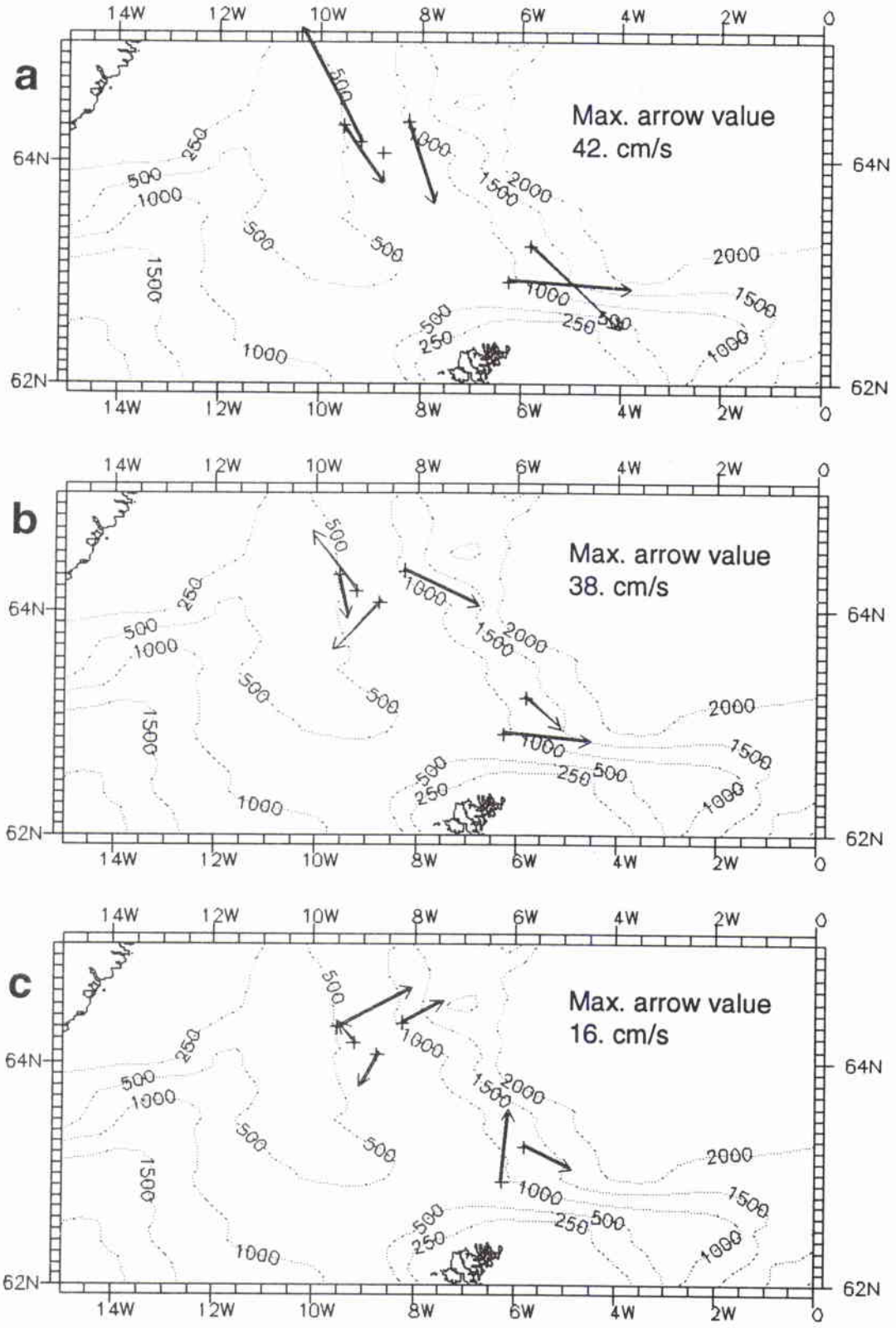

Figure 5 *The LPF10 mean velocity vectors for the period 5–28 June 1989 computed for the currentmeter moorings at level a) L00; b) L01; and c) L02.*

Since the mean values of the currentmeter records over the period of the hydrographic survey are not representative of features with a lifetime of the order of three weeks (i.e. the synoptic time scale), a new possibility is to consider the LPF10 time series limited to a small interval of time centered at the moment at which the closest CTD measurments were taken. A time interval of 3 days is henceforth considered. This period is long enough for assuming the mean values under a geostrophic balance, but short enough for producing acceptable standard deviation values. The resulting mean velocity vectors are illustrated in Fig. 6. It should be noted that the vector configurations are not simultaneous: the vectors of Array 1 are centered on June 25 (or Julian day 176), and those of Array 2 on June 16 (Julian day 167).

The comparison criterium implicitly assumes that the CTD temperature profiles are representative of the mean temperature values from the nearest currentmeter instruments. However, the high spatial variability of the region does not guarantee the accuracy of such a condition. Mooring site S07 is a good example of the problem. The mooring location is surrounded by 4 CTD stations at distances ranging from 20–35 km (Fig. 1), however none of the CTD temperature profiles is consistent with the 3-day mean value of the time series: some CTD values being too warm, other too cold. Unexpectedly, the interpolated temperature profile at the closest numerical grid point, shows a good agreement with the averaged currentmeter data. (i.e. data are strongly contaminated by the mesoscale (sub-grid) features which are removed by the interpolation procedure acting as a small-noise filter). Because the interpolated field is always accurate within the range of the spatial resolution of the numerical grid, the comparison between the currentmeter time series and the numerical experiment computations is made by choosing among the 4 nearest numerical grid points, the one with the temperature profile most consistent with the currentmeter records. The results are summarized in Table 4, and illustrated in Fig. 7.

4.2. MODEL-DATA INTERCOMPARISON

The numerical experiments reproduce most of the features contained in the currentmeter measurements. In general, the model of Part 1 is successful in computing the flow direction, but underestimates the magnitude of the current system. Indeed, the numerical solutions are accurate in determining the shear of the velocity in the upper and lower layer, separately, but poor in the thermocline region. Thus, the hydrographic survey and the model of Part 1 reproduce correctly the deep baroclinic component of the motion. The discrepencies in the thermocline region will be discussed at the end of this section. The missed flow component is not barotropic (i.e. it does not affect the total water column equally), but is confined mainly to the upper layer, where the differences between the observed and computed values are usually independent of depth. Below the thermocline, the numerical solutions are in fairly good agreement with the measured currentmeter values. These conditions apply particularly in proximity to the Array 1 mooring locations. At the Array 2 mooring sites, the dynamics appears to be contaminated by a strong vari-

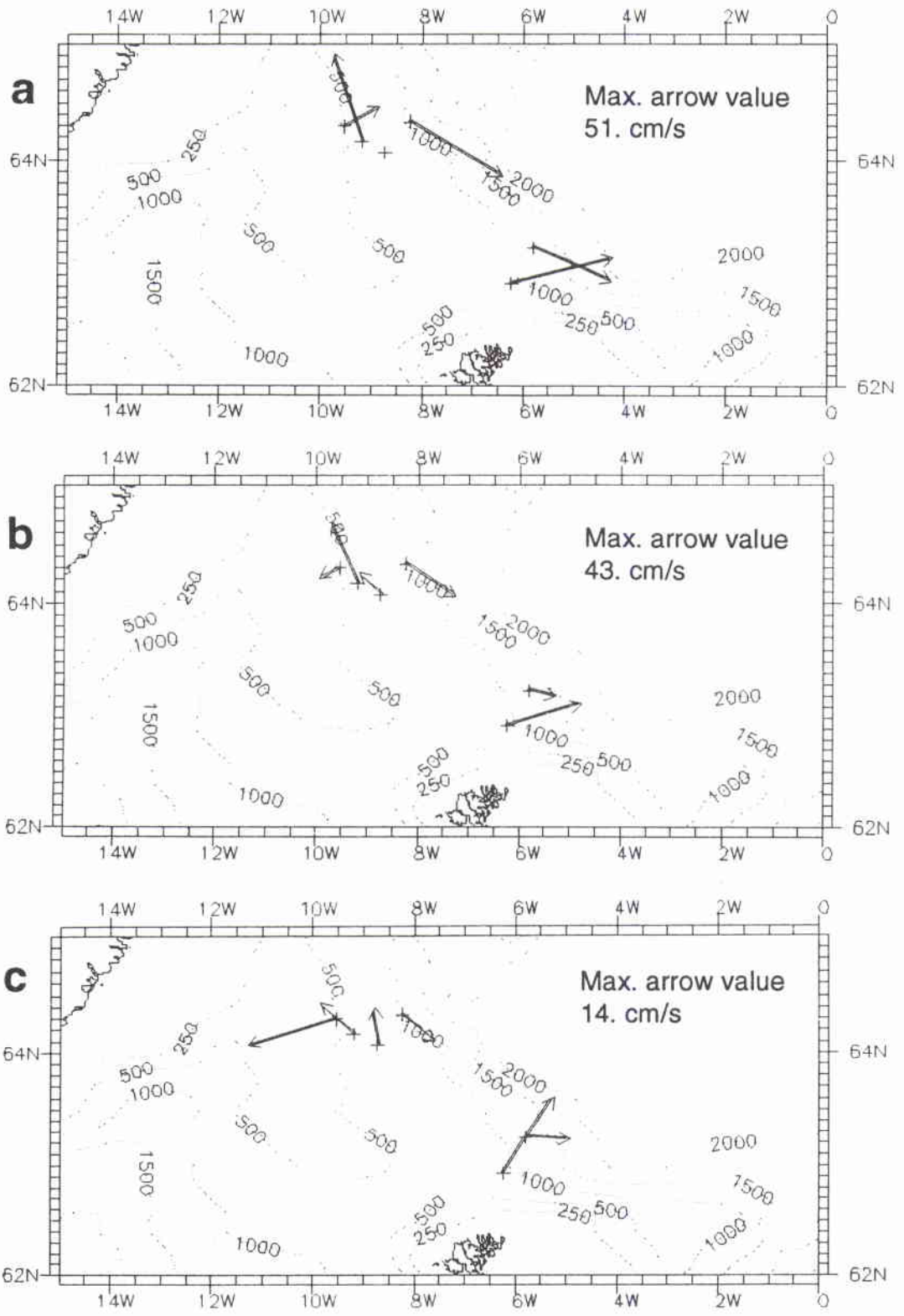

Figure 6 *The LPF10 mean velocity vectors for a three-day time-interval. See text for explanation of definitions. Same as Fig. 5.*

Table 4 *Comparison between the numerical experiments and the currentmeter three-day mean values relative to the days of the CTD stations (see text for an explanation of terms used)*

	CTD Days			Numeric. Comput.		
	u	v	T	u	v	T
S02_L00	46.99	11.80	7.78	15.13	4.87	7.88
S02_L01	41.30	13.23	7.47	9.78	2.54	7.24
S02_L02	6.45	10.17	1.49	2.05	2.78	1.56
S03_L00	36.02	−16.04	6.37	10.19	−4.43	6.45
S03_L01	7.47	−1.48	2.01	3.93	−2.72	3.39
S03_L02	4.46	−0.05	0.02	−0.80	−2.38	0.65
S03_L03	−1.58	−3.62	−0.80	−1.74	−1.96	−0.87
S05_L01	−6.17	5.94	4.63	−0.95	3.73	3.75
S05_L02	−0.40	3.55	−0.19	−0.02	1.45	−0.12
S06_L00	43.60	−25.90	5.58	6.13	−14.06	5.96
S06_L01	15.65	−10.26	1.48	2.87	−7.68	1.41
S06_L02	3.24	−2.76	0.03	0.10	−0.41	−0.21
S06_L03	0.41	−1.17	−0.87	−0.01	0.09	−0.80
S07_L00	14.87	8.22	4.09	1.29	−3.78	3.65
S07_L01	−5.11	−3.03	0.62	2.15	−5.84	0.54
S07_L02	−13.76	−4.41	-	−0.03	0.09	−0.43
S09_L00	−12.87	38.17	6.60	−4.39	3.11	5.38
S09_L01	−9.85	22.47	3.41	−0.95	3.73	3.85
S09_L02	−3.40	2.97	−0.47	−0.02	1.45	−0.12

ability, which complicates the comparison between currentmeter measurements and numerical solutions.

As Fig. 6 illustrates Array 1 is characterized by a strong horizontal shear of the velocity field between sites S07 and S09. This feature is represented also by the numerical experiments (Fig. 7), even though the computed velocities at site S07 are not completely accurate. At mooring location S07_L02, the currentmeters indicate a strong deep undercurrent which is underestimated by the numerical simulations. As was discussed in Part 1, the inaccuracy is mainly due to the vertical grid resolution of the numerical model which is too coarse for a correct parametrization of the deep flow. Both observed and computed values indicate that the flow at sites S06 and S09 is parallel to the 1000, and 500 m. isobath, respectively.

The high mesoscale activity that occurred at this time along the IFR is shown in the satellite AVHRR image from June 19, 1989 (Fig. 2). The coldest water in the image is the dark blue on the Iceland Shelf, warming to light blue, violet, yellow, green, and orange. Cloud formations are indicated by the black color. Near the Iceland Continental Shelf, the IFF is clearly indicated by the color change between the light blue and the yellow color. Moving eastwards, towards the Array 2 site,

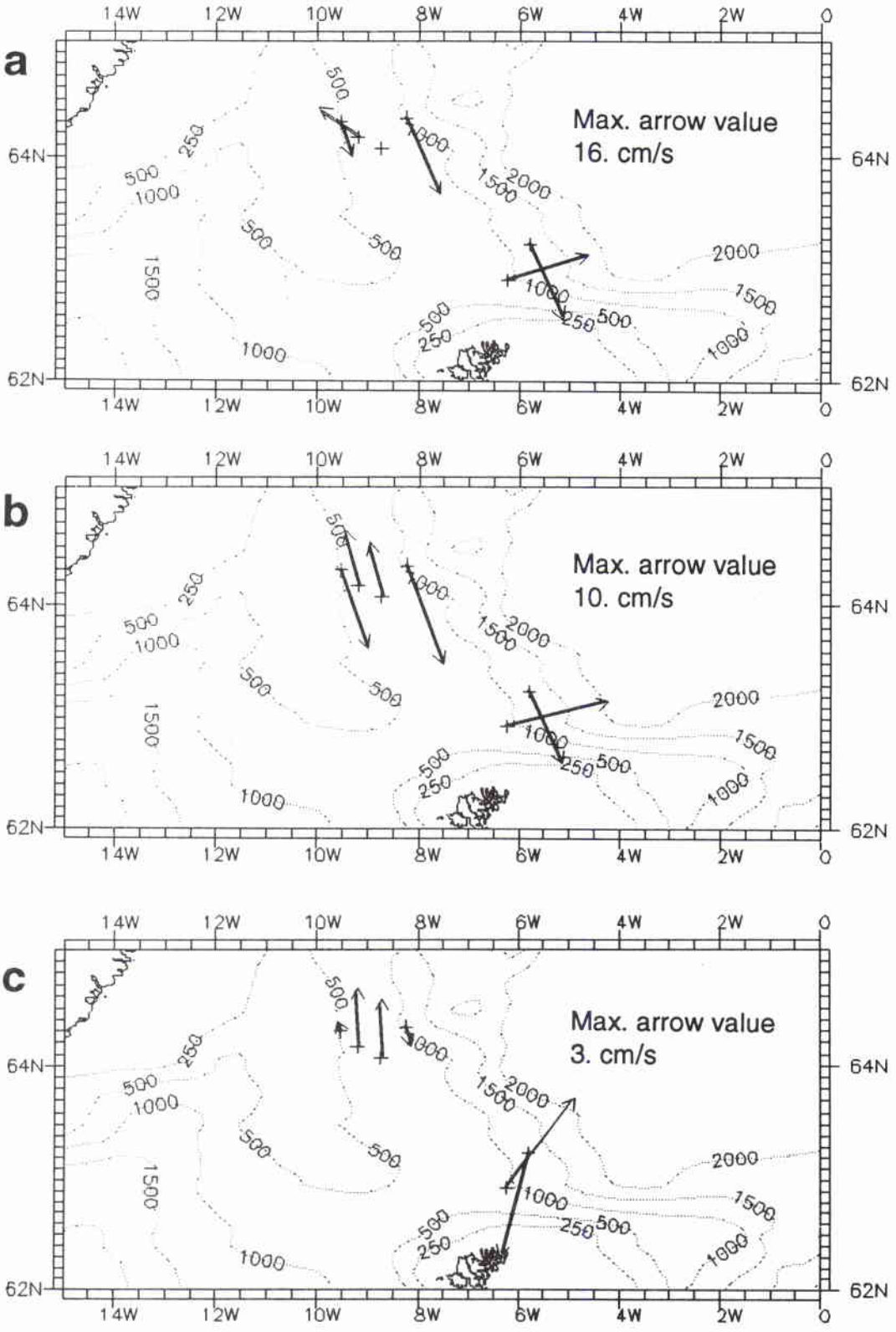

Figure 7 *The velocity vectors computed from the numerical experiments of Part 1. Same as Fig. 6.*

the front location appears much less evident and the region affected by a strong mesoscale activity that is more energetic on the northern side of the ridge. The satellite image shows the formation of a large anticyclonic meander (horizontal scale of about 100 km) filled by warm eddies (horizontal scale of 30 km), and cold eddies (horizontal scale of 10 km). The feature moves northwestwards, and is separated from the main body of NAW by a thin tongue of Artic water less than 15 km wide. The transit of one of the cold eddies corresponds to the marked temperature fluctuations recorded at mooring S09_L00 between June 10–16 (Julian day 161–166).

Given these findings, the region appears to be dominated by the instability of the IFF. Pedlosky (1964a,b) presented an extensive overview of the barotropic and baroclinic instabilities for a zonal current flow confined to the upper layer. The results may be summarized as follows. In the presence of an unstable state, the horizontal Reynolds stresses extract kinetic energy from the mean horizontally sheared flow (barotropic instability), and the vertical Reynolds stress converts the available potential energy into kinetic and potential energy of the perturbed field (baroclinic instability). Assuming that the perturbed field is a superposition of unstable waves, it also follows that the fast-moving, smaller waves gain their source of energy from the available kinetic energy of the mean flow, and the slower-moving large-scale waves from the available potential energy of the mean flow. Finally, one of the conditions necessary for the instability of a zonal current flow requires that lighter fluid must rise and move northwards, and heavier fluid must sink and move southwards.

Indeed, the IFF dynamics present all these features. The character of the instability process is clearly demonstrated by Fig. 2, in which the horizontal scale of the mesoscale fluctuations discloses the origin of the disturbances. Eddies and other small features with a horizontal scale of ~15–20 km (about the length of the local Rossby radius of deformation) are representative of the conversion of the kinetic energy of the mean flow into kinetic energy of the perturbed field. Eddies and meanders of the order of 50 km are related to the available potential energy of the IFF, and also take into account the fluctuations caused by the topographic features of the region.

This mathematical formulation of the instability of zonal current flows, even in its linear approximation, relies on the advective terms that represent the mutual interactions between the mean and perturbed fields. The model of Part 1 neglects this physical mechanism and assumes the flow to be in geostrophic balance, under the hypothesis that the acceleration terms are one order of magnitude smaller than the Coriolis and pressure gradient forces. However, small differences in two large terms, and small errors in computing velocity and pressure fields could lead to large errors in estimating the acceleration, and the geostrophic approximation is most likely to fail.

There are two main reasons for the inaccuracy of the diagnostic model in determining the flow structure in the thermocline region. First, the vertical numerical grid resolution is too coarse for a correct parametrization of the vertical structure of the

thermocline. The CTD observations indicate temperature drops of 2°C and more, in less than 50 m at depths ranging from 200 to 500 m. At these levels the numerical grid uses a vertical resolution of 50 m, which is inadequate. Secondly, there is no guarantee that the observed temperature and salinity distributions satisfy the conditions of the mathematical model formulation. The data contain noise in the measurements, and errors due to the omission of terms dynamically important in the model. The consequent misfit is an additional unknown of the problem. The model of Part 1 defines a solution of the velocity field that minimizes the variance of the misfit. Thus, the mathematical framework has the tendency to smooth the solution in the presence of different water masses governed by different physical processes. Thus the numerical computations are not accurate in the thermocline region of the IFF which separates the upper NAW from the deep Artic water.

5 Summary and conclusions

Statistical analysis of current and temperature time series has revealed information on the kinematic structure of the IFF, and also allows us to speculate on the dynamics governing the motion. The observed currents have dominant signals in the inertial and subinertial frequency band. Tides are highly energetic and strongly anisotropic. After being filtered to remove the inertial frequency, the time series show the low frequency (or 20-day period) band highly energetic, with the energy at least one order of magnitude greater than the other frequency bands. The filtered time series also indicate significant fluctuations with a timescale of about 2–3 days.

A satellite image taken on June 19, 1989 depicts the IFF characterized by a high variability, with mesoscale features on a horizontal scale ranging from 10–50 km. According to mathematical models of the instability of a zonal current flow, the fluctuations of the smaller, and larger features occur on a time period of 2 and 10 days, respectively. These conditions are similar to the observations used by Willebrand and Meincke (1980) to demonstrate that baroclinic instability is the major source of the IFF fluctuations at periods longer than 2 days. Furthermore, Hansen and Meincke (1979) suggested that eddy-like features could be generated by the tendency of the mean flow to follow the isobaths, and features with horizontal scales of the order of 50 km and lifetimes in the 10 day range characterized the topography of the crest zone.

The currentmeter data are used to evaluate the validity of the circulation pattern as described in Part 1. The diagnostic calculation assumes that the hydrographic survey is adequate to describe the synoptic features of the region, and the mathematical framework adequate to represent all the dominant physical mechanisms acting on the IFF dynamics. The computed velocity field is compared with the time series mean values. Unfortunately, the mean values of the records are not representative of the mean flow on a temporal scale of 2 weeks and more. The fluctuations of the observed field give rise to nonlinear process with non-zero time averages, and the structure of the mean flow cannot inevitably be determined by the time averaged state. Thus, the hydrographic data are not sufficient to investigate the kinematics of the IFF on a synoptic time scale.

The numerical solution is then compared with the currentmeter values averaged over a time interval of 3 days centered at the moment at which the closest CTD was taken. It is found that the model of Part 1 is successful in computing the direction and the shear of the flow, but underestimates the magnitude of the velocity vectors. Differences and discrepancies are mainly due to the mathematical formulation of the

model that neglects advective and nonlinear terms, and cannot take into account the instability of a zonal current flow.

It was hoped to combine the information from currentmeter observations, satellite images, and modeling results to outline some of the requirements necessary for forecasting models of the IFF dynamics. Unfortunately, this research is not conclusive and often gives contradictory suggestions. The contributions of this study may be summarized as follows:

1. Real-time analysis of the subsurface structure is traditionally made through rapid XBT/AXBT sections, sometimes combined with a few deep CTD profiles. Representation of the mesoscale structure should consider an observational grid of at least 2–3 samples per the smallest significant feature (i.e. a spacing of 5–10 km over at least $(300\ \text{km})^2$ on the IFR). Remote sensing might supply additional information and restrict the area in which a very fine *in situ* observational grid is needed. Satellite measurements significantly increase the quality and quantity of data acquisition, however they are not sufficient by themselves. The problem of inferring the subsurface structure from knowledge of the sea surface distribution is still an open question. In this study, an attempt has been made to relate the IFF surface location with the intrusion of Artic water over the ridge. Unfortunately, subsurface temperature fluctuations have been found to be not related to surface variations. Acoustic tomography could overcome the limitations of remote sensing data acquisition, but we have no knowledge of any such experiments having yet been conducted in the IFR region.

2. Assuming that the observational program could supply the necessary information on the required spatial and temporal scales, it would still be necessary to link the observations with numerical ocean circulation models capable of parametrizing the sub-grid scale variability. The diagnostic model of Part 1 was conceived to furnish the initial state for time-dependent, evolving models. The model presents a 3D configuration of the ocean as derived from the observational program, and computes the associated velocity field. The data assimilation procedure is consistent with the *in situ* measurements, (i.e., it reproduces the features sufficiently sampled during the observational program with good accuracy). Comparison with currentmeter time series indicates that the model furnishes the *instantaneous* (on a 3-day averaged period) configuration, and stability of the ocean state. However, the model of Part 1 is not completely accurate in defining the dynamic state of the IFF. Differences and discrepancies are mainly due to the omission of nonlinear and diffusive terms, which are usually neglected in the initial state of ocean circulation models. Thus, the solution of Part 1 could be successfully included in regional eddy-resolving circulation models. The main questions are if the solution would represent the mean unperturbed state of the IFF, and how sensitive the instability process would be to the initial state configuration.

3. Regional eddy-resolving models must be able to treat intense, small-scale,

rapidly evolving features, and include physical processes that characterize selected geographical domains. Close to the sea surface, the models must address the problem of air-sea interactions, and other highly energetic surface processes that occur on both a regional and global scale. Even though regional eddy resolving models are able to represent the thermocline structure, and the evolution of major eddies and front meanders, they cannot provide the necessary information on small-scale variability. Regional eddy resolving models could be coupled with statistical/deterministic methods. Unfortunately, the model would be constrained by our lack of confidence in the available covariance function for the climatological (i.e. mean state) and variability of the IFR region. Interpretation and evaluation of the dynamic model results would be a complex and difficult task; it would be impossible to determine whether the computed ocean configuration represents a standard or an unusual event, and infer additional information on the sub-grid scale features.

References

Hansen B and Meincke, J. (1979). Eddies and meanders in the Iceland– Faeroe ridge area. *Deep-Sea Research*, **26A**, 1067–1082.

Koshlyakov, M. N. (1986). Eddies of western boundary currents. *In*: Kamenkovich, V.M., Koshlyakov, M.N. and Monin, A.S. *eds.*, Synoptic Eddies in the Ocean. Dordrecht, Reidel, pp. 208–264.

Monin, A.S. (1986). Stratification and circulation of the ocean. *In*: Kamenkovich, V.M., Koshlyakov, M.N. and Monin, A.S. *eds.*, Synoptic Eddies in the Ocean. Dordrecht, Reidel, pp. 1–33.

Pedlosky, J. (1964a). The stability of currents in the atmosphere and the ocean: Part I. *Journal of the Atmospheric Sciences*, **21**, 201–219.

Pedlosky, J. (1964b). The stability of currents in the atmosphere and the ocean: Part II. *Journal of the Atmospheric Sciences*, **21**, 342–353.

Peggion, G. (1987). A method for determining absolute velocities from hydrographic data, SACLANTCEN SR-114. La Spezia, Italy, SACLANT Undersea Research Centre. [AD B 117 448]

Peggion, G. (1991). Diagnostic calculations for the reconstruction of the environmental and acoustic conditions in the Iceland–Faeroe Ridge region during June 1989, SACLANTCEN SR-178. La Spezia, Italy, SACLANT Undersea Research Centre. [AD B 166 678]

Willebrand, J. and Meincke, J. (1980). Statistical analysis of fluctuations in the Iceland–Scotland frontal zone, *Deep-Sea Research*, **27A**, 1047–1066.

Appendix A

Analysis and treatment of the currentmeter records

Twenty vector-averaging currentmeters (ARCM-7) were deployed at the 6 mooring locations. The nearsurface currentmeter at site 5 was missed at the time of the planned recovery, and no data were obtained. All the other instruments produced good records for the duration of the experiment, except mooring S07_L02 which recorded good compass data, but temperature values out of calibration. Since at the time of this study, conductivity/salinity data have not yet been calibrated, this research is based on velocity and temperature records only. The instruments were set to sample at 30 min intervals, and the OTS checked carefully for gaps and bad points using the 'currentmeter software package' developed at SACLANTCEN. Unless otherwise specified, no rotation of the coordinate system is done: the u component is positive eastwards, and the v component northwards, and angles are referred to the usual complex plane orientation with the brunch cut line along the negative real axis (angle values are ranging from $-180°$–$180°$). These half-hour series were low-passed using a digital Butterworth filter with a cutoff frequency at 48 h to remove tidal and inertial energy. These series were resampled at a 24 h time-interval, and henceforth referred to as two-day low-pass filtered (LPF2). Finally, the LPF2 time series were low-passed again using a digital Butterworth filter with a 10-day cutoff frequency (LPF10).

A spectral analysis was carried out to examine the distribution of energy as a function of frequency for the LPF2 time series. To obtain the greatest possible statistical confidence, the correlation functions are computed using a lag window of 25 days, which is equivalent to assuming about 13 degrees of freedom for each data set.

Values of the statistical functions of each record are summarized in Table A1a–s. The time series plots for the nineteen currentmeter records are illustrated in Figs. A1–A19. Each figure presents a) OTS, b) LPF2, c) LPF10, and d) the autospectra for the LPF2 time series of eastward velocity, poleward velocity, temperature and kinetic energy.

Table A1 *Values of statistical functions for the eastward velocity, poleward velocity, and temperature time series for each currentmeter mooring (the fourth rows correspond to the LPF10 time series for the period 5–28 June, 1989)*

		Maximum	Minimum	Mean	Stand. Dev.
(a) S02_L00 (p = 91 dB)					
E–W Vel.	OTS	215.47	−89.61	50.68	41.65
	LPF2	160.66	−33.15	48.72	33.09
	LPF10	98.30	−11.07	45.75	26.33
		62.76	−29.20	41.89	10.68
N–S Vel.	OTS	133.65	−109.11	−2.22	37.54
	LPF2	83.48	−70.42	−0.23	31.12
	LPF10	50.24	−55.04	−0.64	24.56
		34.97	−55.04	−2.29	27.80
Temp.	OTS	9.47	5.50	8.01	0.45
	LPF2	8.73	6.30	8.02	0.43
	LPF10	8.67	6.50	7.91	0.55
		8.10	7.19	7.85	0.20
(b) S02_L01 (p = 265 dB)					
E–W Vel.	OTS	153.51	−84.44	41.17	33.88
	LPF2	103.18	−23.38	39.77	24.98
	LPF10	74.97	−14.61	38.40	20.70
		57.06	24.96	38.03	9.92
N–S Vel.	OTS	112.94	−102.08	0.96	32.43
	LPF2	69.44	−62.15	2.26	25.44
	LPF10	41.31	−44.76	2.12	20.03
		35.03	−44.76	−3.25	25.75
Temp.	OTS	8.93	2.04	6.81	1.26
	LPF2	8.09	3.71	6.95	1.09
	LPF10	7.93	4.73	7.04	0.83
		7.87	5.73	7.35	0.51
(c) S02_L02 (p = 522 dB)					
E–W Vel.	OTS	110.14	−78.89	7.69	25.04
	LPF2	73.51	−38.70	6.22	17.67
	LPF10	35.69	−15.27	5.93	12.28
		18.32	−14.25	0.56	12.27
N–S Vel.	OTS	77.69	−47.09	4.51	13.96
	LPF2	48.03	−13.61	4.76	9.25
	LPF10	30.55	−3.77	4.76	6.32
		30.55	−3.77	8.78	11.11
Temp.	OTS	4.26	−0.50	0.80	1.05
	LPF2	3.60	−0.41	0.86	1.02
	LPF10	3.08	−0.39	0.88	0.96
		2.25	0.87	1.55	0.50

Table A1 *(Cont'd)*

		Maximum	Minimum	Mean	Stand. Dev.
(d) S03_L00 (p = 184 dB)					
E–W Vel.	OTS	153.06	−93.08	15.20	37.75
	LPF2	131.29	−43.99	17.02	35.54
	LPF10	100.76	−33.87	17.76	33.32
		47.92	7.20	30.37	12.95
N–S Vel.	OTS	110.51	−147.06	−0.62	33.06
	LPF2	72.43	−93.43	−0.80	30.17
	LPF10	58.21	−69.48	−1.17	26.78
		−0.99	−69.48	−28.31	23.69
Temp.	OTS	7.91	1.58	5.85	1.85
	LPF2	7.86	1.96	5.97	1.83
	LPF10	7.72	2.92	5.80	1.98
		7.02	3.00	5.35	1.37
(e) S03_L01 (p = 353 dB)					
E–W Vel.	OTS	76.47	−64.45	2.16	19.24
	LPF2	51.15	−32.99	2.73	15.81
	LPF10	34.75	−28.44	3.09	13.43
		16.14	0.63	9.54	4.80
N–S Vel.	OTS	79.38	−79.42	1.44	19.97
	LPF2	51.39	−52.44	1.63	16.55
	LPF10	46.54	−27.47	1.68	14.88
		4.18	−27.47	−8.82	10.66
Temp.	OTS	4.98	0.20	2.08	0.95
	LPF2	3.93	0.37	2.20	0.84
	LPF10	3.30	0.37	2.18	0.61
		2.69	1.24	1.86	0.37
(f) S03_L02 (p = 623 dB)					
E–W Vel.	OTS	56.47	−48.87	−0.29	13.30
	LPF2	28.99	−28.56	−0.06	9.27
	LPF10	12.67	−17.92	0.23	6.92
		9.54	1.22	5.48	2.52
N–S Vel.	OTS	48.84	−47.47	−0.43	12.12
	LPF2	26.91	−17.53	−0.24	8.34
	LPF10	22.52	−10.13	0.12	7.27
		2.44	−10.05	−2.74	4.11
Temp.	OTS	0.95	−0.53	0.01	0.28
	LPF2	0.57	−0.44	0.03	0.25
	LPF10	0.45	−0.36	0.05	0.22
		0.09	−0.10	−0.02	–

Table A1 *(Cont'd)*

		Maximum	Minimum	Mean	Stand. Dev.
(g) S03_L03 (p = 1502 dB)					
E–W Vel.	OTS	53.05	−44.36	−0.24	13.71
	LPF2	22.57	−20.93	−0.14	9.50
	LPF10	9.37	−8.18	−0.04	4.04
		5.89	−5.85	0.77	3.84
N–S Vel.	OTS	38.16	−43.17	−1.64	10.95
	LPF2	20.25	−23.04	−1.49	8.08
	LPF10	15.02	−17.31	−1.29	6.18
		0.70	−8.95	−3.22	2.94
Temp.	OTS	−0.73	−0.93	−0.85	–
	LPF2	−0.76	−0.96	−0.85	–
	LPF10	−0.79	−0.93	−0.82	–
		−0.79	−0.83	−0.82	–
(h) S05_L01 (p = 257 dB)					
E–W Vel.	OTS	74.75	−65.64	−4.03	23.16
	LPF2	19.25	−30.80	−4.14	11.12
	LPF10	17.07	−27.05	−4.27	9.75
		0.11	−27.05	−12.99	9.01
N–S Vel.	OTS	80.76	−69.54	6.07	22.02
	LPF2	28.99	−14.76	6.12	9.84
	LPF10	23.60	−12.33	6.33	8.99
		18.22	3.64	13.66	4.12
Temp.	OTS	5.71	0.14	2.86	1.46
	LPF2	5.02	0.61	2.87	1.14
	LPF10	4.83	0.66	2.85	1.35
		4.83	3.53	4.26	0.46
(i) S05_L02 (p = 524 dB)					
E–W Vel.	OTS	74.75	−72.43	1.90	22.06
	LPF2	21.46	−11.90	1.41	6.29
	LPF10	7.98	−6.51	1.03	3.65
		2.83	−6.33	−1.89	2.65
N–S Vel.	OTS	81.22	−71.21	0.20	22.93
	LPF2	15.21	−11.75	0.43	4.93
	LPF10	5.61	−9.10	0.57	3.22
		5.61	−0.24	3.56	1.49
Temp.	OTS	0.21	−0.52	−0.25	–
	LPF2	0.21	−0.44	−0.25	–
	LPF10	−0.04	−0.41	−0.24	–
		−0.04	−0.22	−0.11	–

Table A1 *(Cont'd)*

		Maximum	Minimum	Mean	Stand. Dev.
(j) S06_L00 (p = 48 dB)					
E–W Vel.	OTS	136.49	−72.67	20.94	29.87
	LPF2	106.33	−20.21	21.34	20.69
	LPF10	69.04	−14.11	20.76	18.36
		69.04	18.51	8.33	16.22
N–S Vel.	OTS	118.27	−106.74	1.37	34.33
	LPF2	65.83	−67.92	1.24	24.07
	LPF10	51.98	−57.30	1.43	21.55
		10.03	−57.30	−26.33	21.70
Temp.	OTS	10.11	3.38	7.27	1.11
	LPF2	9.18	3.47	7.30	1.02
	LPF10	8.83	5.53	7.06	1.85
		7.93	5.23	6.76	0.92
(k) S06_L01 (p = 212 dB)					
E–W Vel.	OTS	79.13	−60.47	7.38	18.37
	LPF2	53.45	−39.40	7.61	13.70
	LPF10	45.44	−14.92	7.51	12.16
		45.44	8.48	21.58	11.72
N–S Vel.	OTS	87.64	−78.88	1.05	22.35
	LPF2	43.67	−34.00	1.00	14.17
	LPF10	33.44	−25.66	1.15	12.48
		9.22	−25.66	−9.84	10.26
Temp.	OTS	6.50	0.76	2.82	1.13
	LPF2	5.55	0.81	2.84	1.25
	LPF10	5.32	0.81	2.76	1.18
		4.84	1.51	2.83	1.16
(l) S06_L02 (p = 476 dB)					
E–W Vel.	OTS	41.66	−40.64	0.38	10.03
	LPF2	13.52	−9.71	0.40	4.34
	LPF10	10.99	−7.74	0.45	3.56
		10.99	0.25	4.41	3.50
N–S Vel.	OTS	54.10	−52.88	−0.57	12.56
	LPF2	14.88	−16.00	−0.55	6.34
	LPF10	12.59	−12.40	−0.53	5.38
		12.59	−3.53	2.35	5.34
Temp.	OTS	0.99	−0.24	0.03	0.14
	LPF2	0.61	−0.14	0.03	0.13
	LPF10	0.38	−0.11	0.03	0.12
		0.38	−0.11	0.10	0.13

Table A1 *(Cont'd)*

		Maximum	Minimum	Mean	Stand. Dev.
(m) (p = 1488 dB)					
E–W Vel.	OTS	40.42	−39.89	0.38	10.33
	LPF2	12.72	−8.45	0.39	3.70
	LPF10	5.76	−5.91	0.39	2.04
		5.76	−1.50	1.04	2.22
N–S Vel.	OTS	37.55	−35.83	−0.32	10.42
	LPF2	9.10	−17.01	−0.25	5.06
	LPF10	5.53	−9.48	−0.35	3.24
		2.34	−6.21	−0.01	2.94
Temp.	OTS	−0.80	−0.96	−0.85	–
	LPF2	−0.81	−0.96	−0.85	–
	LPF10	−0.83	−0.96	−0.83	–
		−0.83	−0.96	−0.86	–
(n) (p = 118 dB)					
E–W Vel.	OTS	161.84	−122.35	2.55	41.42
	LPF2	107.81	−76.47	2.18	30.26
	LPF10	75.51	−54.19	2.25	27.77
		27.29	−4.44	13.19	11.31
N–S Vel.	OTS	104.44	−141.05	−23.63	42.90
	LPF2	61.16	−95.43	−24.68	32.60
	LPF10	34.47	−83.16	−24.87	28.49
		31.46	−66.74	−18.09	27.20
Temp.	OTS	8.13	1.20	6.94	1.31
	LPF2	7.99	2.53	6.94	1.22
	LPF10	7.95	2.53	6.69	1.11
		7.62	3.83	6.31	1.33
(o) S07_L01 (p = 282 dB)					
E–W Vel.	OTS	108.87	−128.88	−2.07	38.03
	LPF2	43.83	−39.28	−2.16	14.67
	LPF10	30.26	−24.25	−1.90	11.62
		14.31	−9.13	2.68	8.39
N–S Vel.	OTS	107.28	−123.73	−11.88	39.16
	LPF2	26.33	−42.42	−12.63	14.11
	LPF10	6.58	−32.13	−12.75	10.21
		2.21	−24.99	−11.49	7.86
Temp.	OTS	6.86	−0.13	2.20	1.45
	LPF2	5.96	0.27	2.21	1.36
	LPF10	5.83	0.27	2.15	1.32
		4.11	0.41	2.34	1.26

Table A1 *(Cont'd)*

		Maximum	Minimum	Mean	Stand. Dev.
(p) S07_L02 (p = 548 dB)					
E–W Vel.	OTS	83.17	−140.58	−11.76	32.02
	LPF2	25.31	−42.16	−12.00	12.68
	LPF10	5.62	−27.29	−11.36	6.44
		−6.37	−23.61	−14.01	5.17
N–S Vel.	OTS	80.81	−95.03	−3.33	28.61
	LPF2	26.06	−33.41	−3.63	12.55
	LPF10	10.37	−18.07	−3.43	5.25
		−1.69	−13.93	−7.17	3.61
(q) S09_L00 (p = 86 dB)					
E–W Vel.	OTS	91.08	−126.55	−9.36	35.40
	LPF2	61.90	−59.03	−8.97	23.34
	LPF10	58.83	−50.06	−7.37	19.04
		−8.35	−30.21	−20.01	5.72
N–S Vel.	OTS	117.98	−154.74	2.45	42.66
	LPF2	80.42	−97.91	2.55	32.56
	LPF10	65.72	−77.88	2.46	30.72
		64.68	−1.47	36.06	21.27
Temp.	OTS	8.15	3.21	6.82	0.93
	LPF2	7.92	3.74	6.73	1.10
	LPF10	7.70	3.74	6.75	0.70
		7.54	5.01	6.53	0.94
(r) S09_L01 (p = 249 dB)					
E–W Vel.	OTS	79.97	−93.24	−4.88	25.10
	LPF2	31.32	−38.46	−4.78	11.81
	LPF10	20.80	−23.67	−4.22	8.67
		−9.26	−15.08	−12.57	1.89
N–S Vel.	OTS	100.18	−88.59	2.67	27.52
	LPF2	32.52	−25.50	2.77	12.36
	LPF10	25.00	−17.51	2.93	11.24
		23.17	2.39	15.84	7.99
Temp.	OTS	6.67	0.21	2.30	1.46
	LPF2	5.54	0.50	2.30	1.42
	LPF10	5.08	0.58	2.24	1.38
		4.63	0.84	2.91	1.33

Table A1 *(Cont'd)*

		Maximum	Minimum	Mean	Stand. Dev.
(s) S09_L02 (p = 585 dB)					
E–W Vel.	OTS	71.36	−60.60	−0.70	25.54
	LPF2	29.38	−42.47	−0.68	11.32
	LPF10	7.10	−14.31	−0.99	3.71
		2.37	−6.96	−1.61	2.89
N–S Vel.	OTS	56.39	−60.60	1.29	21.66
	LPF2	14.43	−11.60	1.32	5.17
	LPF10	8.20	−4.62	1.60	2.81
		4.75	−1.01	1.94	1.73
Temp.	OTS	−0.03	−0.57	−0.42	–
	LPF2	−0.18	−0.54	−0.41	–
	LPF10	−0.01	−0.56	−0.42	–
		−0.37	−0.50	−0.47	–

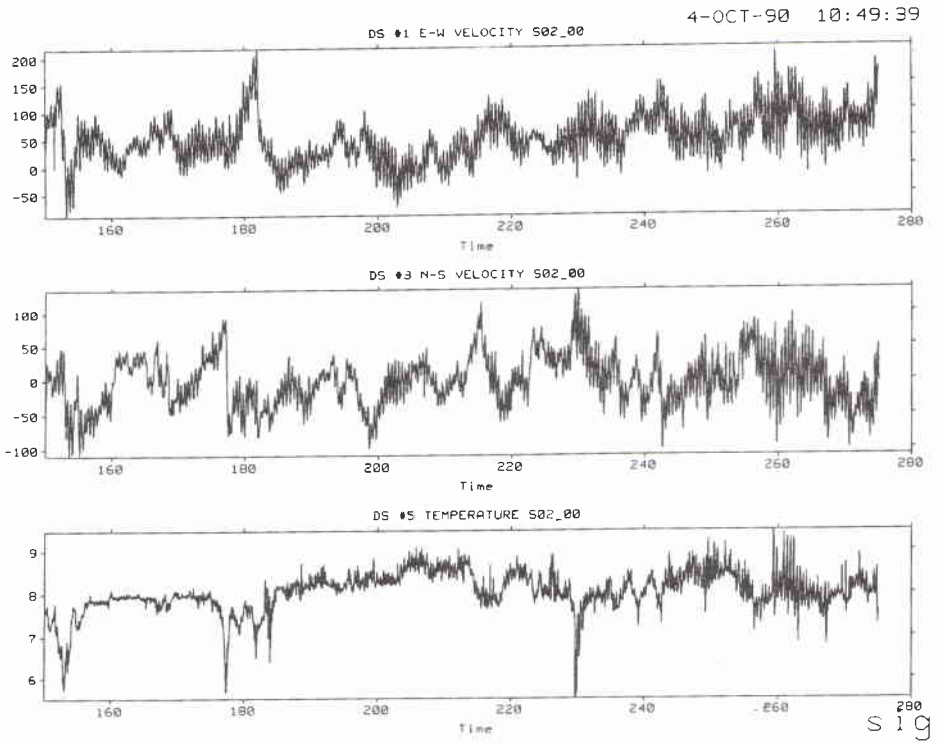

Figure A1a

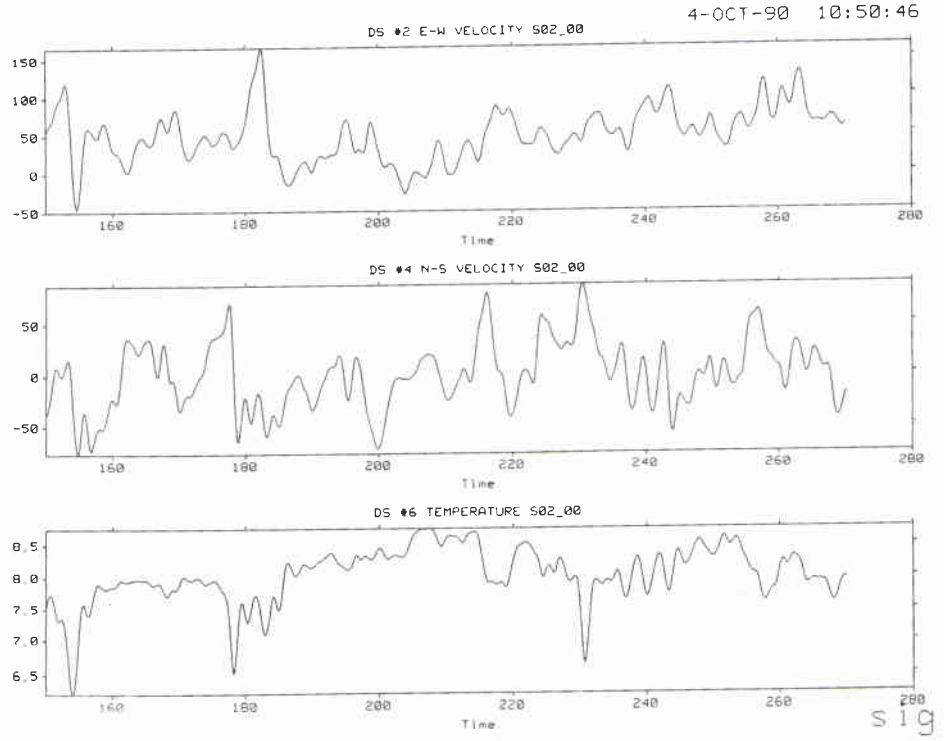

Figure A1b

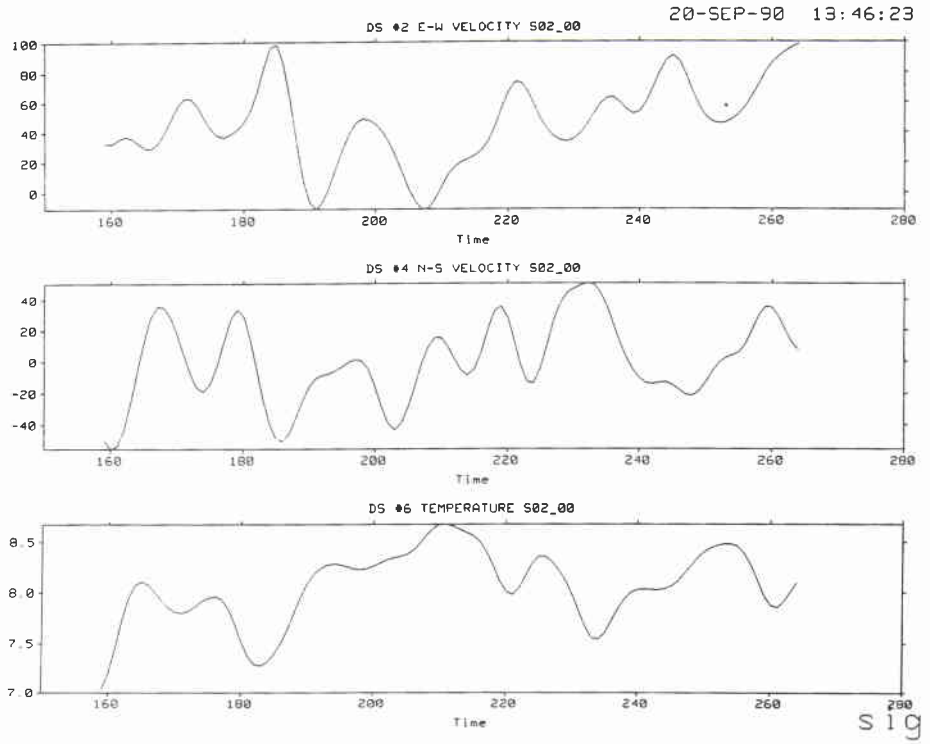

Figure A1c

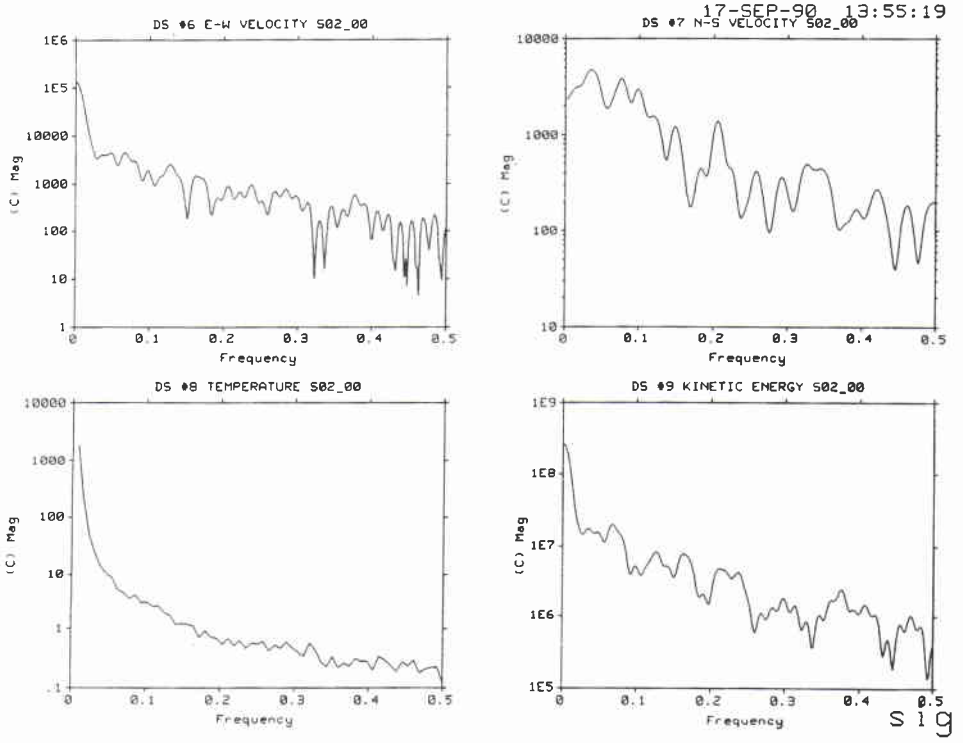

Figure A1d

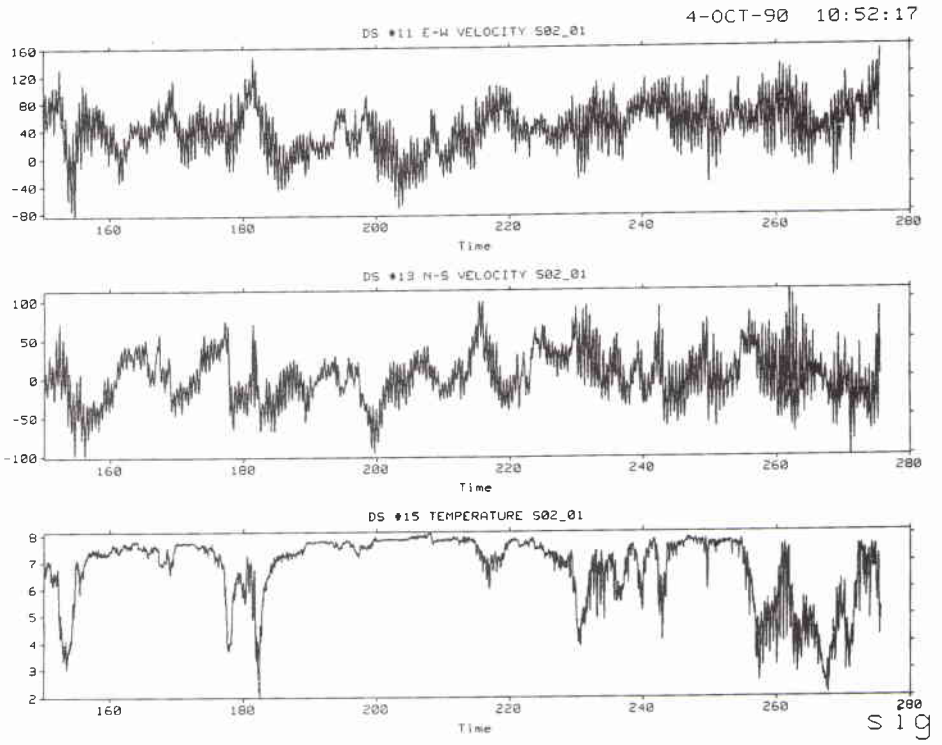

Figure A2a

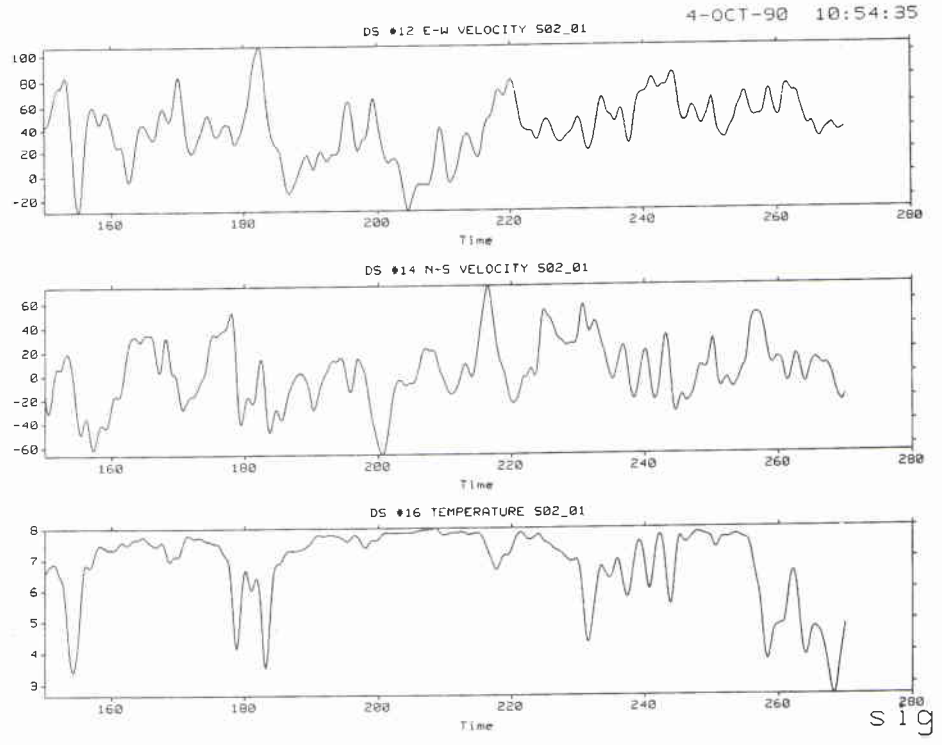

Figure A2b

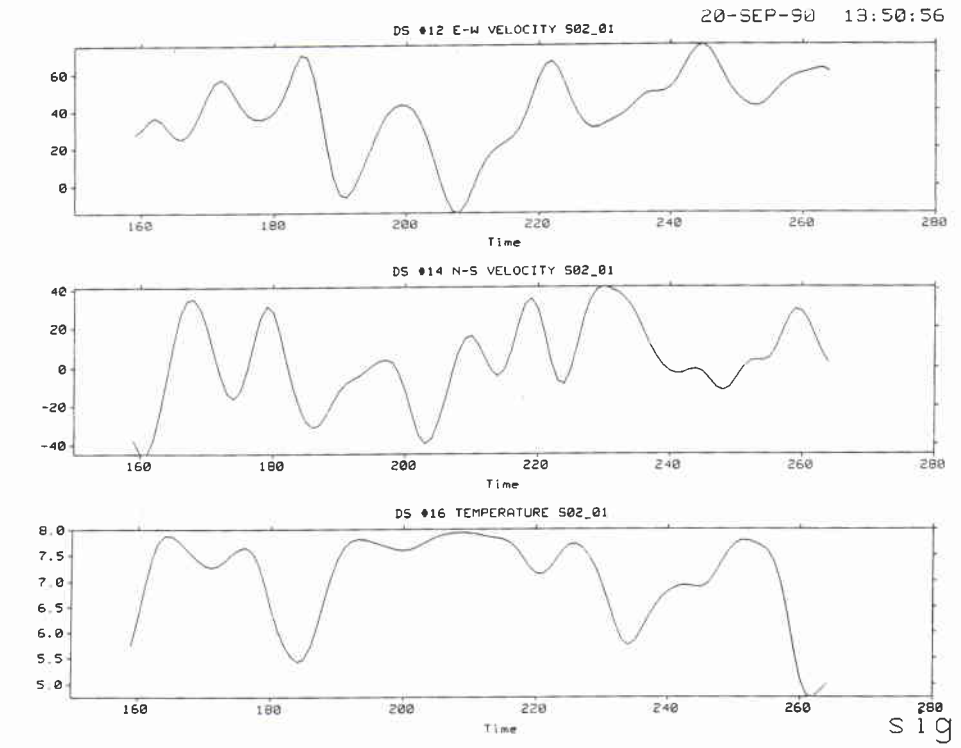

Figure A2c

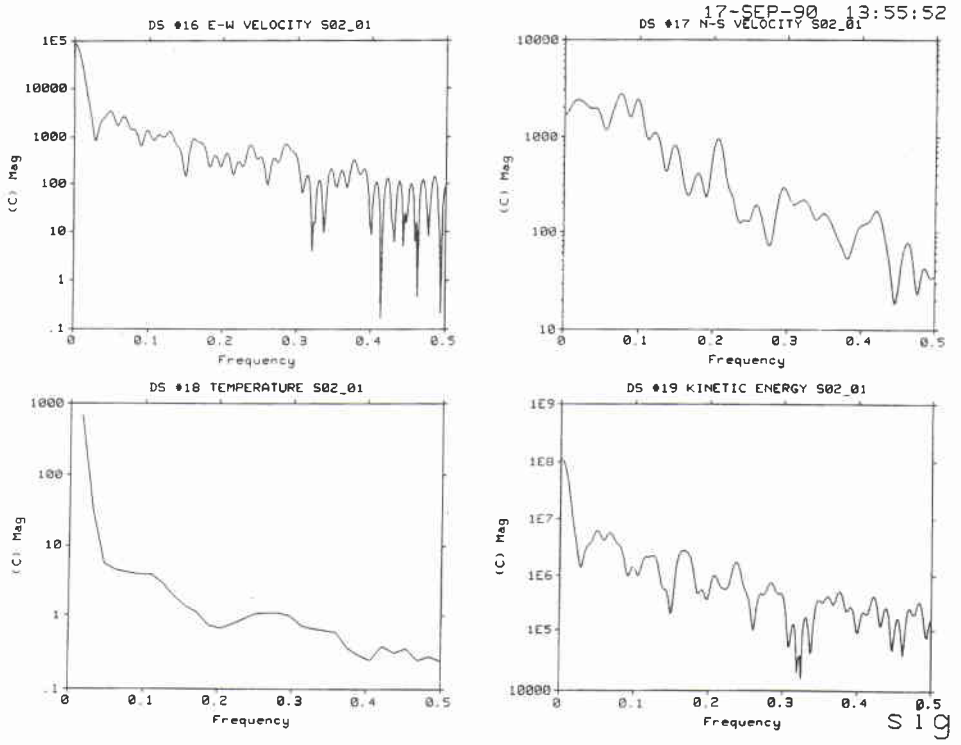

Figure A2d

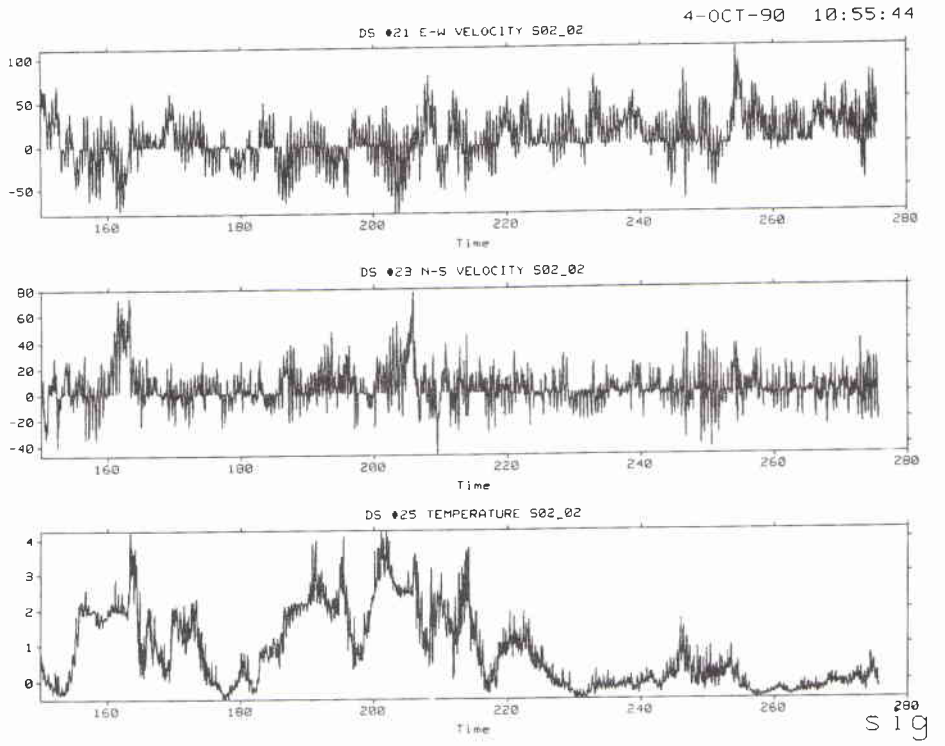

Figure A3a

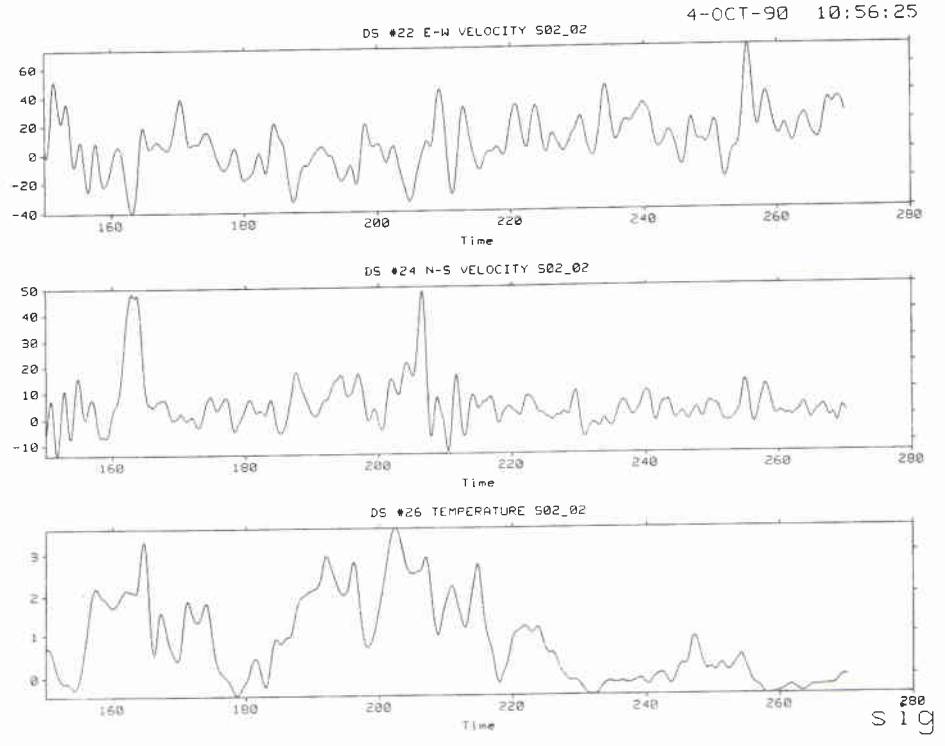

Figure A3b

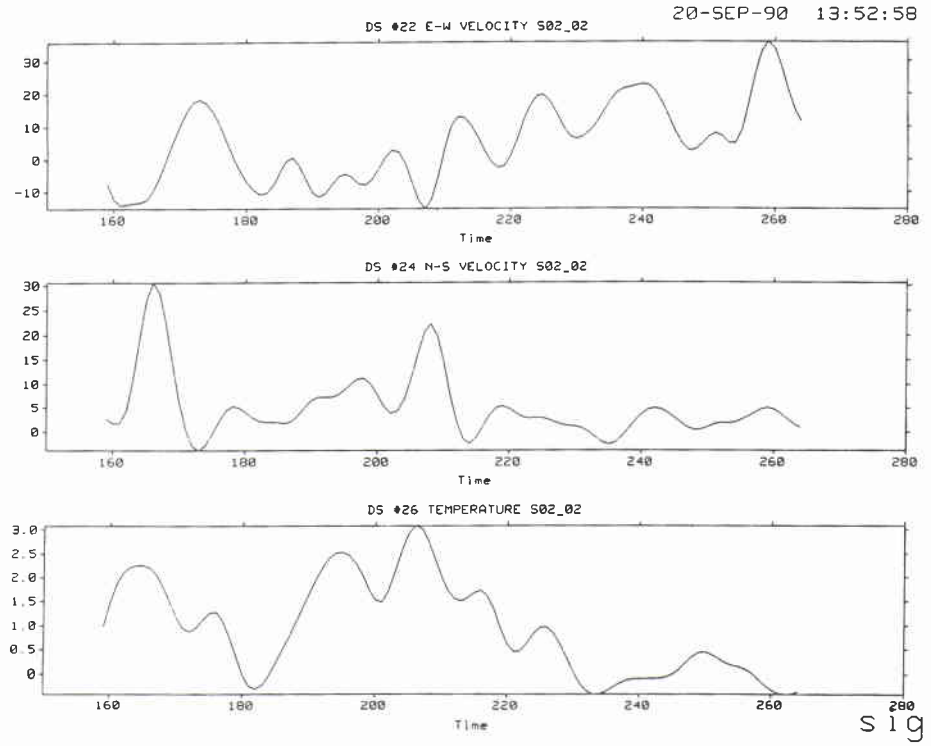

Figure A3c

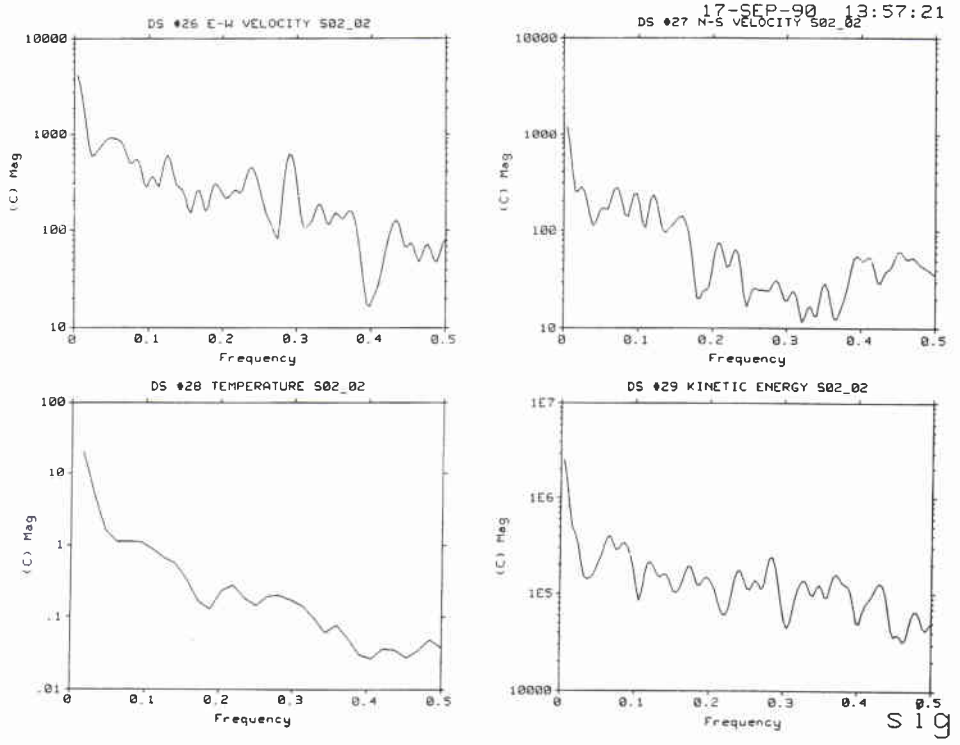

Figure A3d

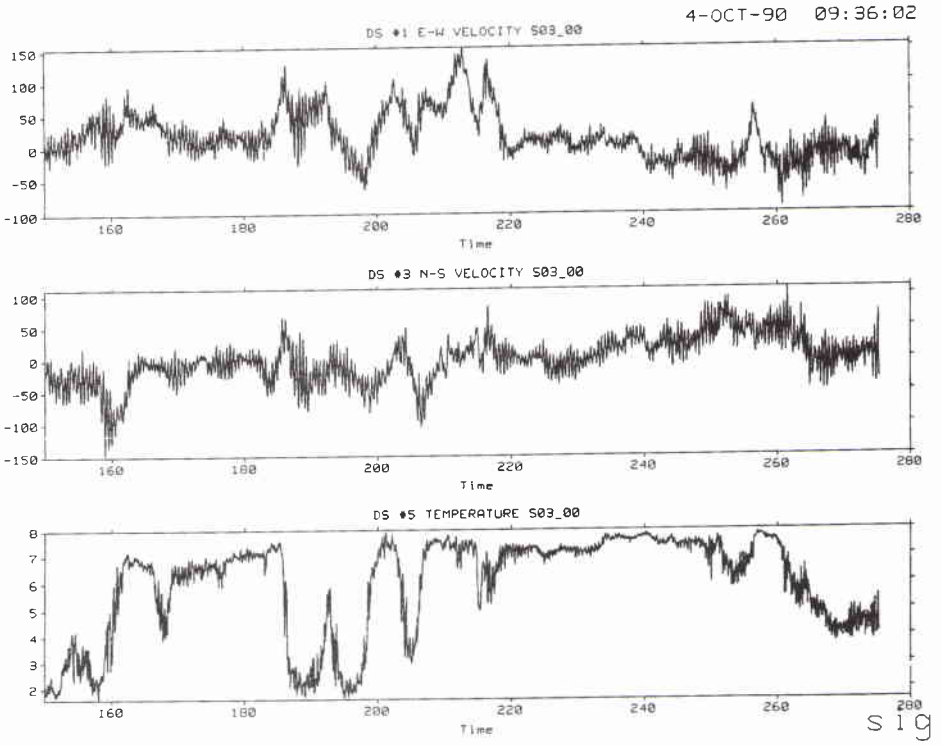

Figure A4a

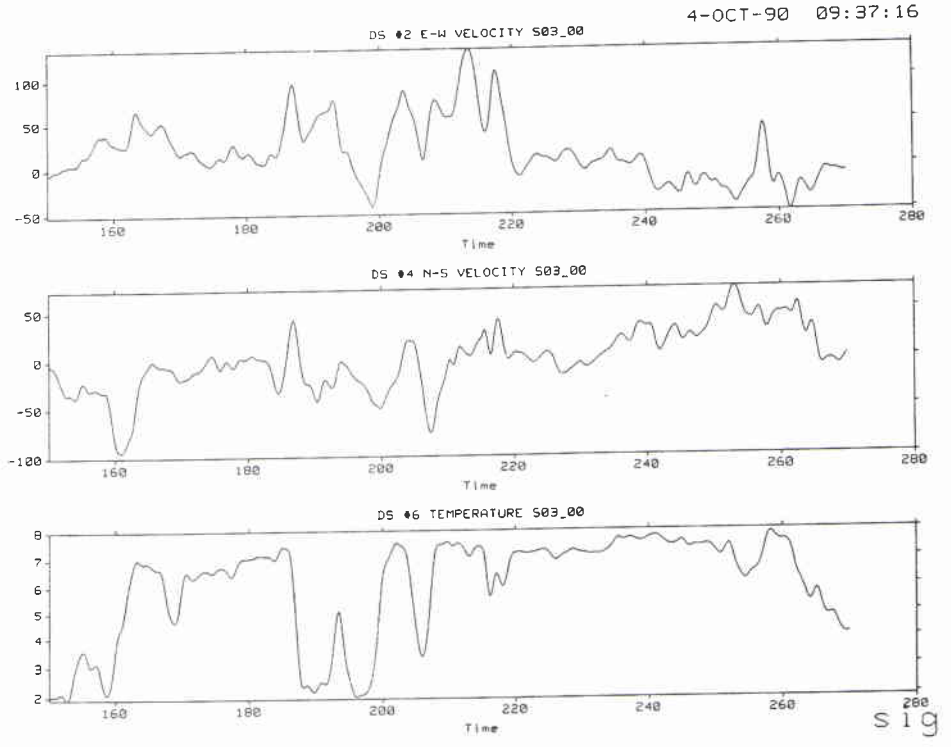

Figure A4b

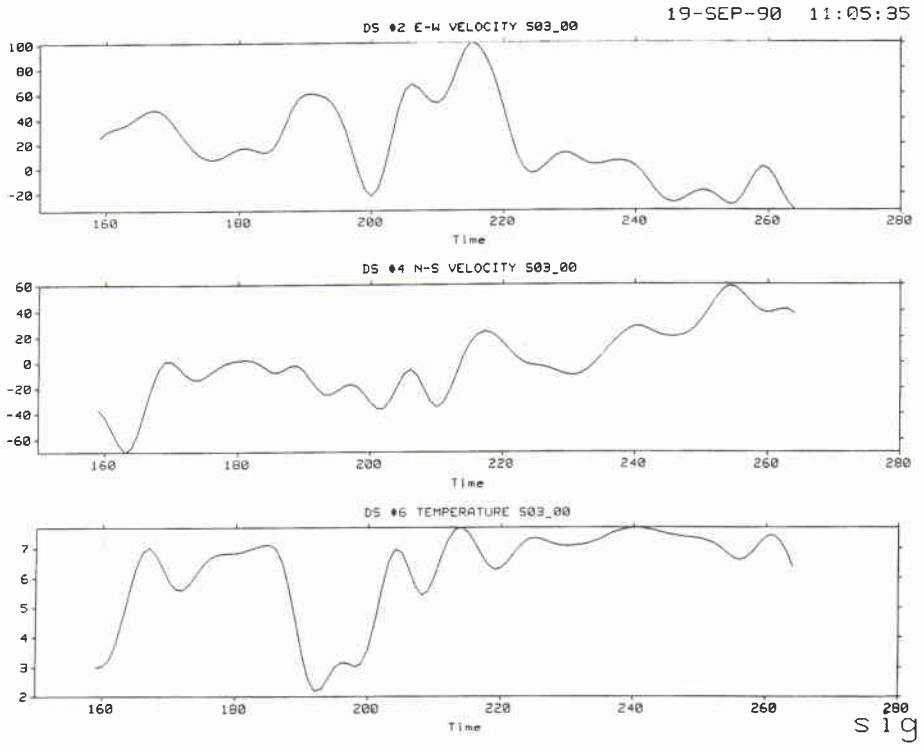

Figure A4c

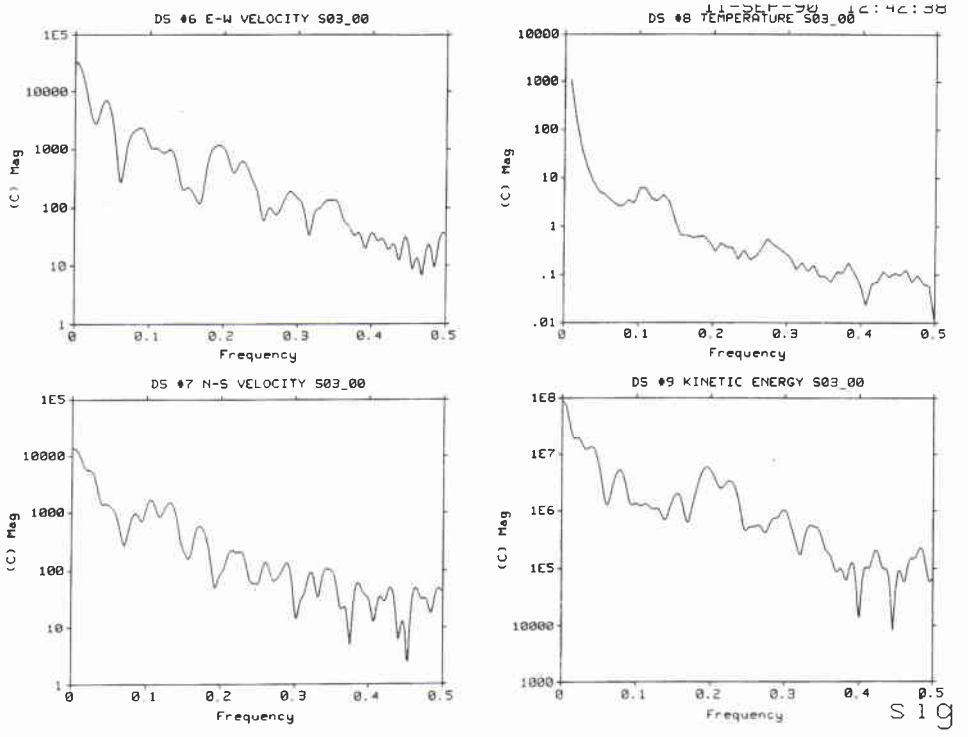

Figure A4d

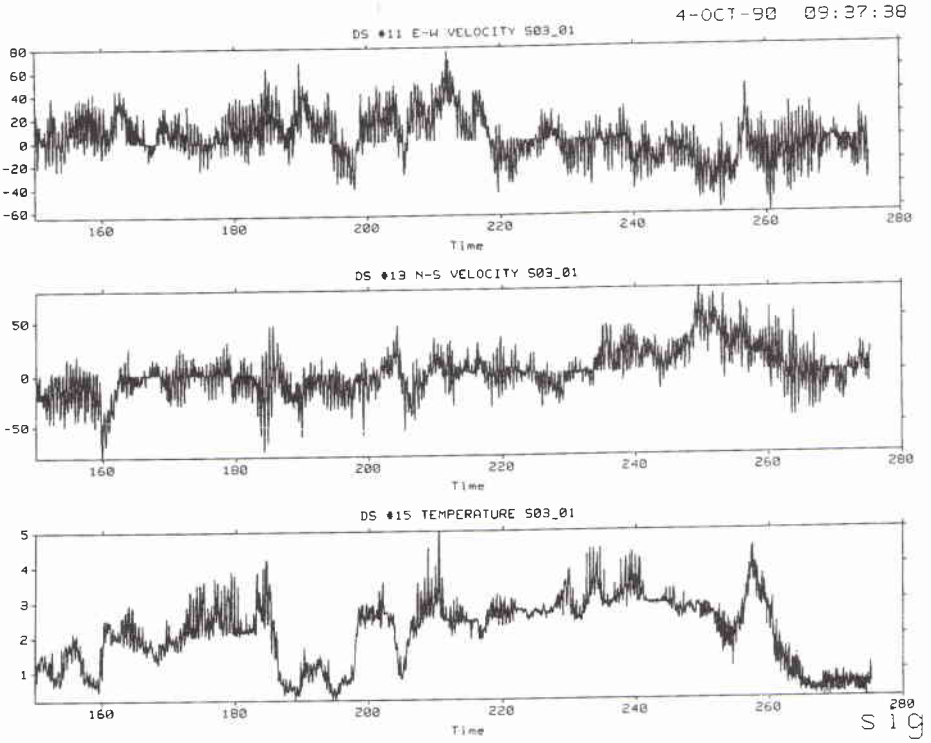

Figure A5a

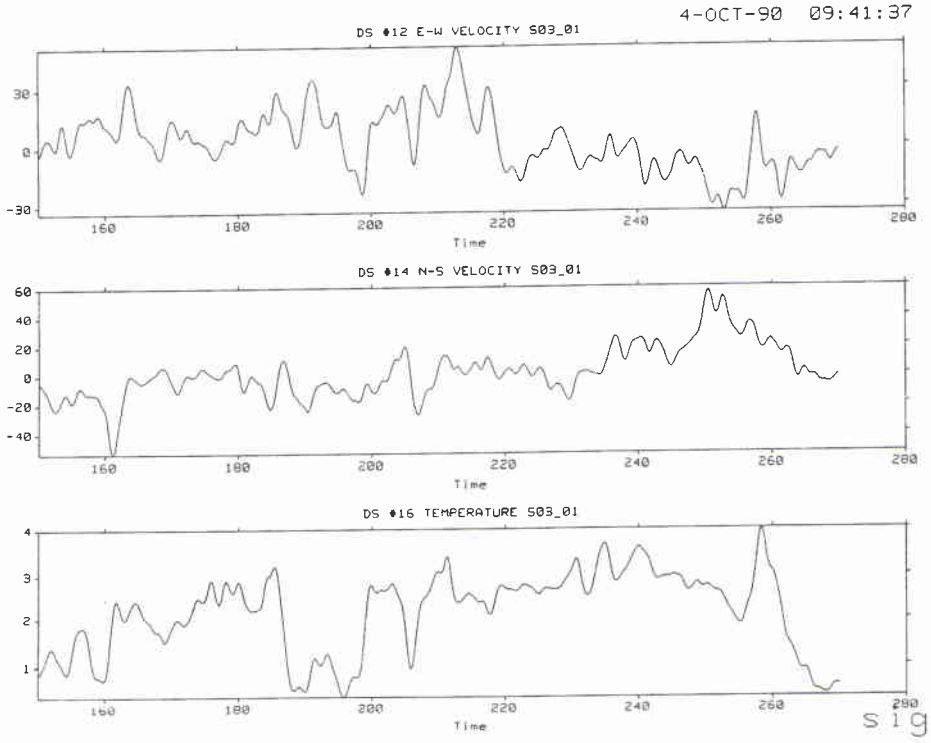

Figure A5b

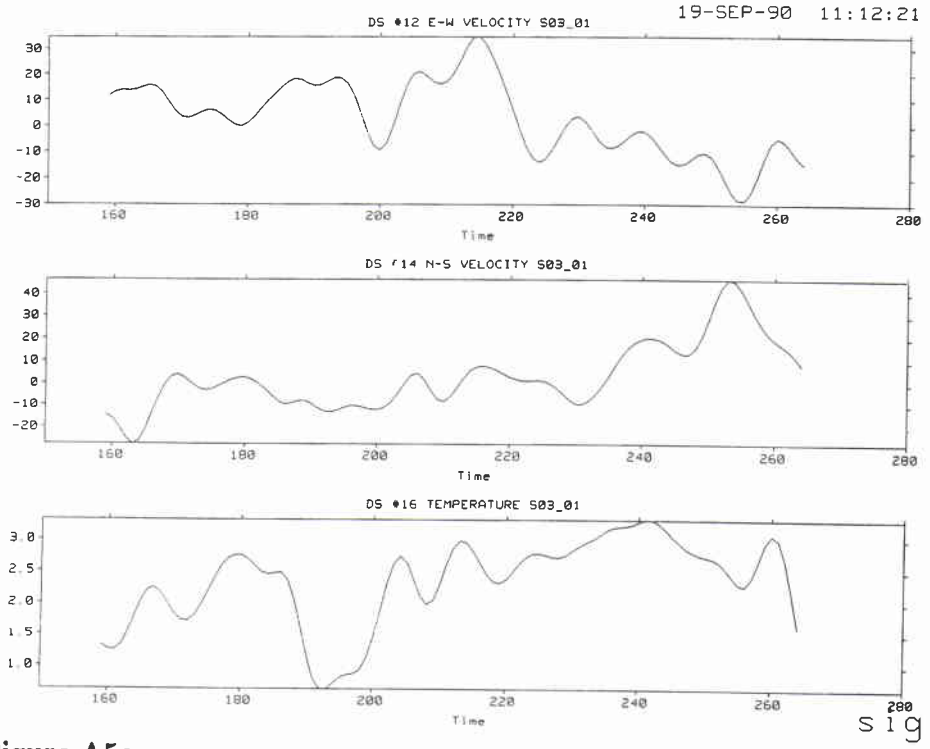

Figure A5c

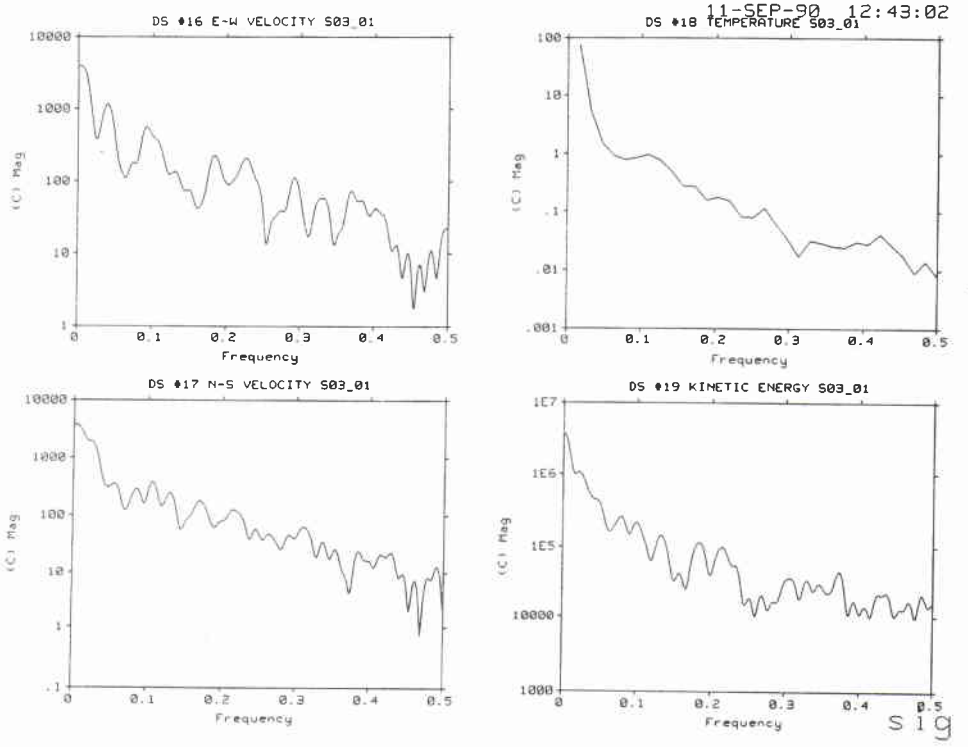

Figure A5d

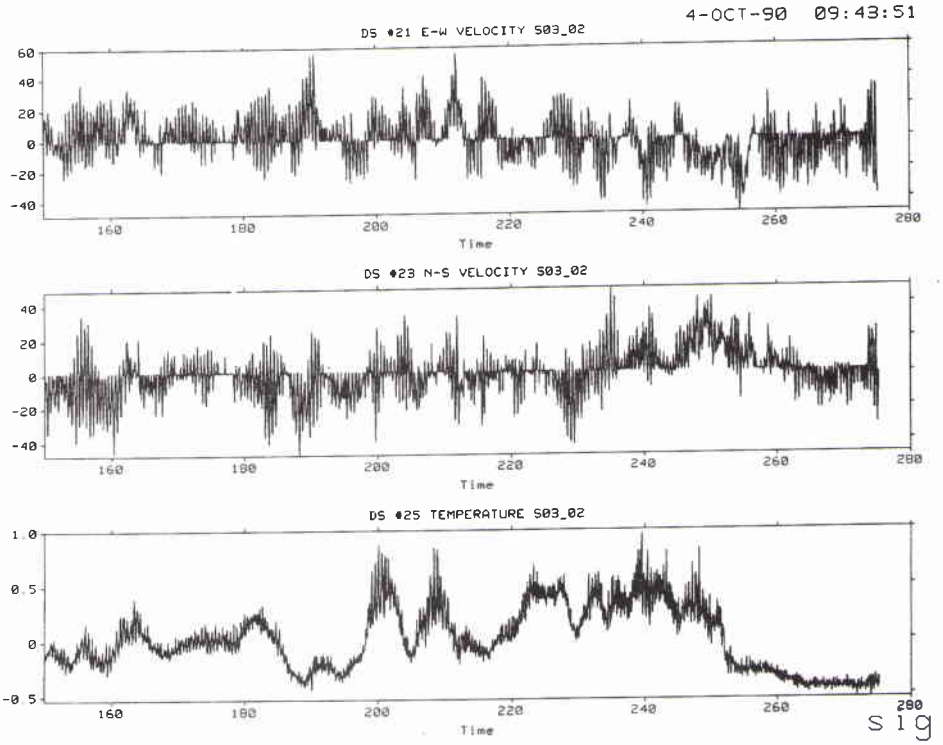

Figure A6a

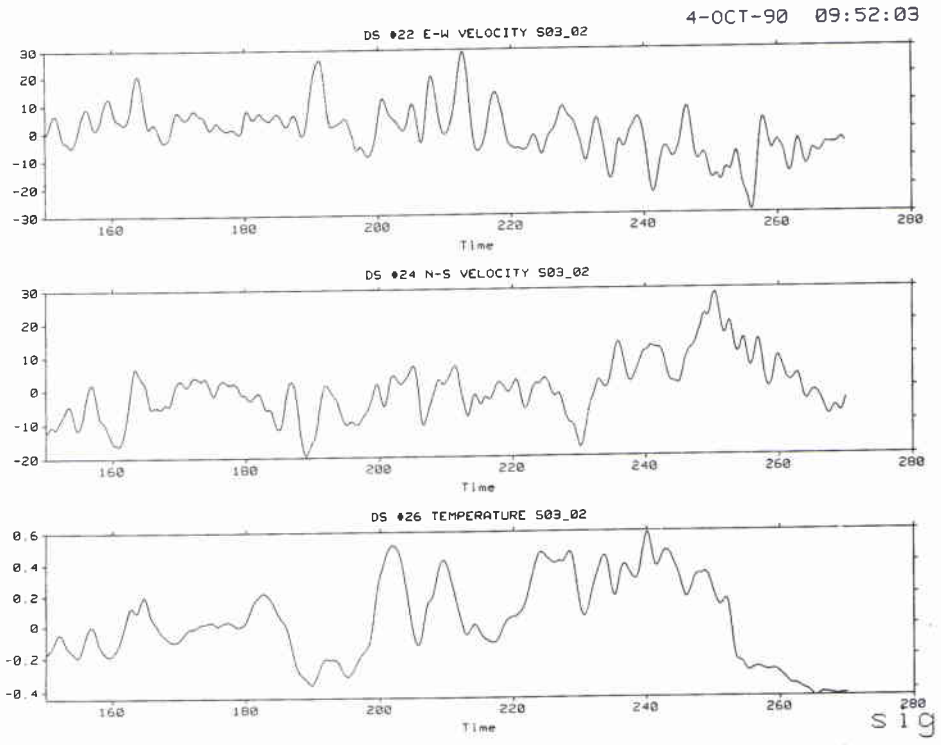

Figure A6b

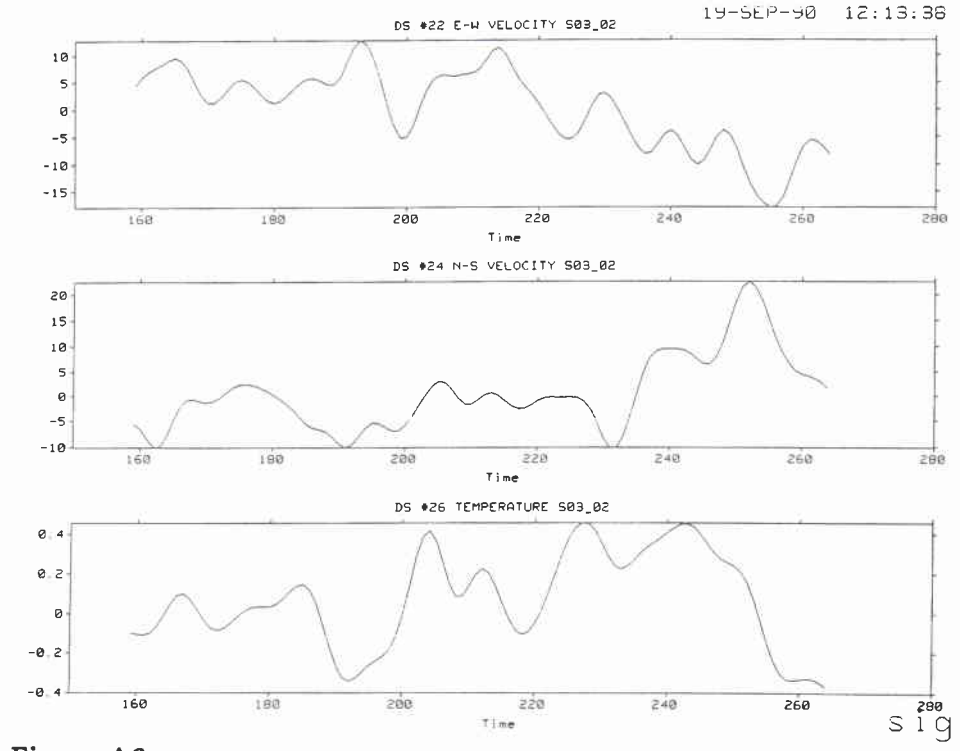

Figure A6c

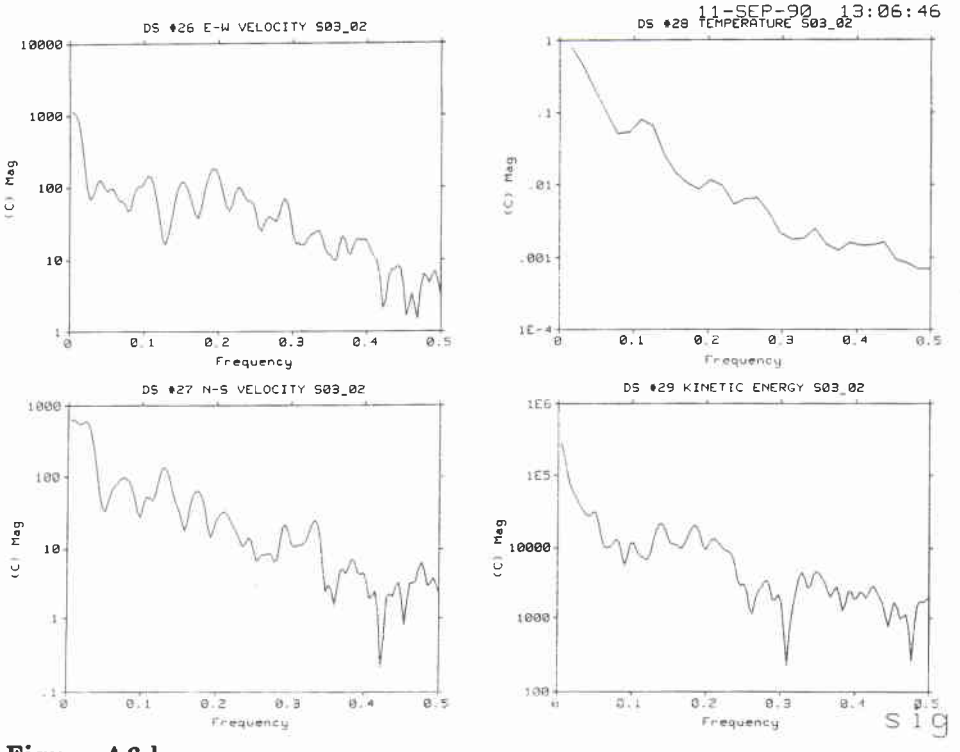

Figure A6d

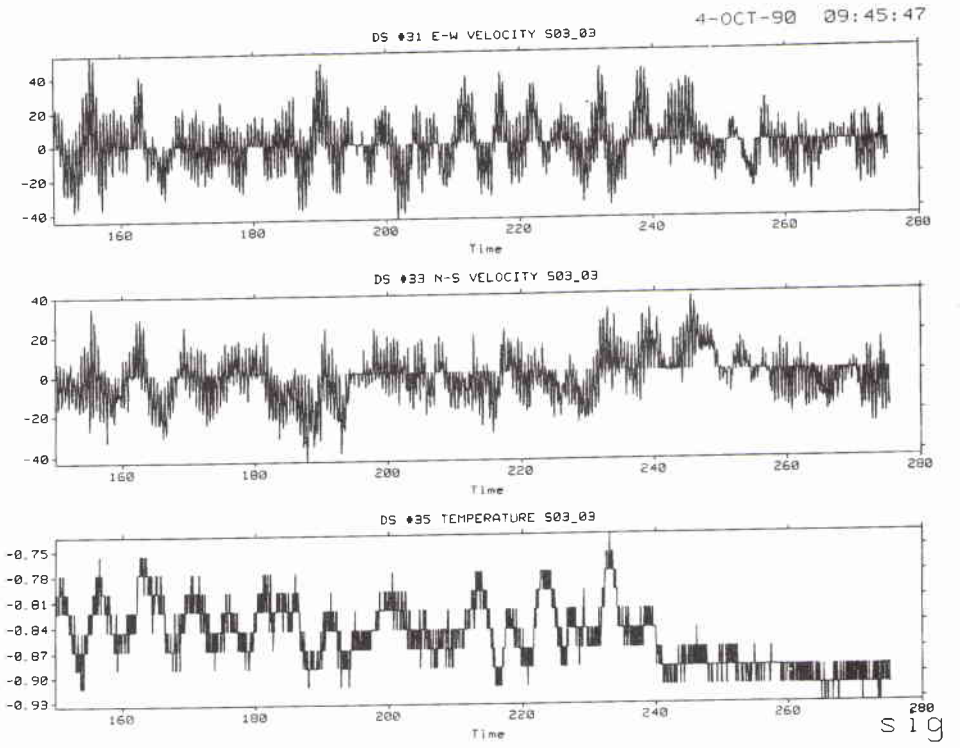

Figure A7a

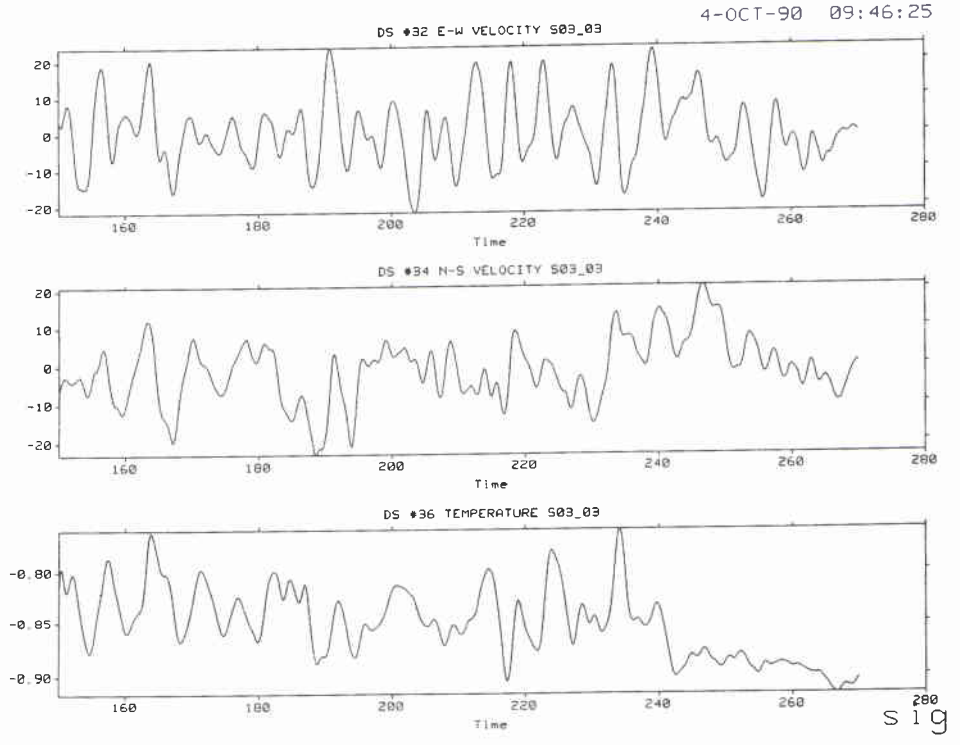

Figure A7b

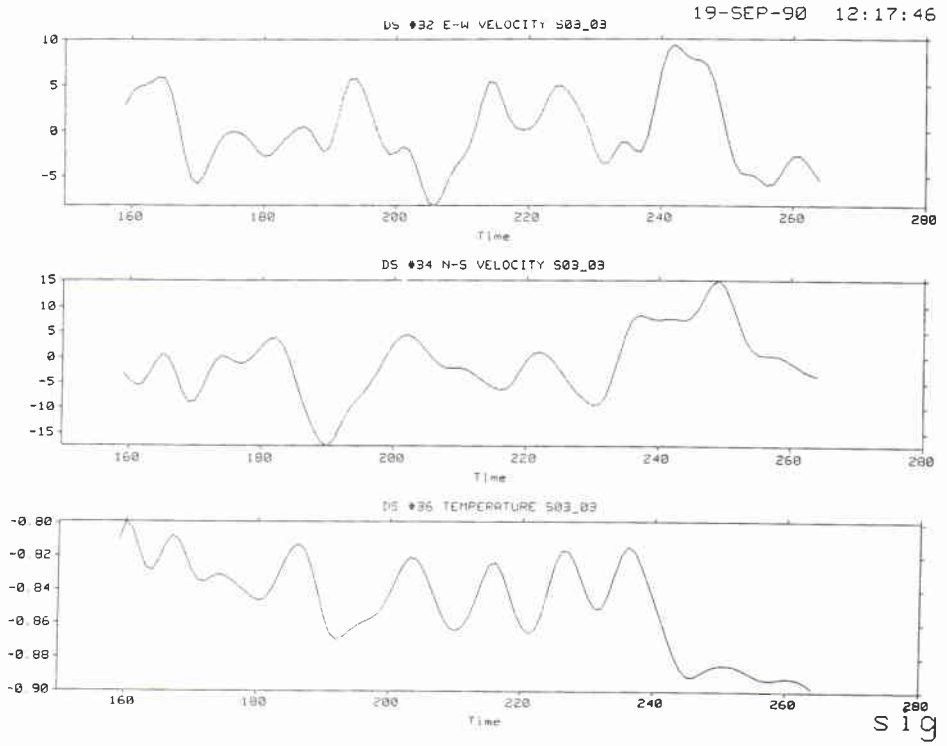

Figure A7c

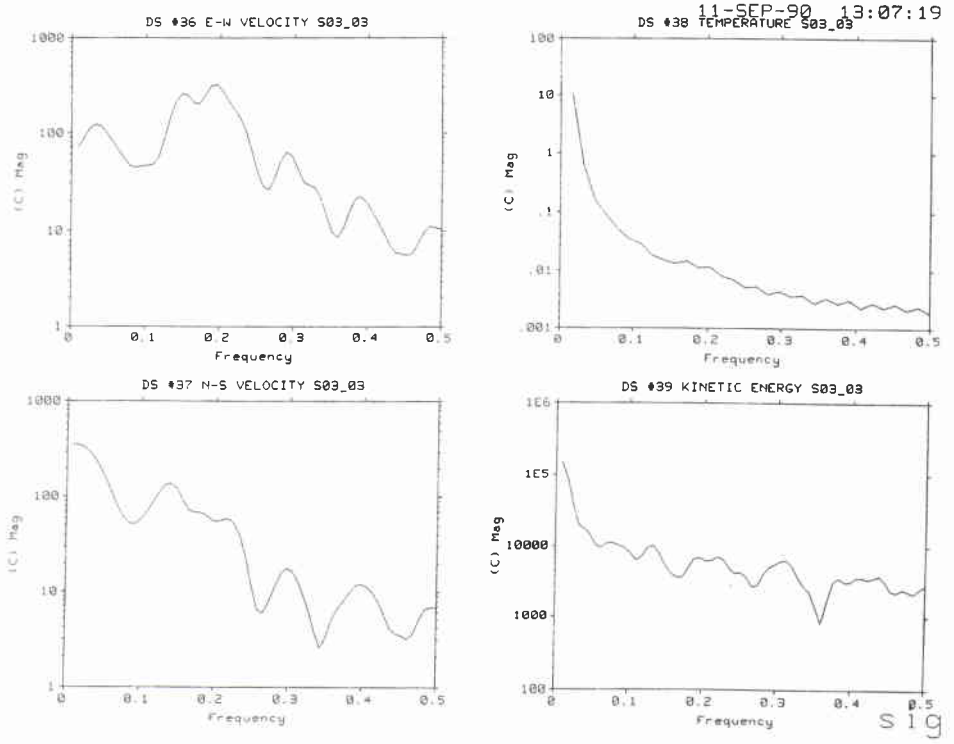

Figure A7d

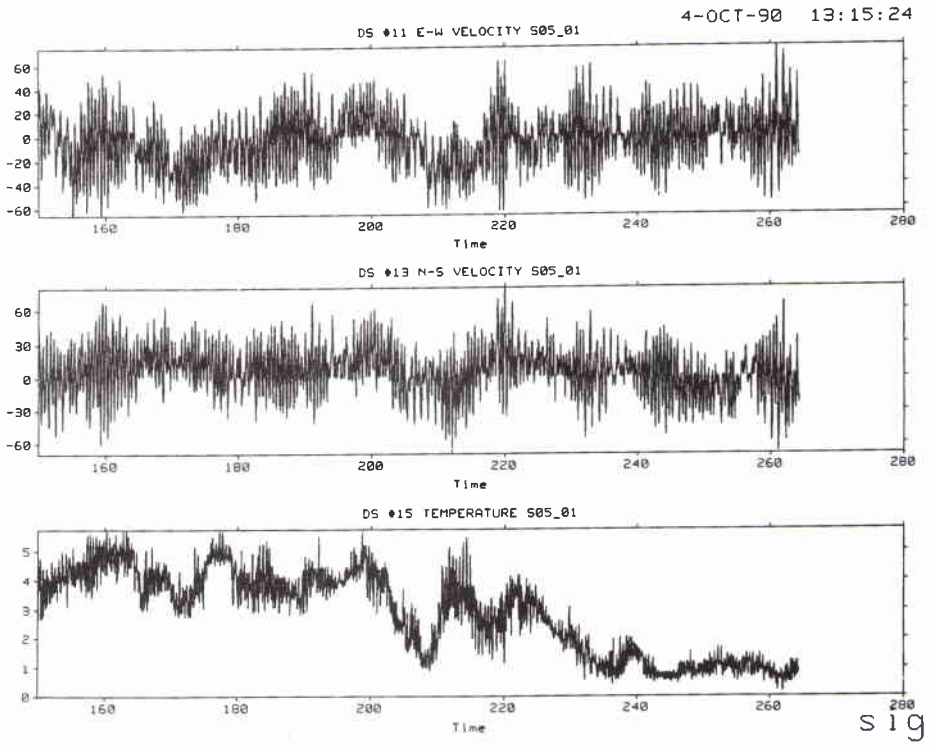

Figure A8a

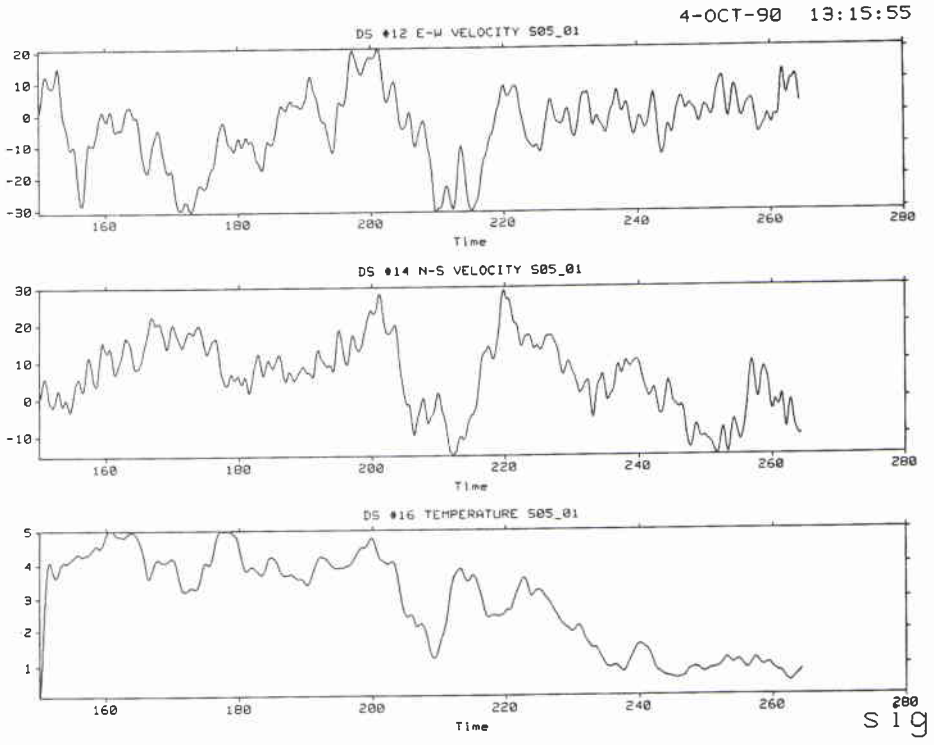

Figure A8b

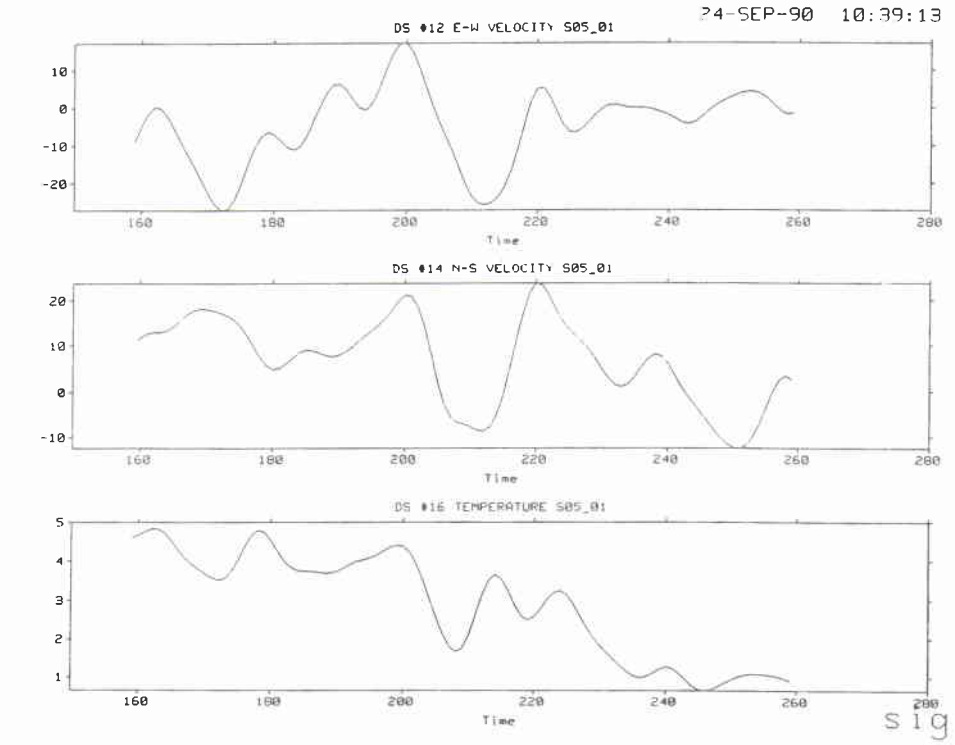

Figure A8c

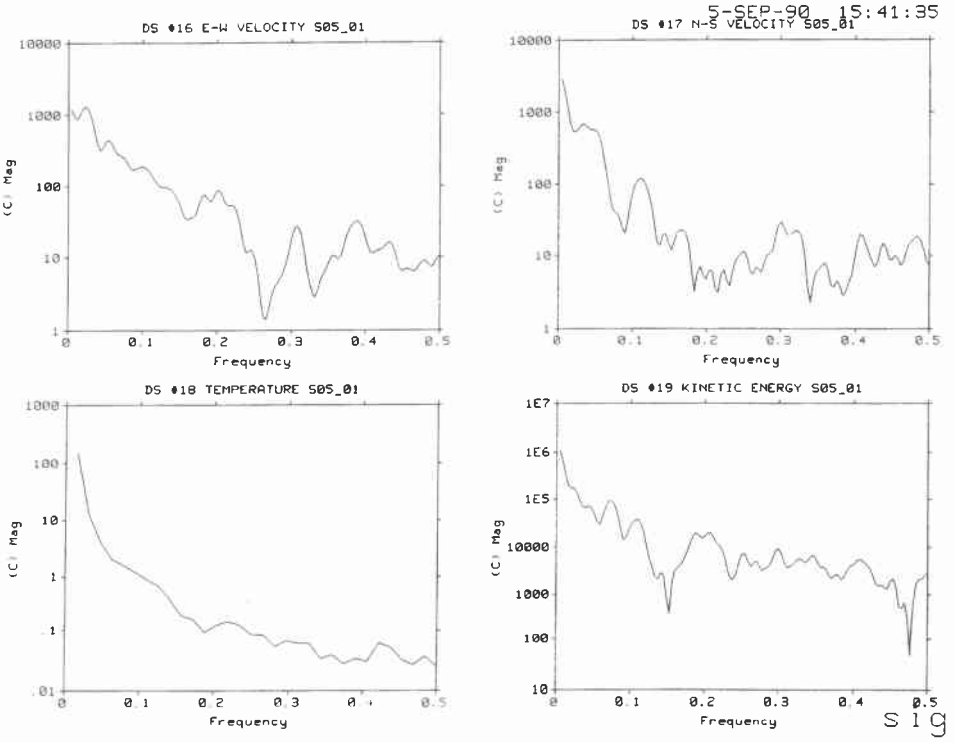

Figure A8d

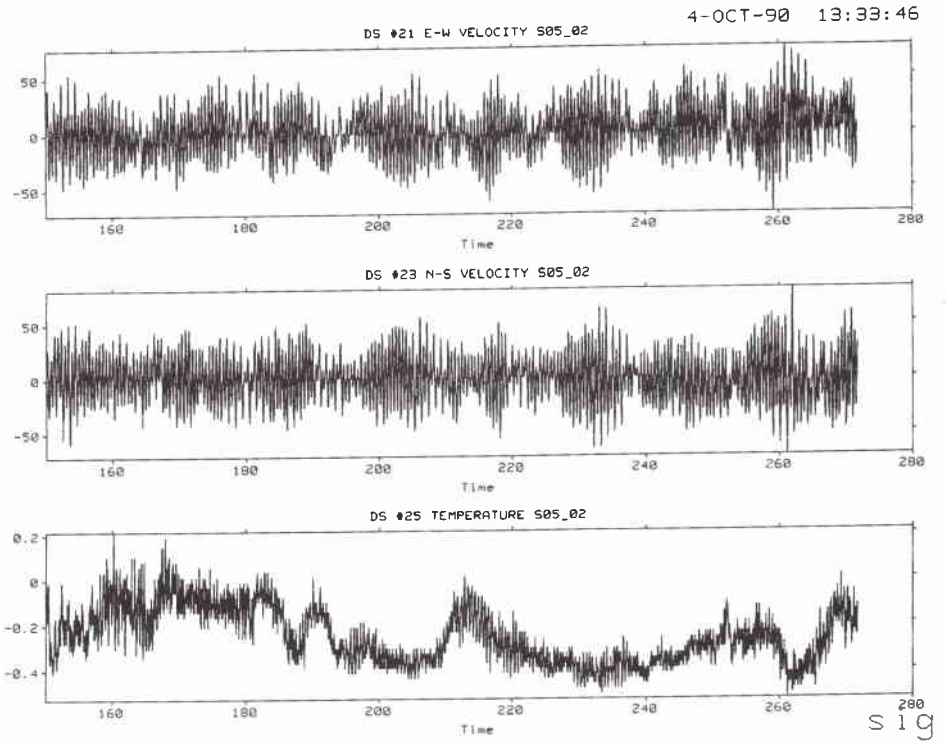

Figure A9a

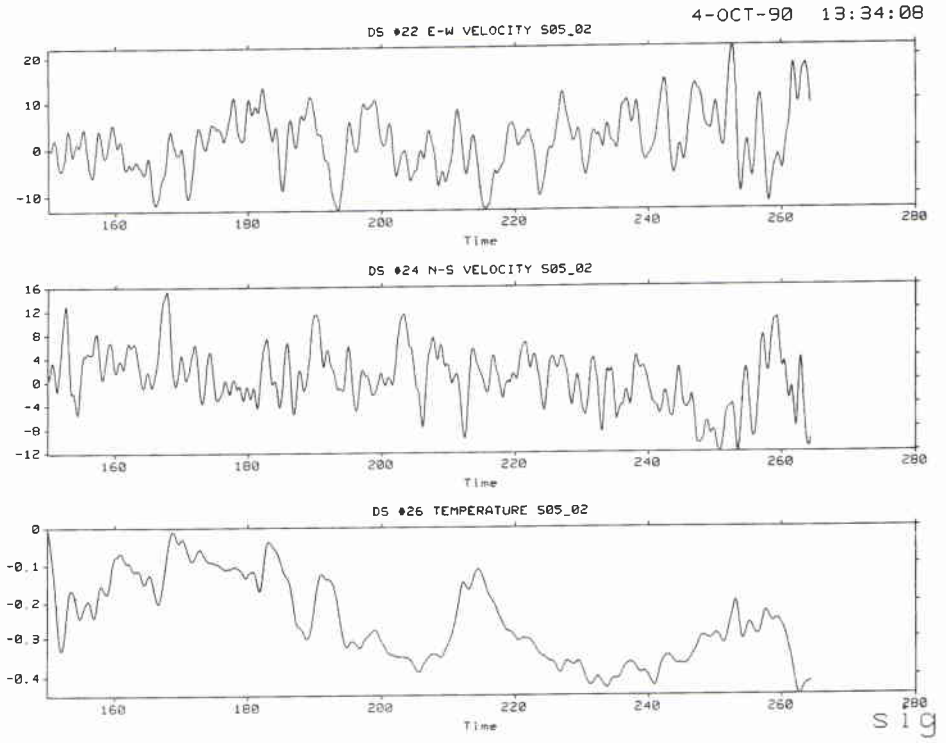

Figure A9b

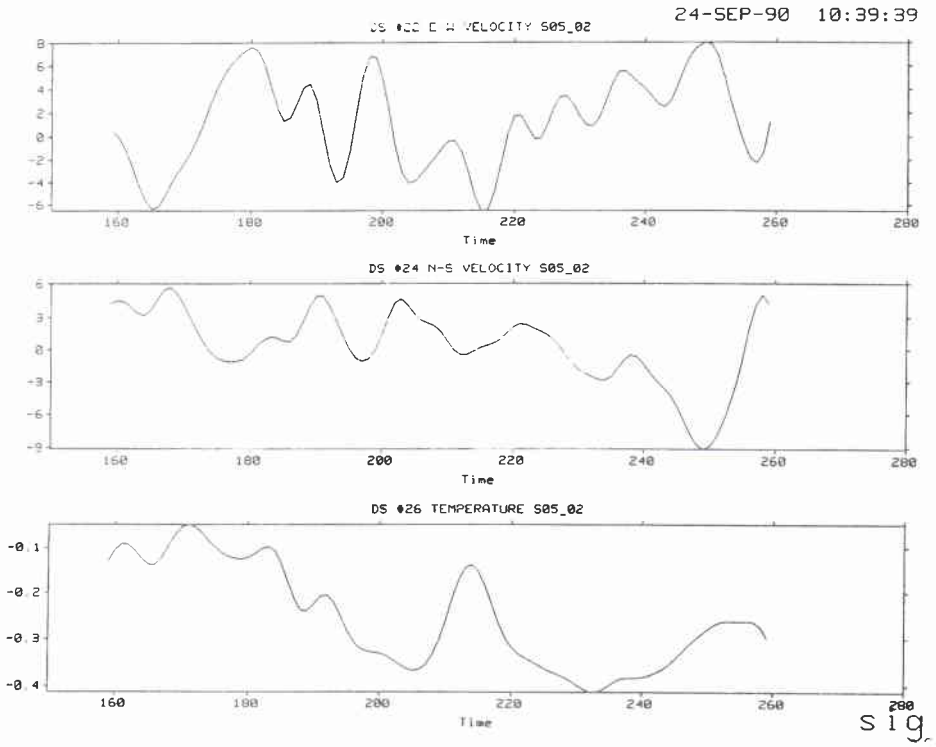

Figure A9c

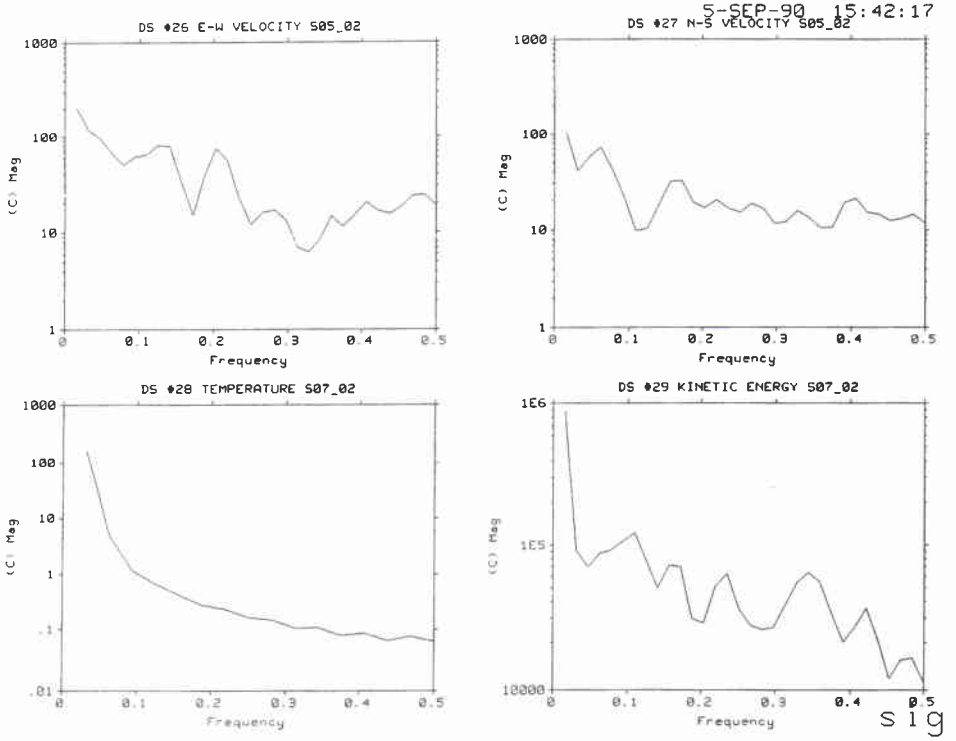

Figure A9d

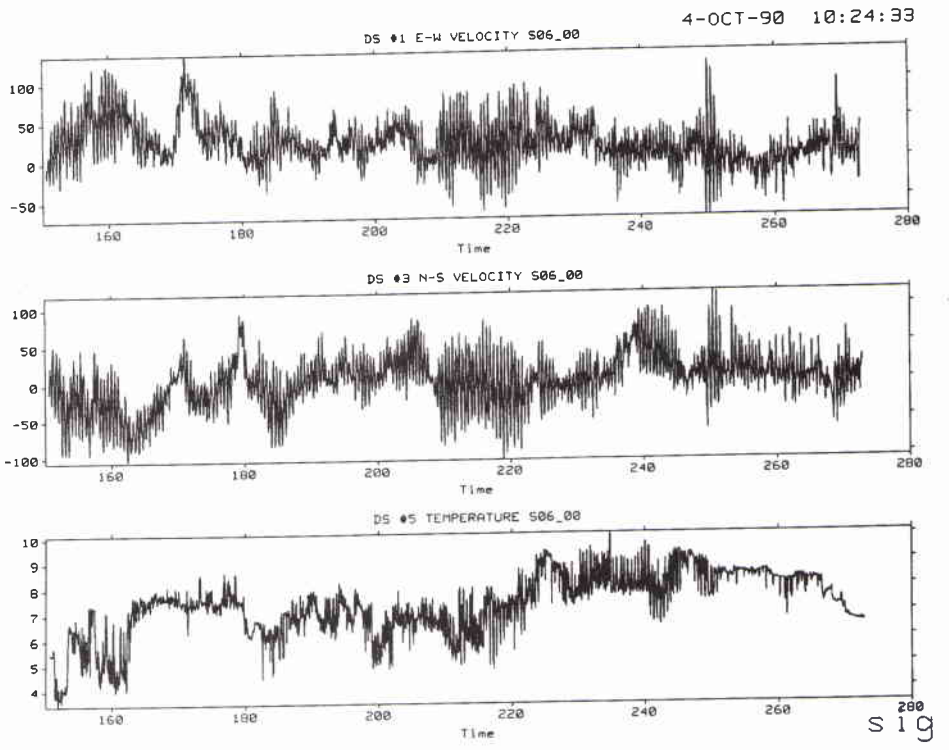

Figure A10a

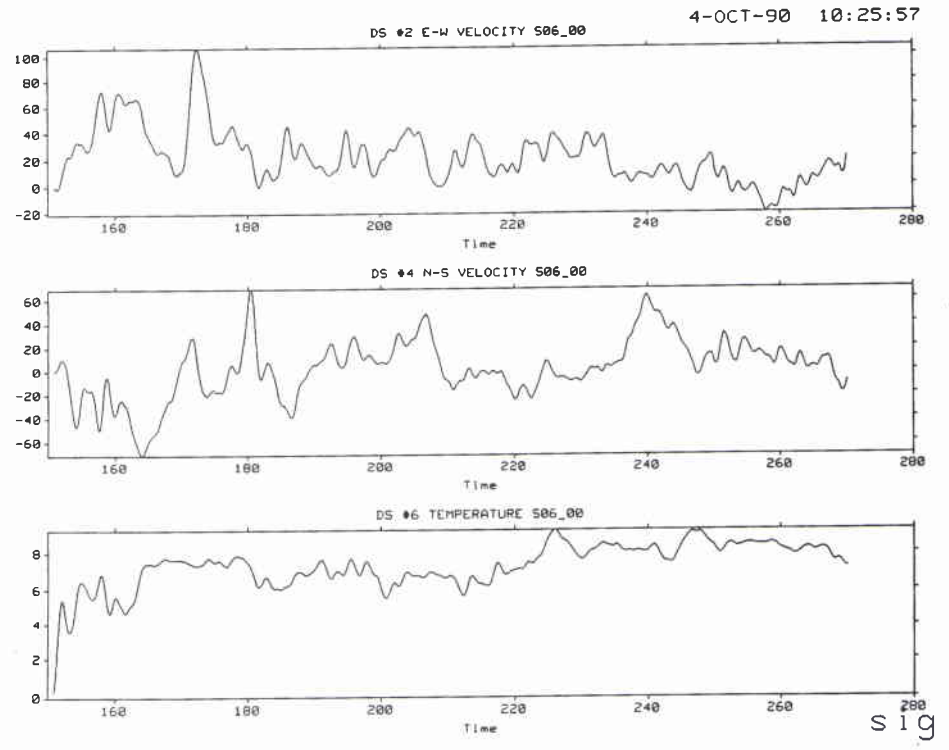

Figure A10b

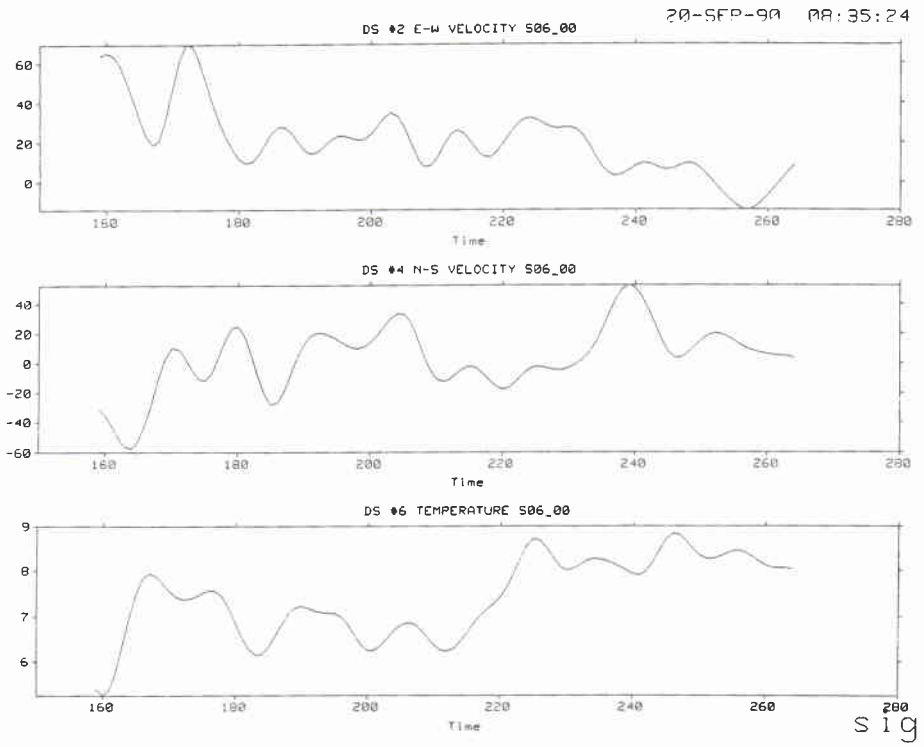

Figure A10c

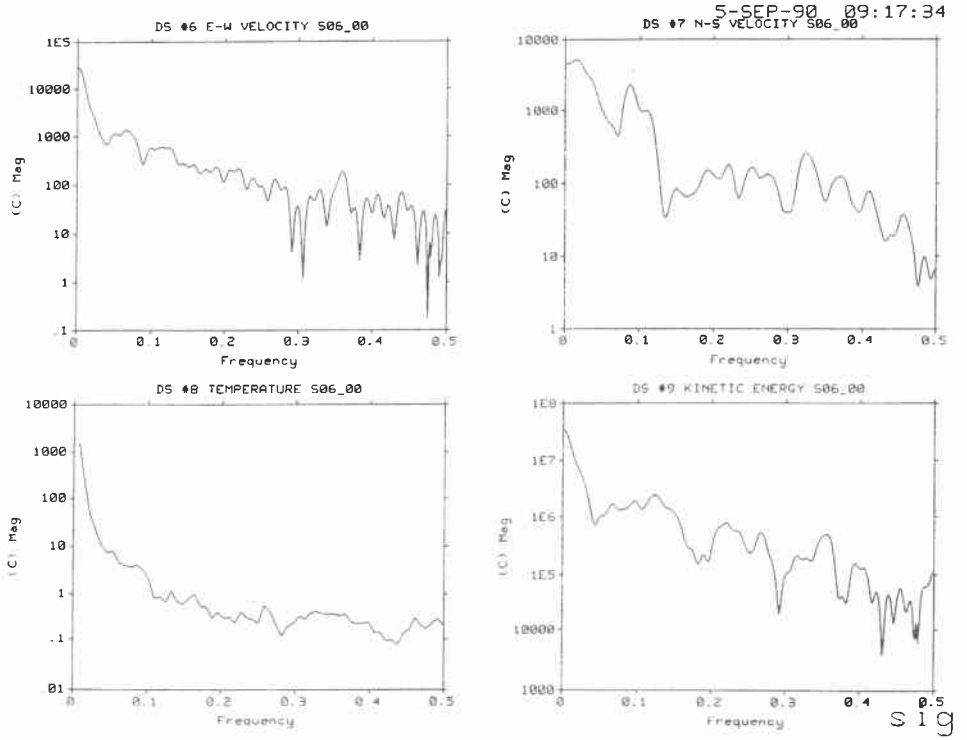

Figure A10d

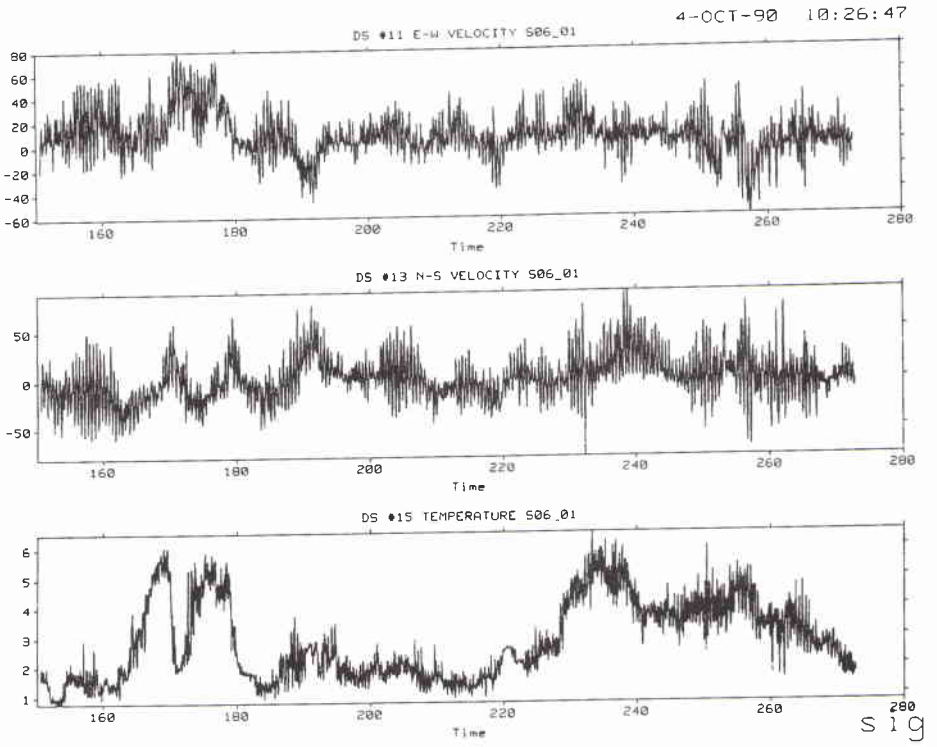

Figure A11a

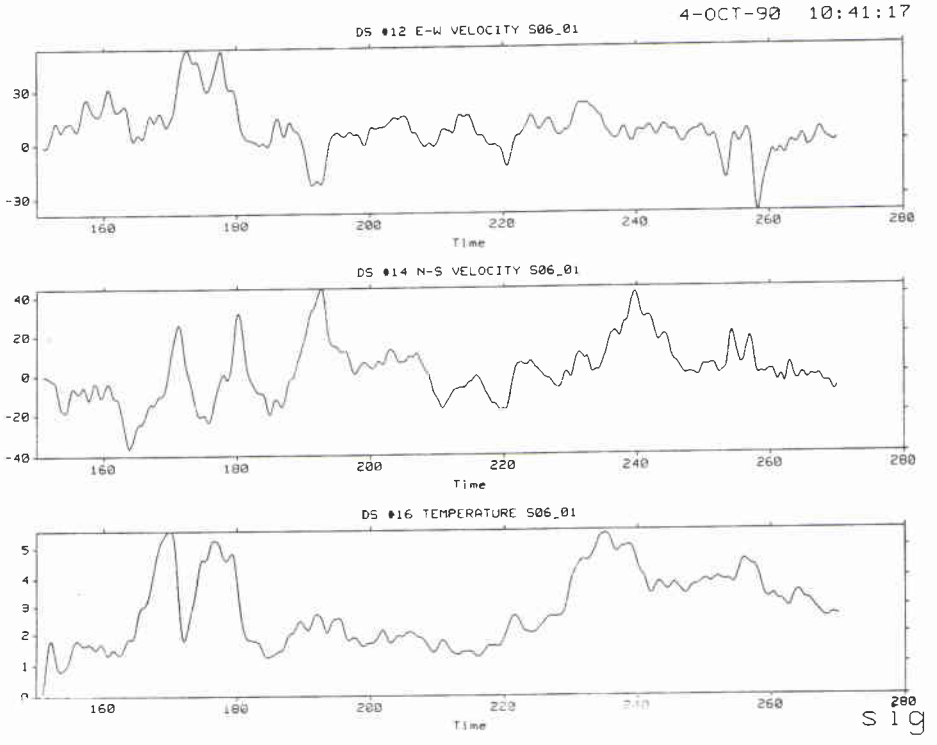

Figure A11b

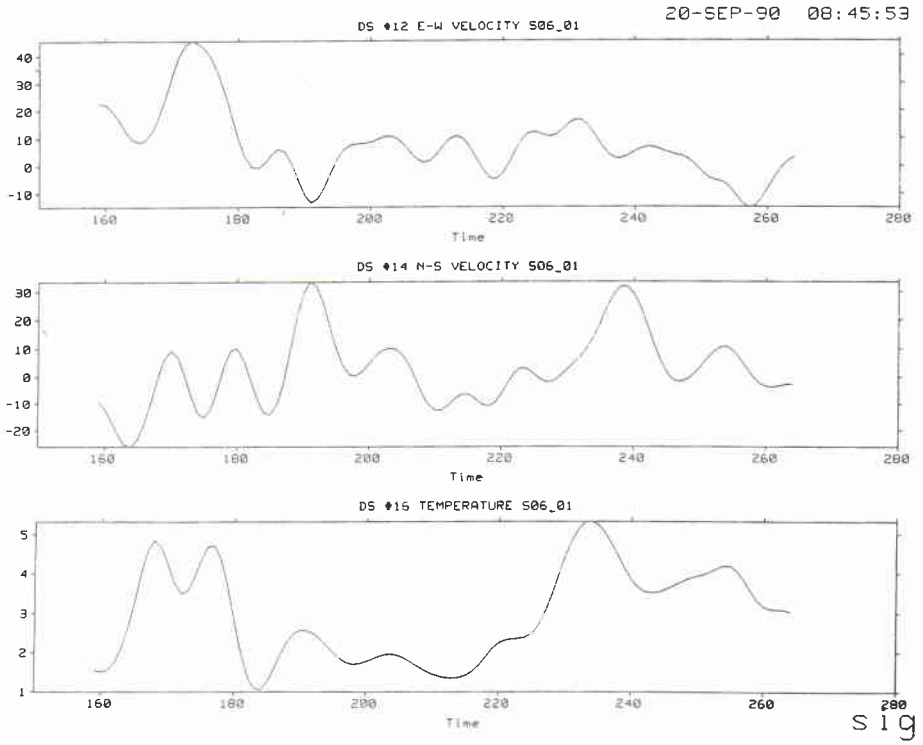

Figure A11c

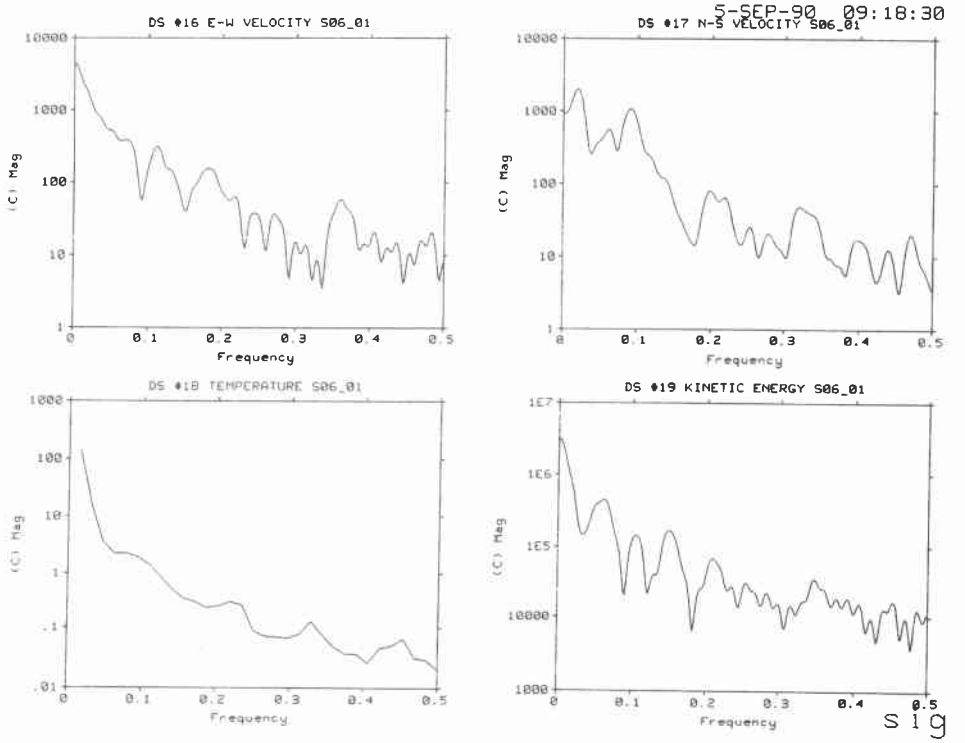

Figure A11d

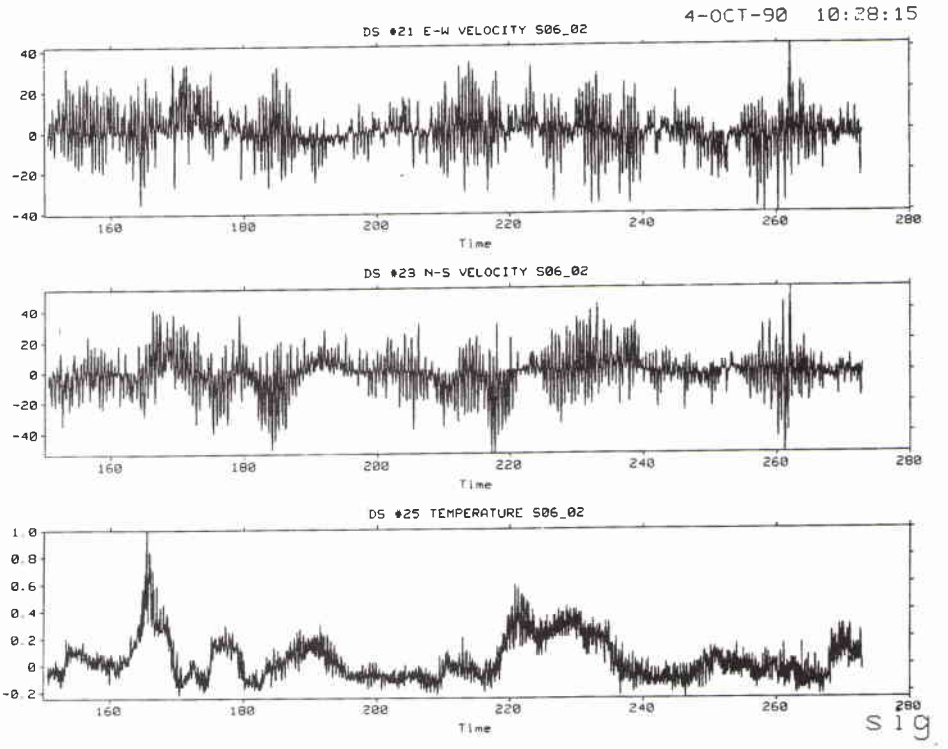

Figure A12a

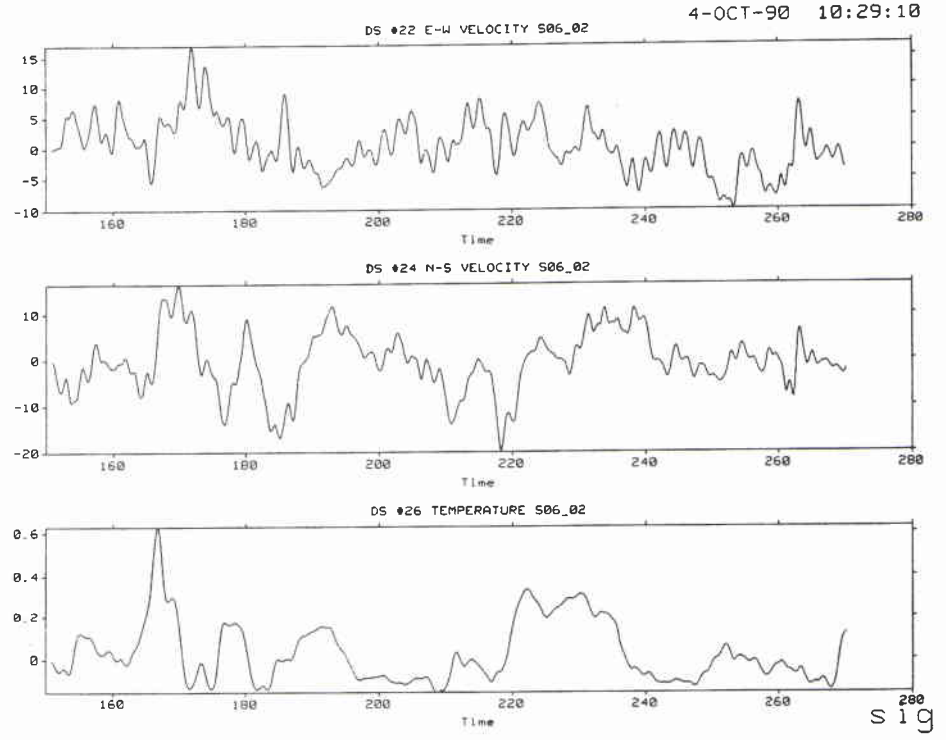

Figure A12b

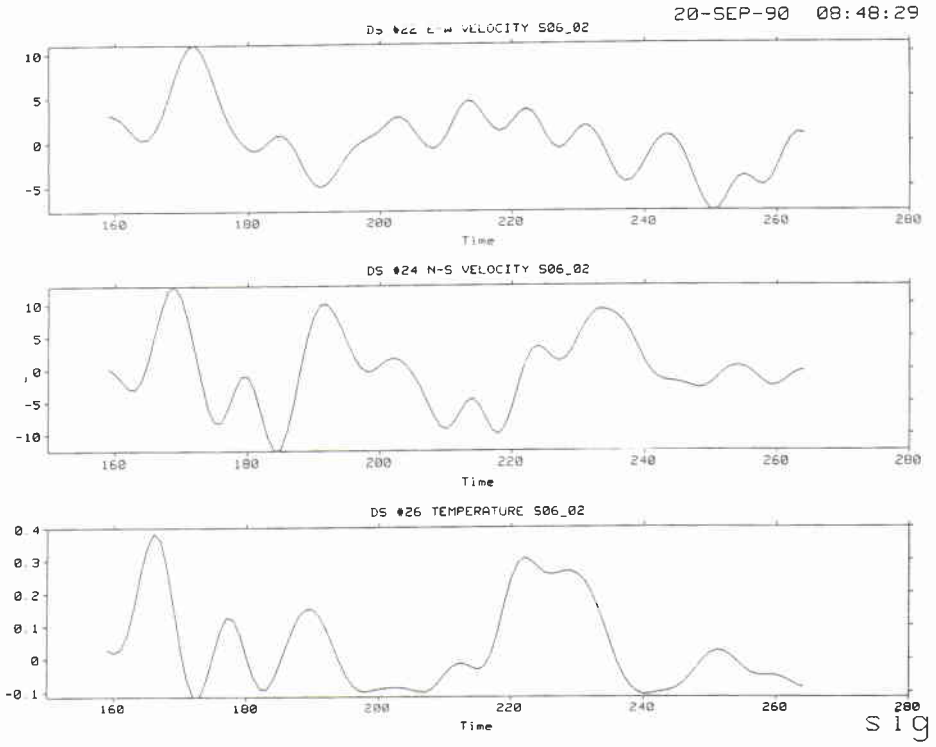

Figure A12c

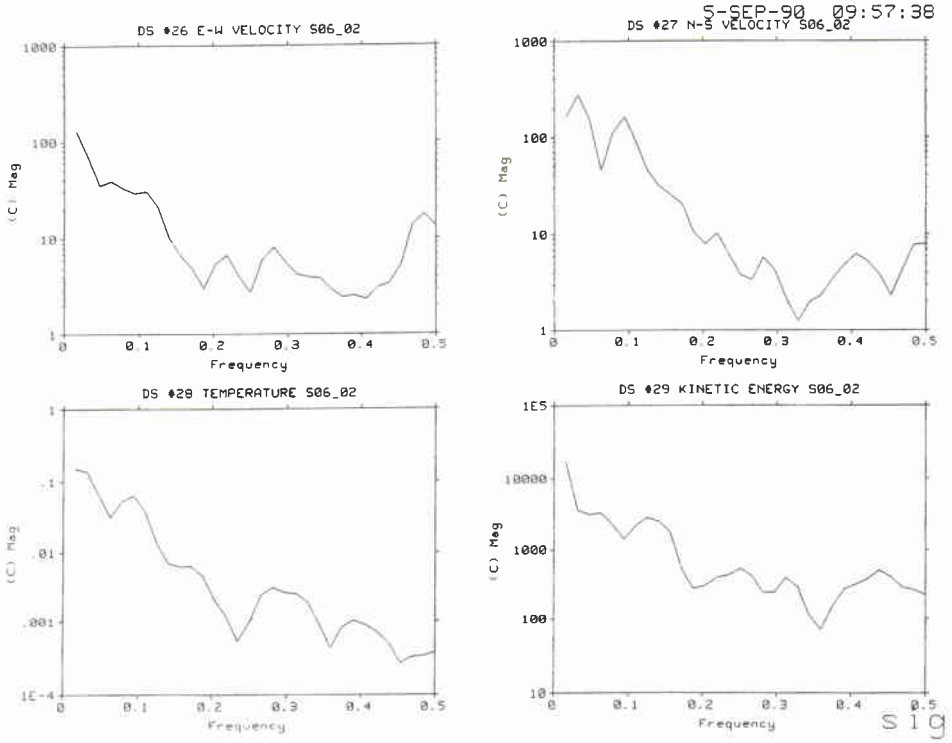

Figure A12d

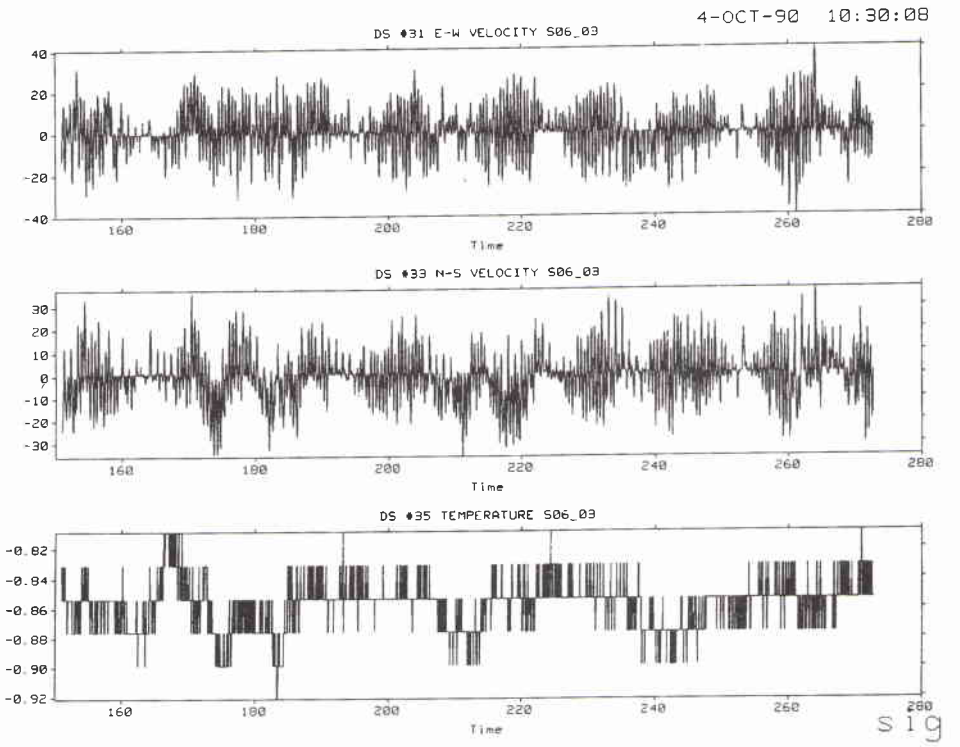

Figure A13a

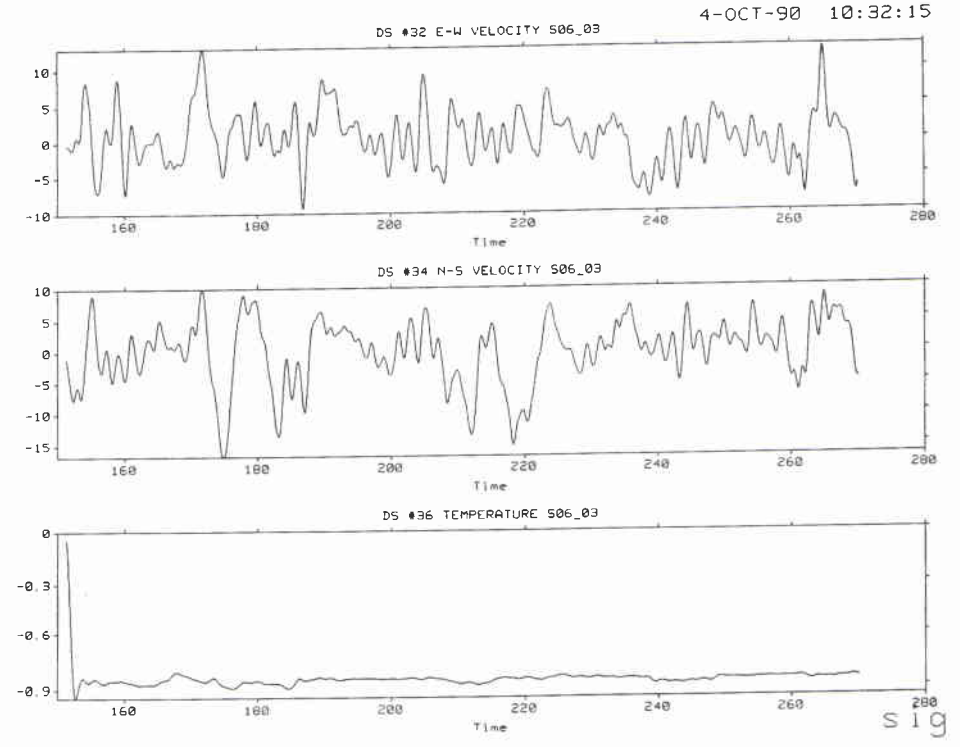

Figure A13b

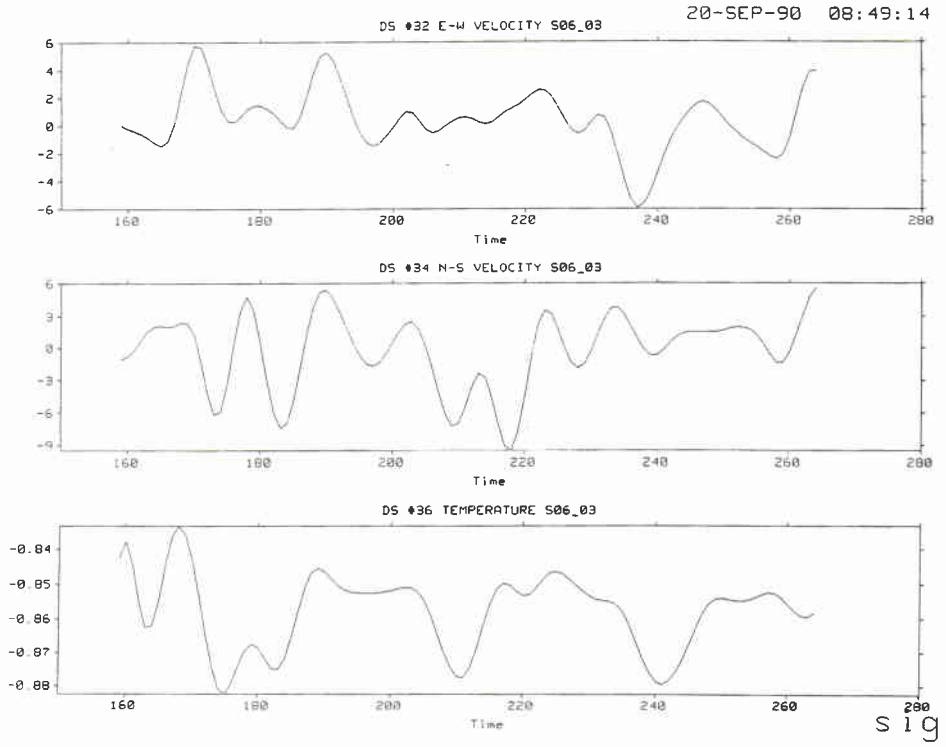

Figure A13c

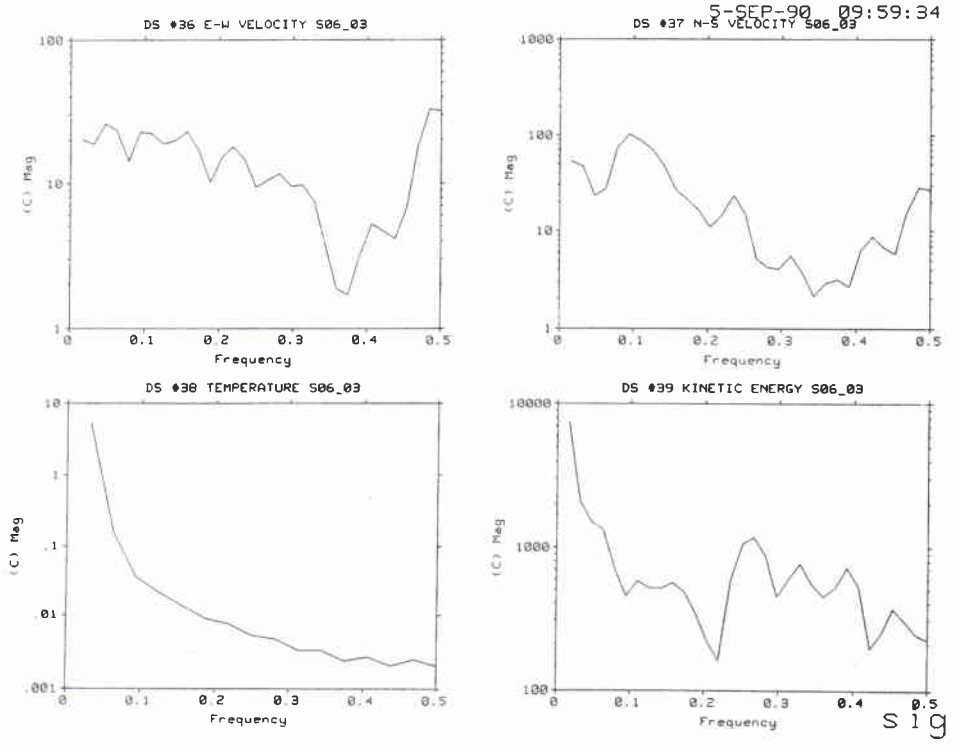

Figure A13d

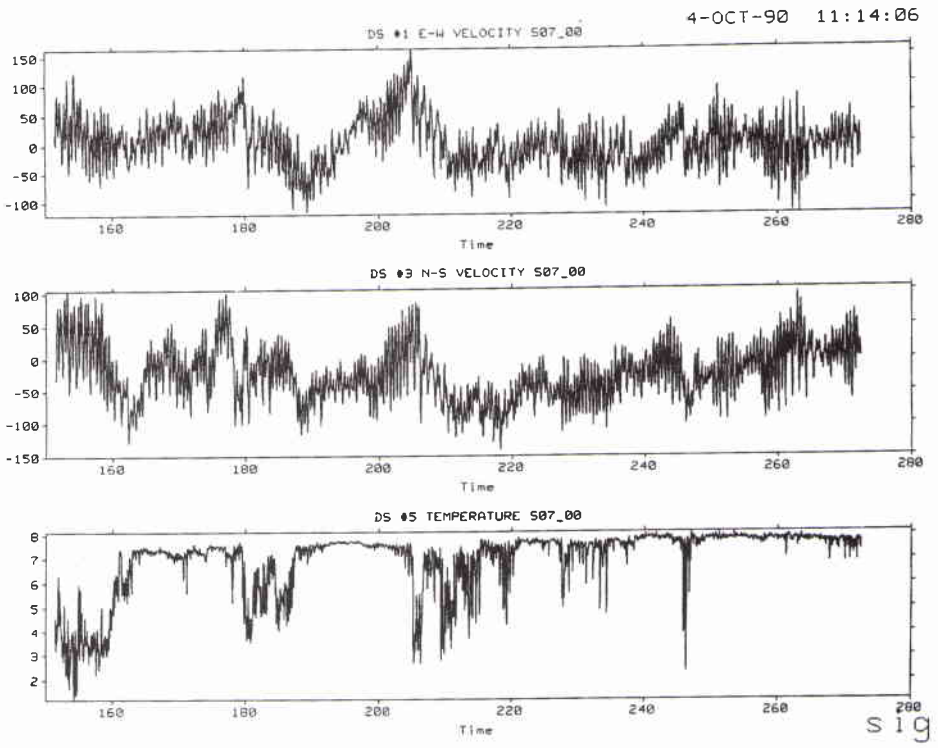

Figure A14a

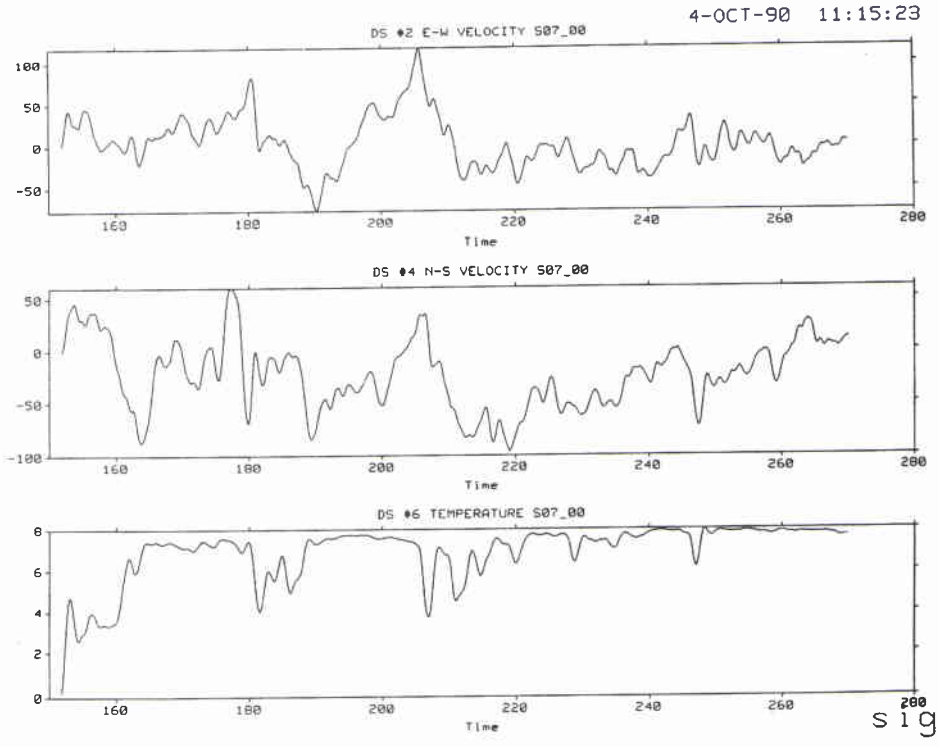

Figure A14b

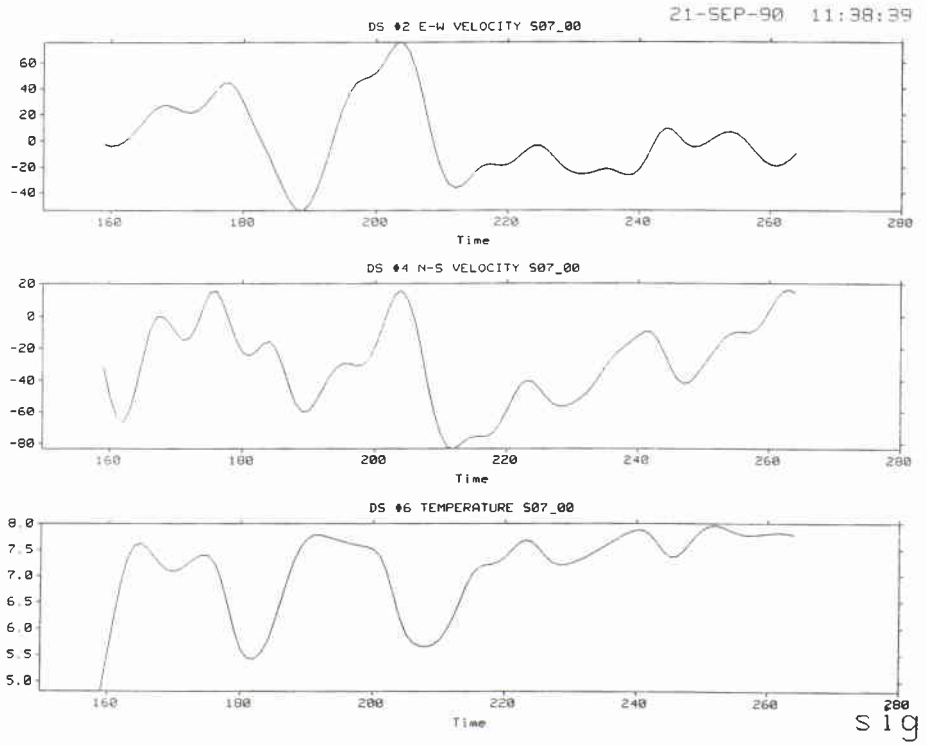

Figure A14c

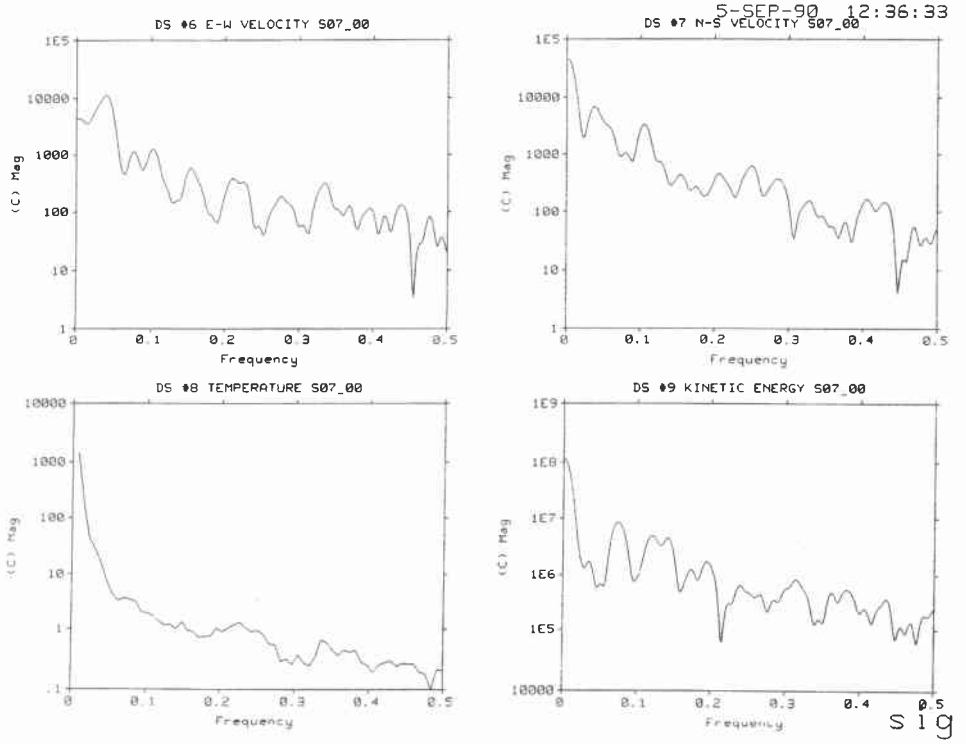

Figure A14d

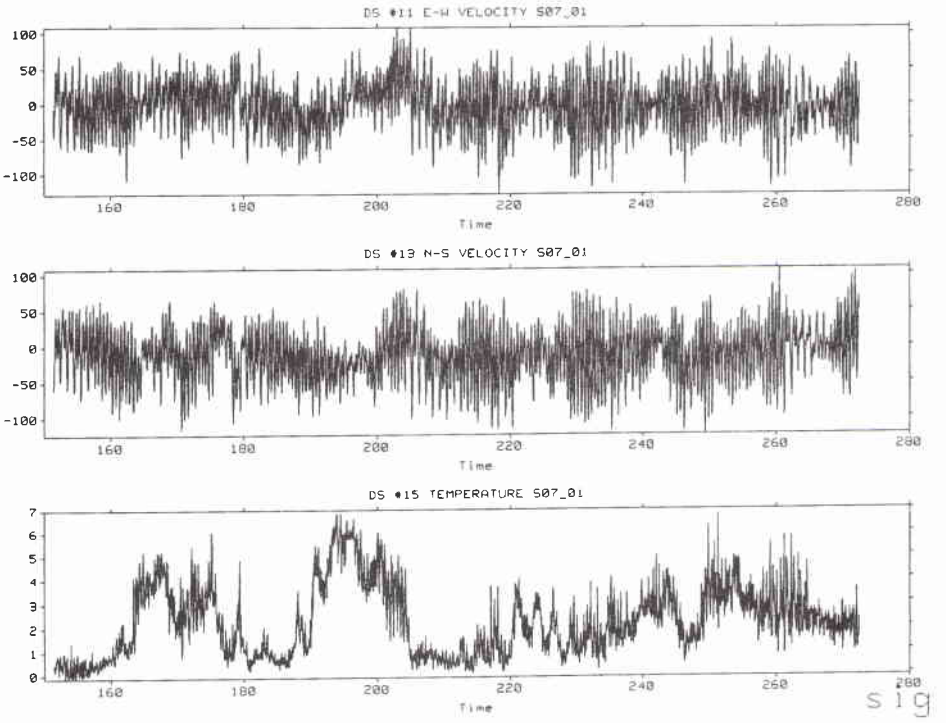

Figure A15a

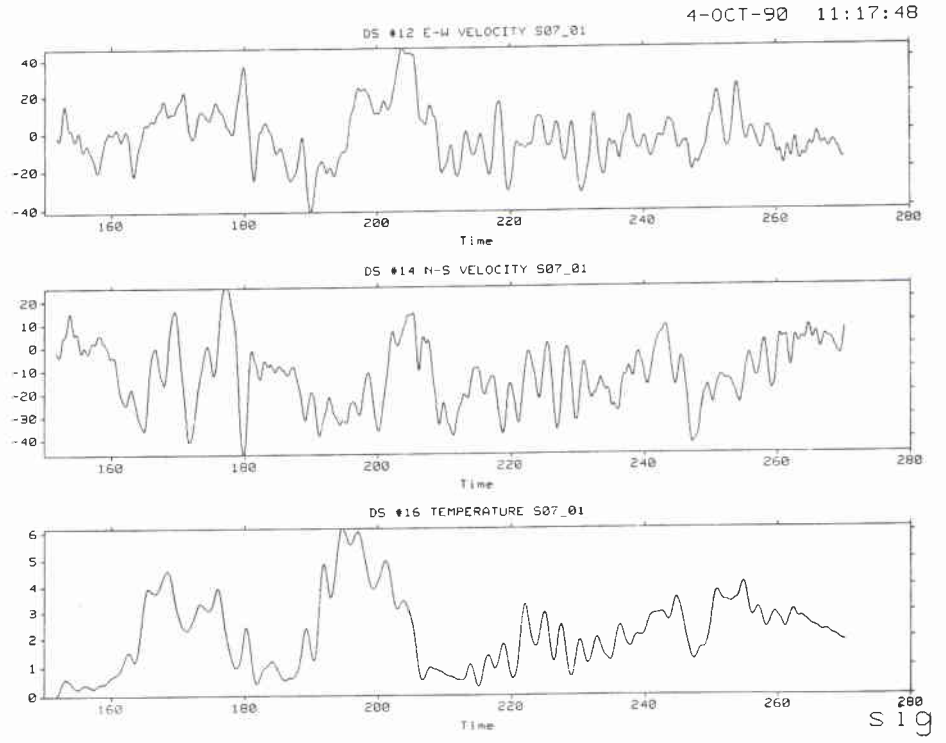

Figure A15b

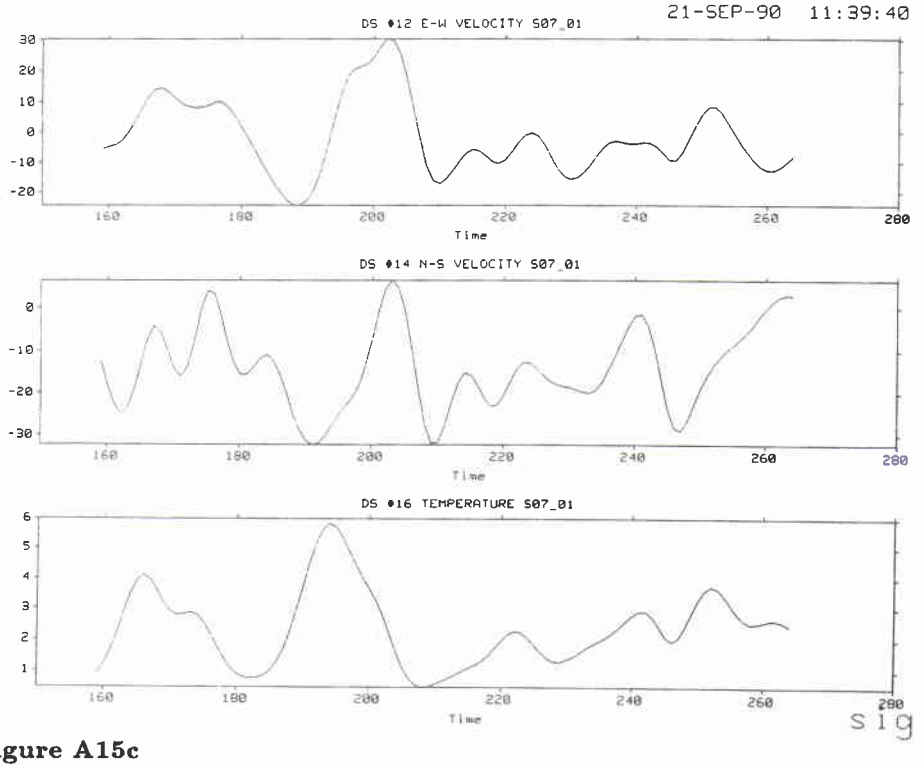

Figure A15c

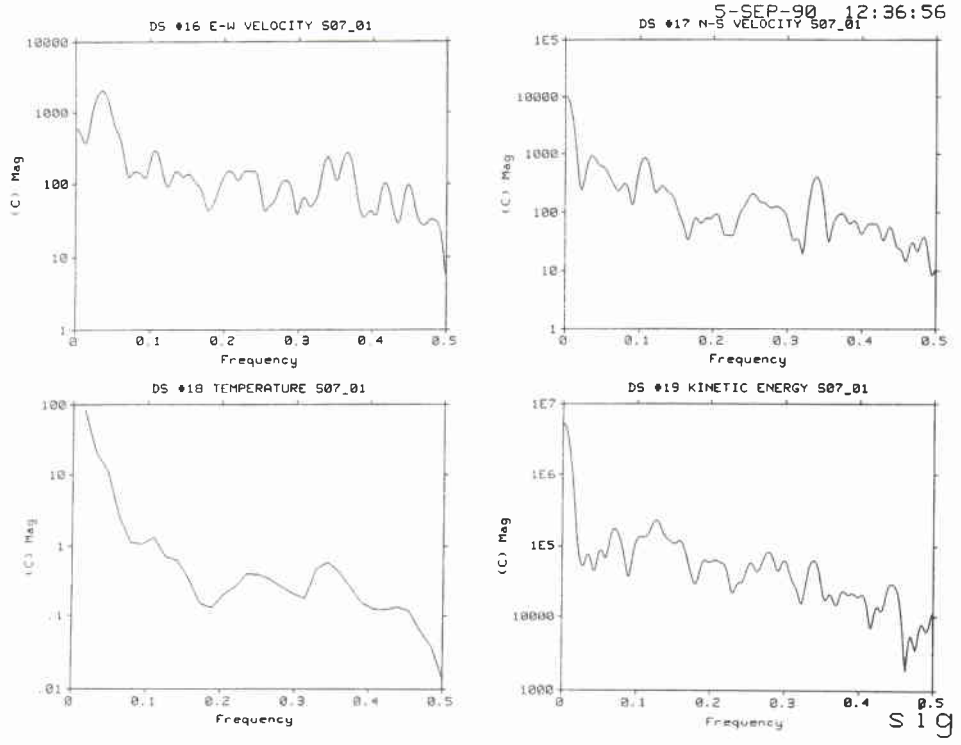

Figure A15d

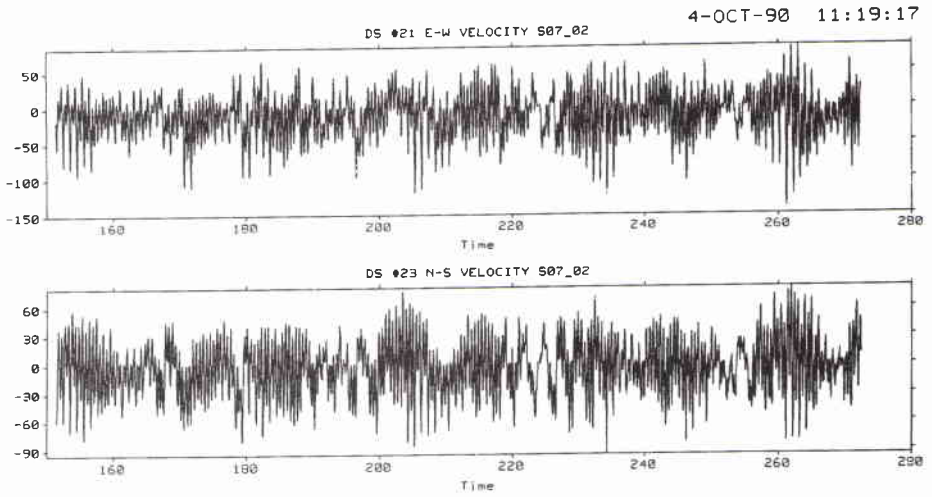

Figure A16a

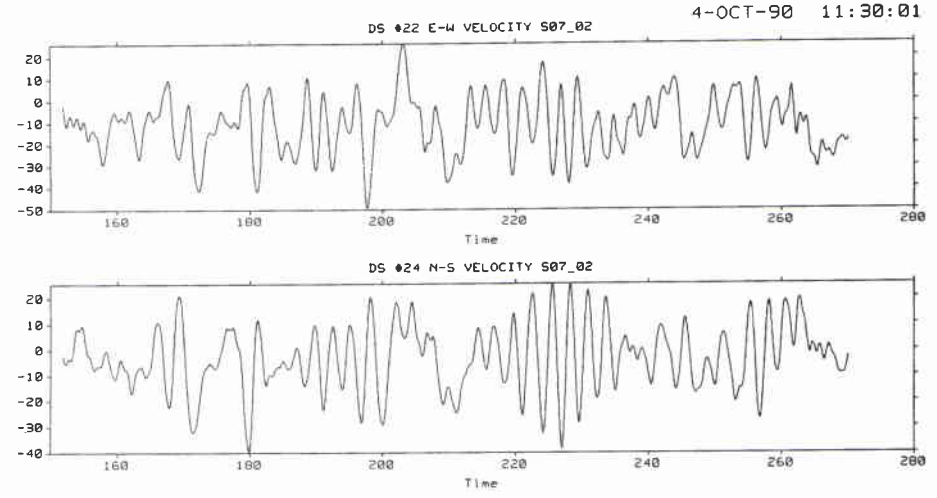

Figure A16b

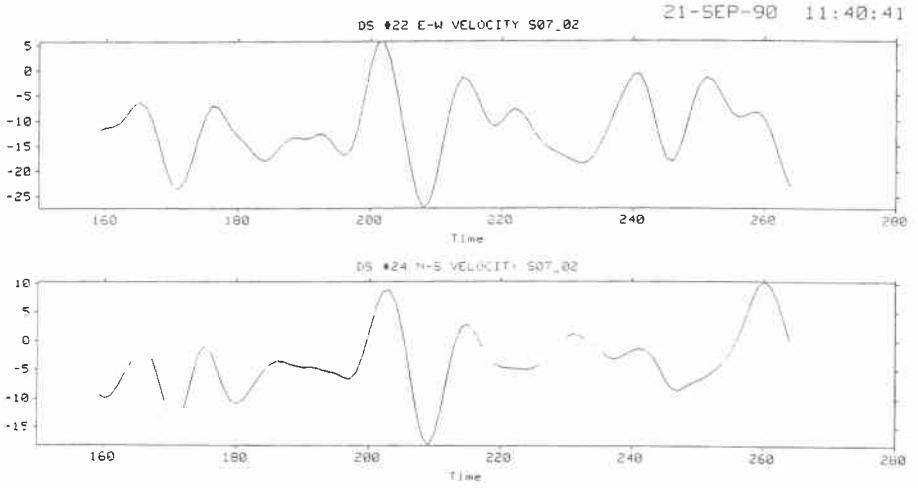

Figure A16c

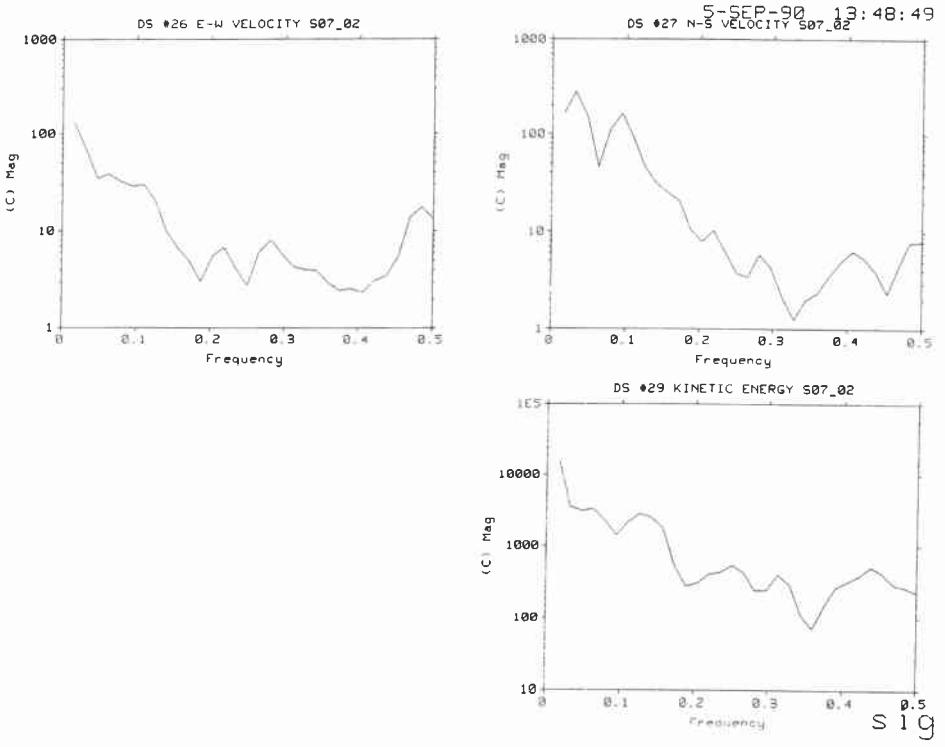

Figure A16d

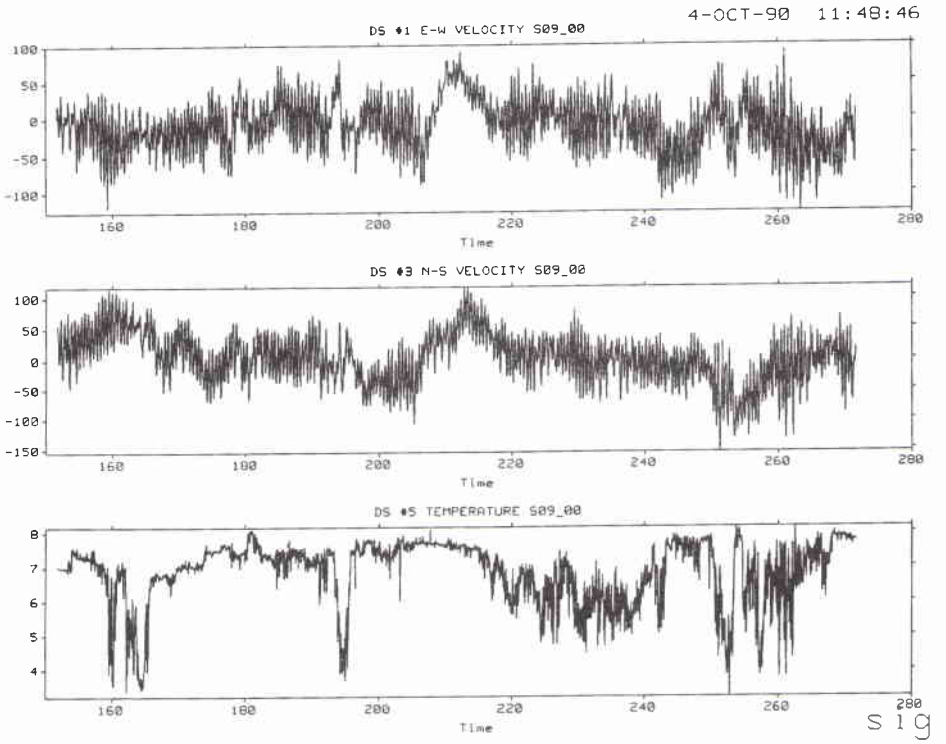

Figure A17a

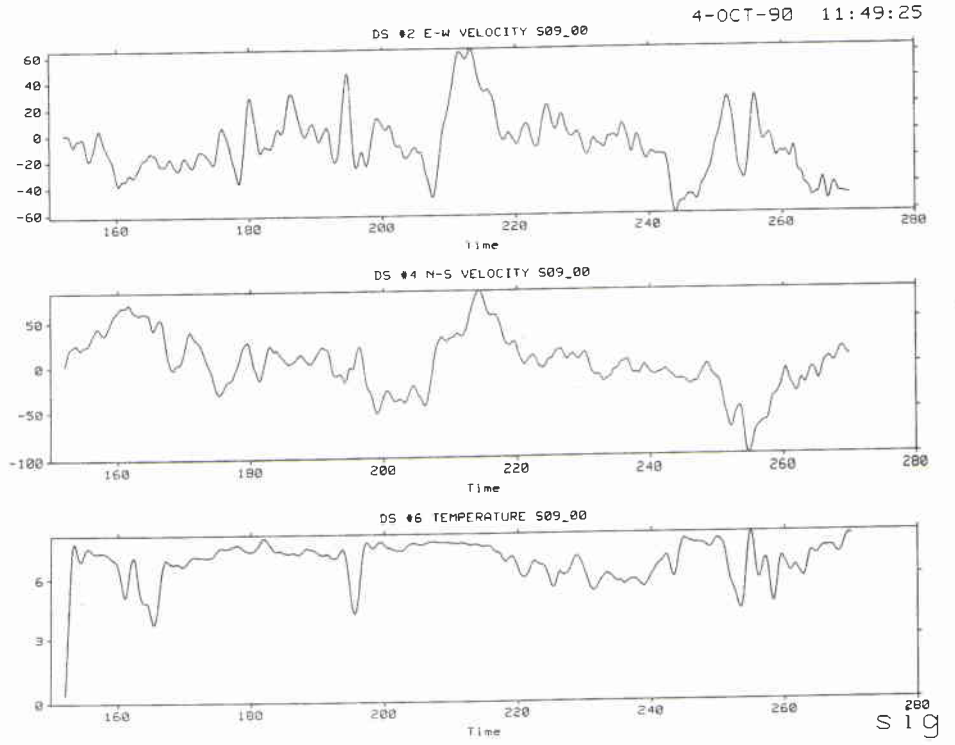

Figure A17b

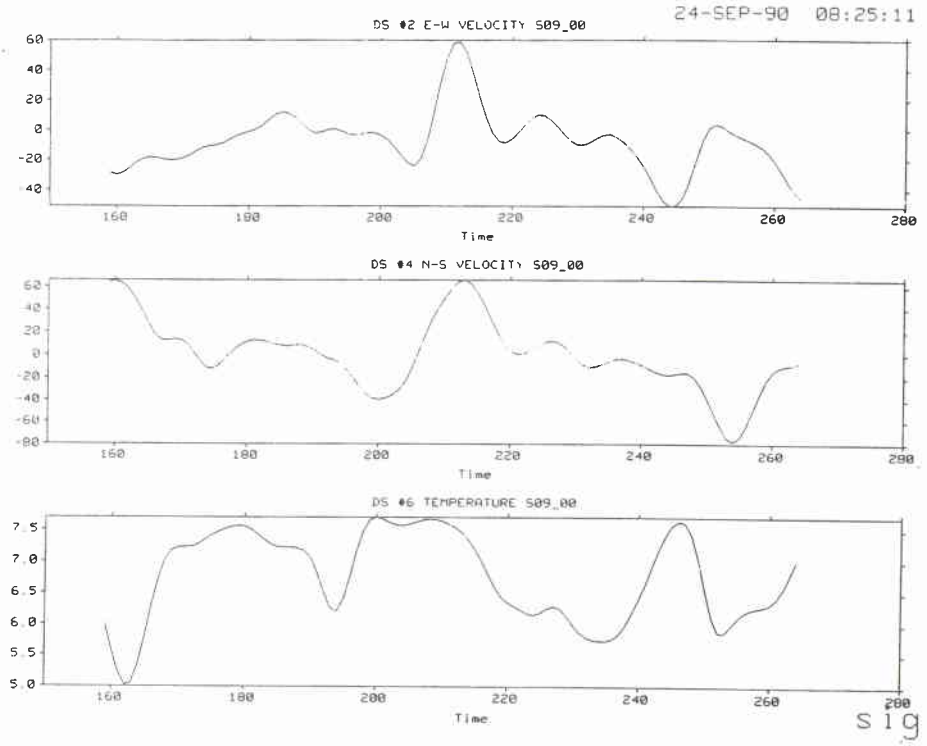

Figure A17c

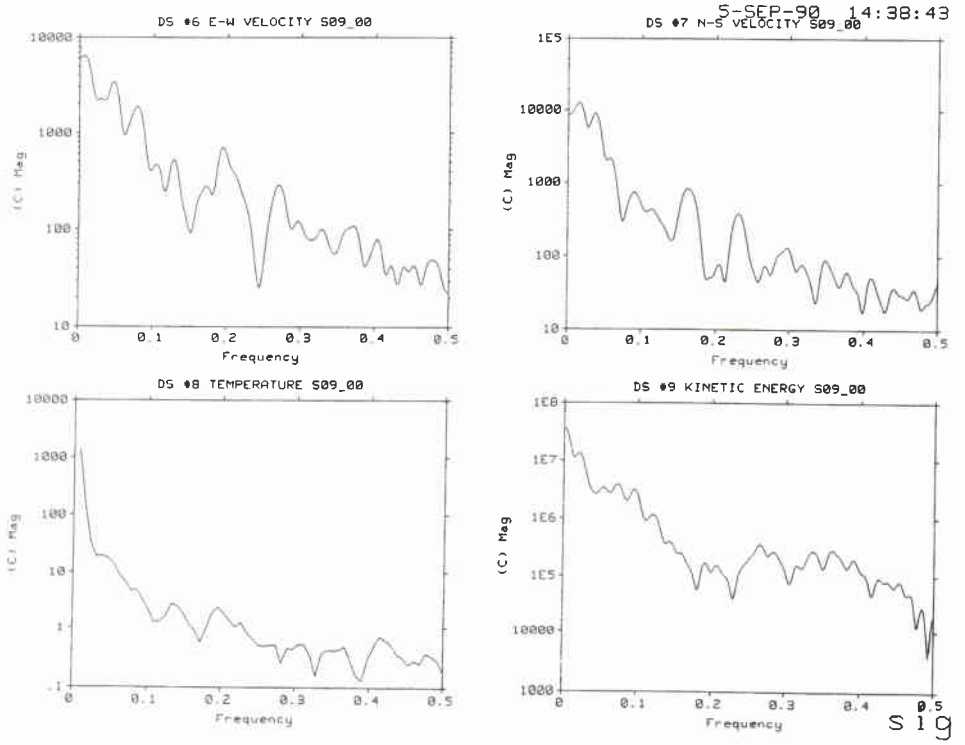

Figure A17d

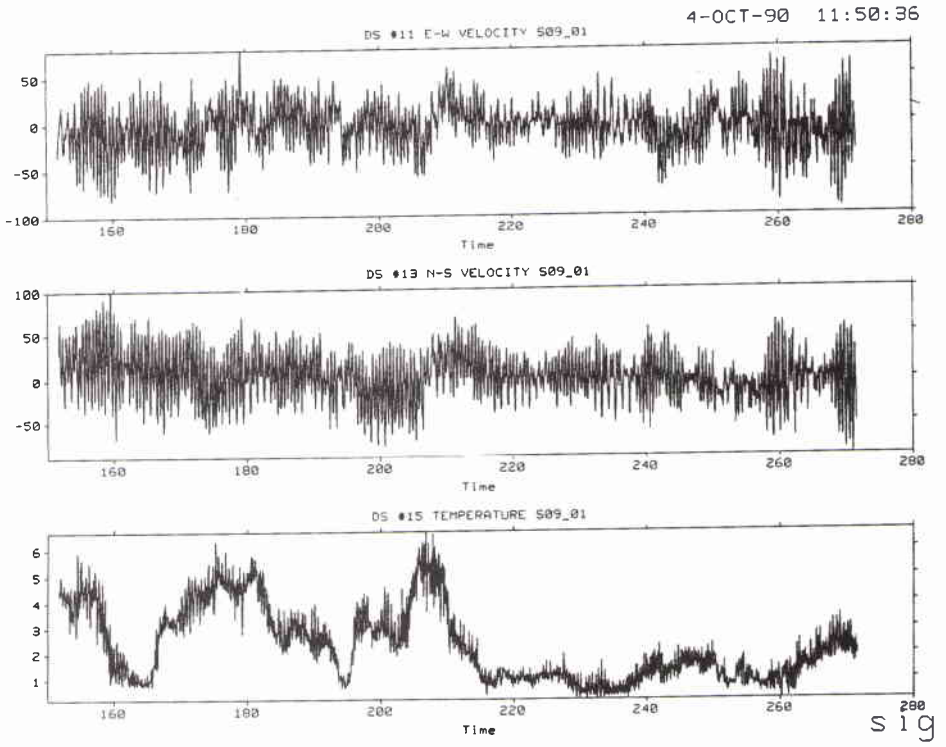

Figure A18a

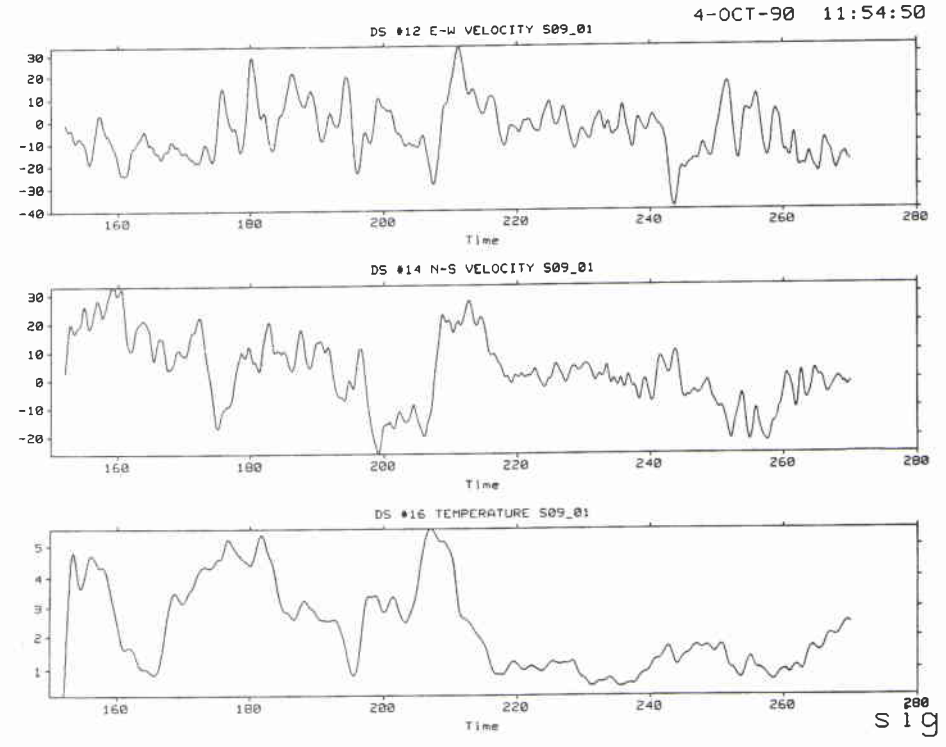

Figure A18b

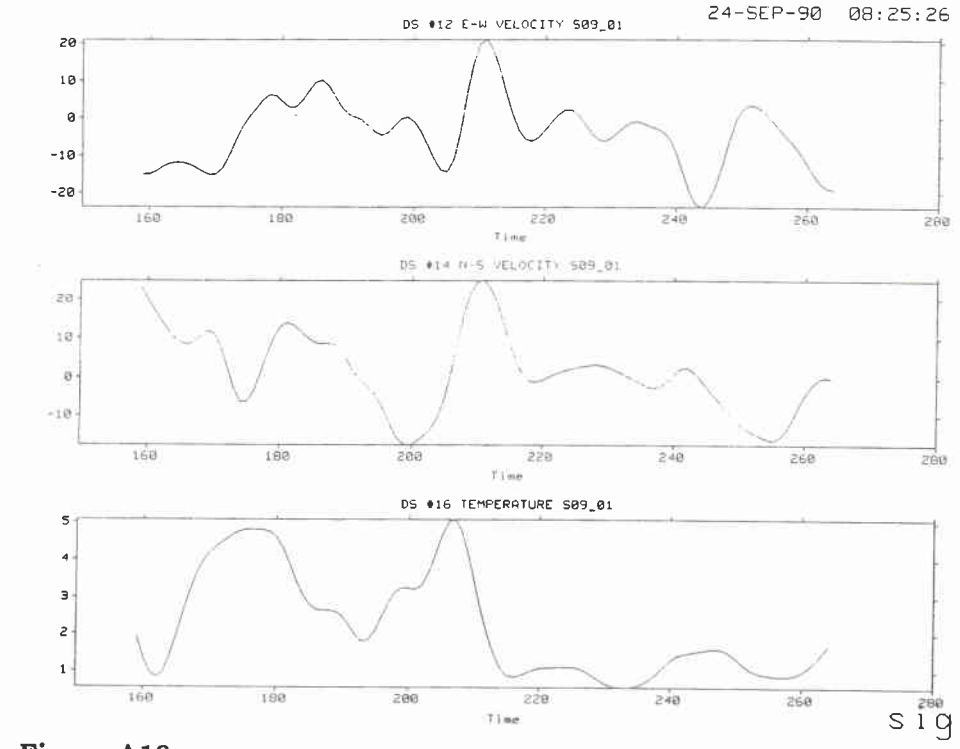

Figure A18c

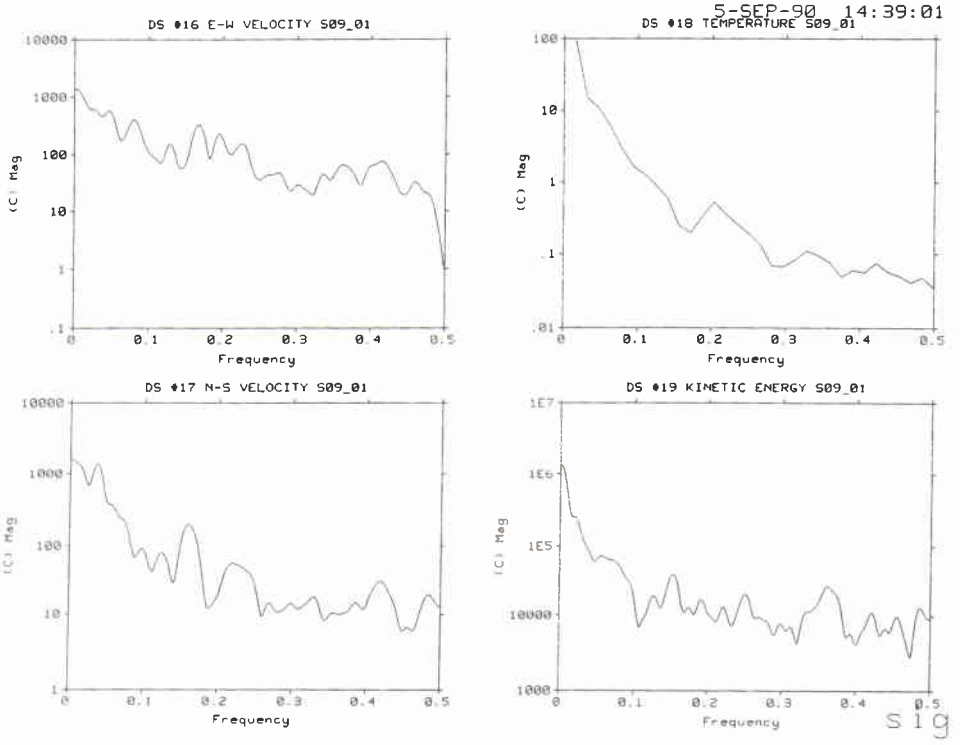

Figure A18d

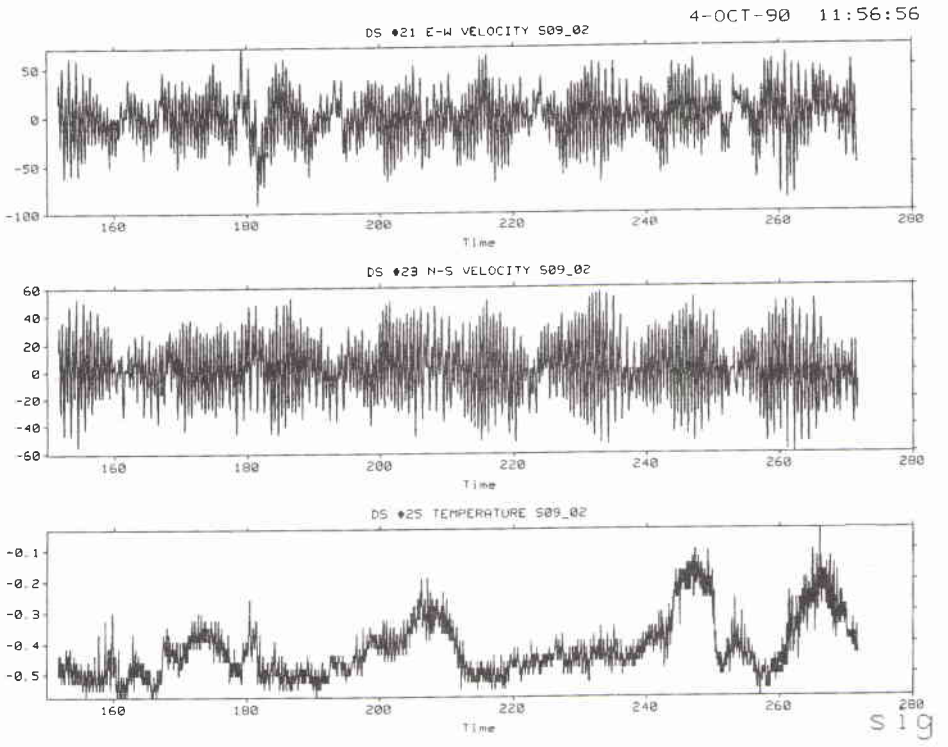

Figure A19a

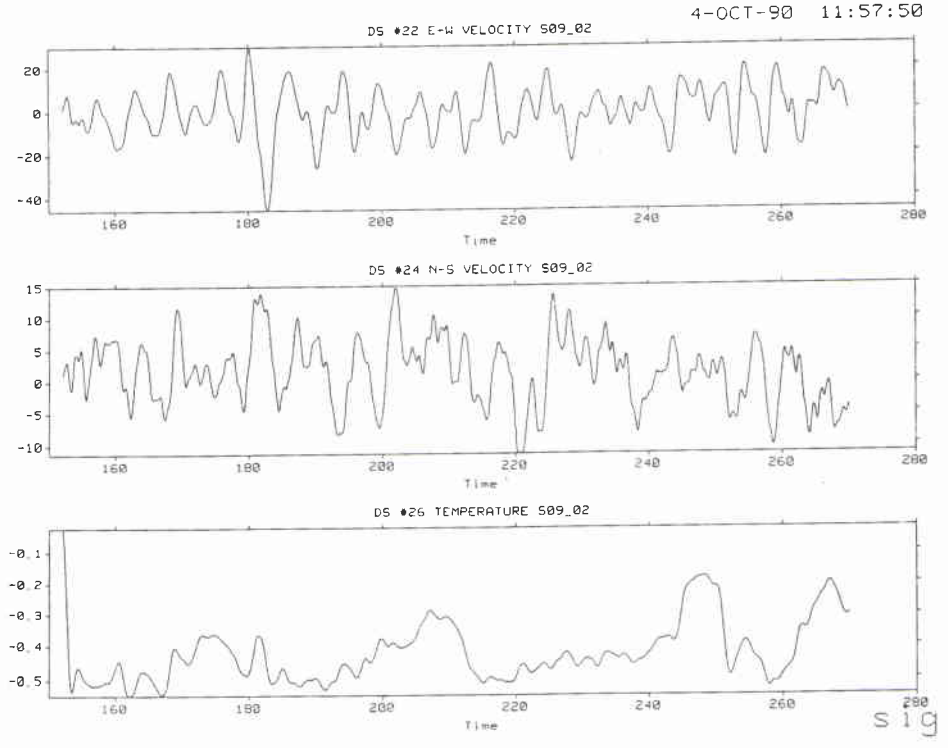

Figure A19b

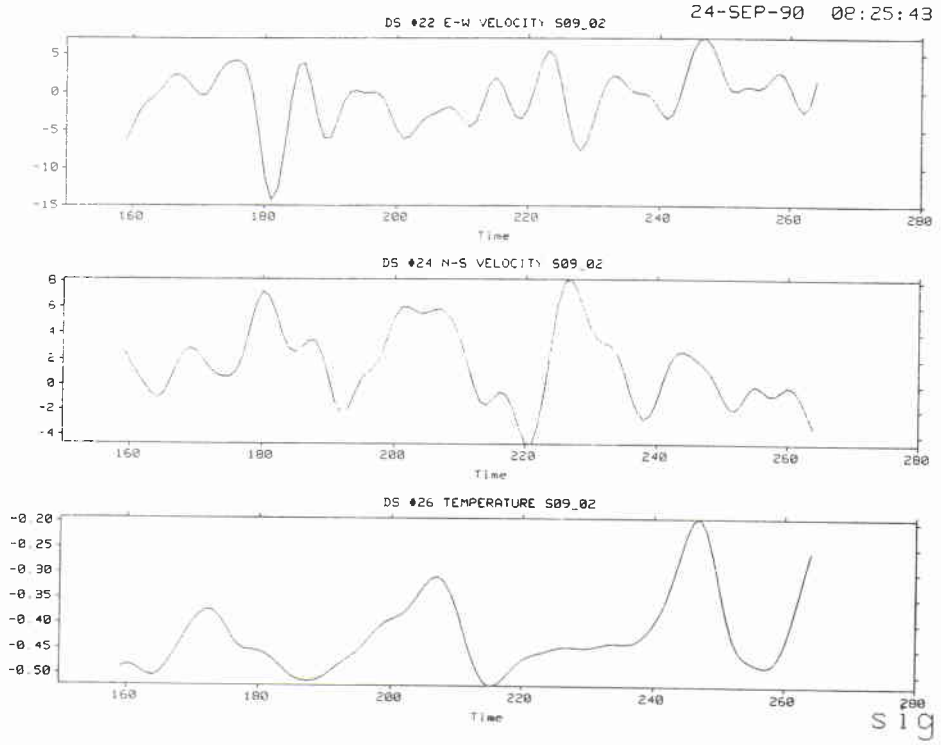

Figure A19c

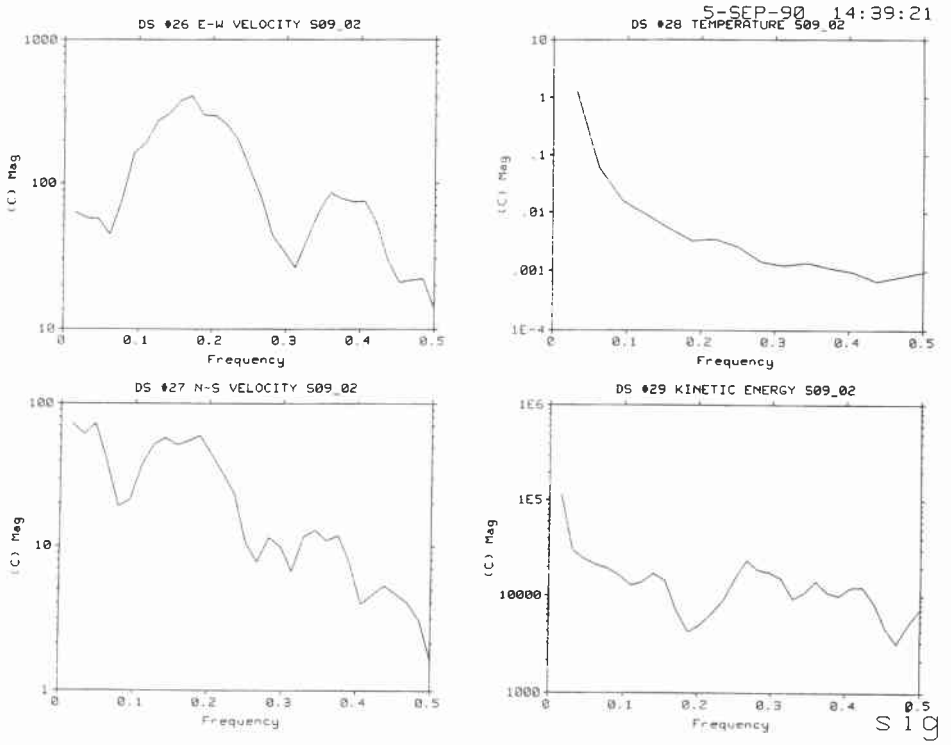

Figure A19d

Security Classification		Project No.
NATO UNCLASSIFIED		04
Document Serial No.	**Date of Issue**	**Total Pages**
SM-269	July 1993	76 pp.

Author(s)

G. Peggion

Title

Interpretation and representation of the synoptic features in the Iceland–Faeroe–Shetland region

Abstract

The kinematic structure of the sub-inertial fluctuations of measured current and temperature fields from 6 moorings deployed during the June 1989 Icelandic Current Experiment (ICE) cruise is analyzed and interpreted. The field of operations encompassed the Iceland–Faeroe Front (IFF) where high temperature and salinity gradients exist together with mesoscale activity. The currentmeter records were found to be highly contaminated by tidal signals and contain evidence of 2–5 day oscillations (the mesoscale events) embedded in a long period signal of about 10–15 days (synoptic events). The currentmeter data is analyzed for vertical and horizontal coherence. The variability of the IFF is highly energetic and mainly due to baroclinic instability of the frontal flow. Satellite images of the region show that in the vicinity of the front mesoscale features are present with horizontal scales of 15 to 50 km. Ocean currents were calculated from hydrography data with a diagnostic model. The model assumes geostrophic and hydrostatic balances and uses CTD measurements taken in the region during the interval of currentmeter measurements. It is found that the model reproduces the large scale current structures of the region but underestimates the velocity magnitude of the upper ocean. This is attributed to the simplified physics that is incorporated into the formalism.

Keywords

Bryan–Cox model, currents, salinity, sound velocity, temperature

Issuing Organization

North Atlantic Treaty Organization
SACLANT Undersea Research Centre
Viale San Bartolomeo 400, 19138 La Spezia, Italy

tel: 0187 540 111
fax: 0187 524 600
telex: 271148 SACENT I

[From N. America: SACLANTCEN CMR-426 (New York) APO AE 09613]

Initial Distribution for SM-269

SCNR for SACLANTCEN	
SCNR Belgium	1
SCNR Canada	1
SCNR Denmark	1
SCNR Germany	1
SCNR Greece	1
SCNR Italy	1
SCNR Netherlands	1
SCNR Norway	1
SCNR Portugal	1
SCNR Spain	1
SCNR Turkey	1
SCNR UK	1
SCNR US	2
French Delegate	1
SECGEN Rep. SCNR	1
NAMILCOM Rep. SCNR	1

National Liaison Officers	
NLO Belgium	1
NLO Canada	1
NLO Denmark	1
NLO Germany	1
NLO Italy	1
NLO Netherlands	1
NLO UK	3
NLO US	4

Total external distribution	30
SACLANTCEN Library	10
Stock	20
Total number of copies	60